# Atoms in Rotating Lattices and Cavity QED Measurements of Atomic Dynamics

by

**Brandon March Peden**

M.S., Mathematics, Western Washington University, 2004

B.S., Physics, Western Washington University, 2002

A thesis submitted to the

Faculty of the Graduate School of the

University of Colorado in partial fulfillment

of the requirements for the degree of

Doctor of Philosophy in Physics

Department of Physics

2010

This thesis entitled:
Atoms in Rotating Lattices and Cavity QED Measurements of Atomic Dynamics
written by Brandon March Peden
has been approved for the Department of Physics

Murray Holland

Ana Maria Rey

Date

The final copy of this thesis has been examined by the signatories, and we find that both the content and the form meet acceptable presentation standards of scholarly work in the above mentioned discipline.

Peden, Brandon March (Ph.D., Physics)

Atoms in Rotating Lattices and Cavity QED Measurements of Atomic Dynamics

Thesis directed by Prof. Murray Holland

The first part of this thesis describes the behavior of ultracold atoms confined in a rotating optical lattice. We consider gases of strongly-interacting bosons and non-interacting fermions in ring and square lattice geometries. We derive modified Hubbard models to describe the gas and use the quasi-angular momentum (QAM) representation to label the eigenstates. Exact level crossings between states of different QAM are predicted. We identify signatures of these transitions in the momentum distribution, indicating that these states should be distinguishable in time-of-flight experiments.

The second part of this thesis describes a scheme for nondestructively probing the dynamics of atoms in optical lattices by coupling to the modes of an optical resonator. The cavity fields set up both the optical lattice and the probe field so that no external interrogation fields are necessary. The probe is weak so that the atoms can be continuously monitored without affecting the atomic motion. This scheme is applied to a measurement of Bloch oscillations; SNR's as high as $10^4$ are predicted.

In the third part of this thesis, we study the dynamics of atoms in a tilted lattice near the Mott-insulator regime. The dynamics involve the creation and annihilation of dipoles, states generated from the unit-filled states by introducing defects where an atom has hopped exactly one site to the left. We describe how these states can be experimentally distinguished by coupling the atoms to the modes of an optical cavity.

Finally, we describe a quantum non-demolition measurement of the cavity photon number using Raman interferometry of atoms coupled to the cavity modes. Using Bayesian inference, we show that there is a measurement protocol for which the cavity photon number can be determined with just a few measurements.

## Dedication

To Amanda, Ashley, Dylan, and Sean.

To Chuck, Marilyn, and Marty.

## Acknowledgements

Special thanks go to Brad Johnson, Murray Holland, and Dominic Meiser as advisors/mentors: they meant well. Special thanks go to Boris Nowak and David Tieri: without them putting up with me telling them wrong things all the time about master equations and quantum Monte Carlo simulations, I might never have learned how to use those methods. Special thanks go to Ron Pepino, Rajiv Bhat, and Brian Seaman: the office was a spectacularly fun place to work (I mean do crosswords, watch online videos, and play flash games). And special thanks go to Seth Rittenhouse and Rob Wild for the excellent variety of random discussions about physics, baseball, probability, magnetic healing, egg-nog recipes, puzzles and riddles, natural selection, books—most had over a glass of beer.

Here are even more people who helped me understand physics: Alan Bristow, Marilu Chiofalo, Jinx Cooper, Jami Kinnunen, Meret Krämer, Ed Meyer, Ana Maria Rey, Chester Rubbo, Evan Salim, and Jochen Wachter.

These are the people—besides those already mentioned—who are responsible (to blame?) for who I am: the Clans Anderson, Bostwick, and Peden; Mike Burghart, Ariel Coleman, Katy Davis, Matt Fuller, William Funk, Jason Ho, Josh Kaffer, Kevin Langstaff, Patrick Leonard, Brian Long, Alex Mazurkewycz, Molly Painter, Tanya Rivers, Zev Rivers, Lizzie Rothwell, Tim Salazar, Ben Schielke, Jesse Sherman, Ali Smith, Rick Wallace, James Wells, Jason Whittington, Glenn Willis; the cat, Stewart; the Clan Holland; the CU hiking club VIPs; the WWU math and physics departments.

Special acknowledgements go out to Cheez-its, cheese, Charles Darwin, India pale ales, the Southern Sun, community-supported agriculture, Salman Rushdie, scotch, the Lucksmiths, InfiniteRegress Collective Mix Tapes, GarageBand, the Mariners (especially, Ichiro!, Felix, and Jack Z), FactCheck.org, Alton Brown, Google reader, Bon Iver, Radiohead, Built to Spill, Braid, Xtc, Death Cab For Cutie, The Daily Show, USS Mariner, FanGraphs, J. R. R. Tolkien, Lookout Landing, babies, xkcd, Dinosaur Comics, Ernest Hemingway, Dresden Codak, Indexed, MLB.tv, PhD Comics, Pitchfork Music, Daytrotter, La Blogotheque Take-Away Shows, Wins Above Replacement, Michael Pollan, the Beaver Inn, Richard Dawkins, National Public Radio, Wait Wait Don't Tell Me, New York Times crosswords, Craig Calcaterra of Shysterball, Dave Cameron of USSM, Joe Posnanski of SI, television, Bellingham, Budapest, Boulder, beer-brewing and cheese-making, jam-canning and bread-baking, Accustomed to Failure, and My Little Brother.

Plus everyone else.

## Contents

**Chapter**

# Figures

**Figure**

# Chapter 1

# Introduction

## 1.1 Background

Experimental and theoretical studies of quantum gases of ultracold atoms have been successful in replicating the behavior of a wide class of condensed matter systems. In particular, Bose-Einstein condensation (BEC) [4, 16, 32] and the degenerate Fermi gas [33] have both been realized, and there have been extensive studies of superfluidity, vortex formation [135], and the BCS-BEC crossover [48, 90]. More recently, a gas of ultracold polar K-Rb molecules has been created near quantum degeneracy [92]. There are also proposals for simulating quantum Hall physics in rotating BEC's [5, 38, 100, 130]. However, experimentally reaching the parameter regimes necessary to observe this behavior is difficult [117].

The recognition that systems comprised of ultracold atoms trapped in optical lattices could be used to cleanly realize many-particle systems from condensed matter systems [64] has motivated a concentrated effort to study these systems. These systems are highly tunable: lattice spacing and depth can be varied by tuning the frequency and intensity of the lasers, and interactions between atoms can be tuned via a Feshbach resonance; in addition, these systems are very clean, i.e. they lack defects that typically show up in condensed matter systems [15]. By varying the lattice depth, the existence of the Mott-insulator to superfluid transition in a system of interacting bosons trapped in a lattice has been verified [47]. Fundamental concepts from condensed-matter physics

such as Fermi surfaces and interaction-induced inter-band transitions have been investigated [68]. Experiments observing novel phases of ultracold matter in atomic mixtures of Bose and Fermi gases in optical lattices have also been performed [2, 60, 97, 96].

On the theoretical side, proposals for a range class of condensed matter and high-energy models abound. By imprinting an effective magnetic field on two-dimensional systems by either rotating the lattice [9] or driving atomic transitions with a set of lasers [65], phenomena such as the Hofstadter butterfly and quantum Hall physics can be observed. Other recent studies have made direct connections between fractional quantum Hall effect (FQHE) physics and strongly-interacting bosons in optical lattices [10, 52, 99, 125]. Similarly, there have been proposals for realizing systems exhibiting non-Abelian symmetries [98, 114], Kondo-type physics [41], superradiant exciton states [134], and supersolid states [81].

Concurrently, experimental activity in quantum optics and cavity quantum electrodynamics (QED) has provided access to interesting regimes of the light-matter interaction [89]. The strong-coupling regime—where interaction effects dominate over dissipative effects—has been achieved, and both vacuum-Rabi oscillations and mechanical light forces can be monitored in cavity QED setups where the mean photon-number is at all times less than one [57]. By coupling atoms to a cavity mode, efficient conversion of collective atomic excitations into a single photon points the way towards high-efficiency single-photon sources [123]. Kerr non-linearities and dispersive optical bistability due to the displacements of atoms in the cavity have been observed [51]. Photon blockade, where a single photon within a cavity blocks further photons from entering the cavity, leading to photon anti-bunching, has been observed [13].

All along, there has been a productive marriage of the two fields of ultracold atoms in optical lattices and cavity QED. Using the long-range interactions between atoms induced by the field-atom coupling in an optical cavity, the Dicke quantum phase transition has been demonstrated [6]. In addition, cooling of a single trapped ion in

an optical cavity has been achieved by way of cavity sideband cooling [72]. There are numerous theoretical studies of novel models where the atomic and light-field degrees of freedom both play integral parts, such as self-organization of atomic states due to the back-action of light on atoms in optical resonators [70] and phase transitions to superradiant-like phases driven by competition between atom-atom and atom-field interactions [122].

In the great majority of the atomic experiments listed above, destructive measurement schemes such as time-of-flight absorption imaging and Bragg spectroscopy are employed to probe atomic states and dynamics. This allows for high resolution images and a strong signal using only a single measurement. In addition, be preparing several experimental copies with identical initial conditions and varying the duration of the experiment, these schemes provide access to dynamical information. Thus, these measurements are sensitive to a large number of atomic observables in experimental setups. On the theoretical side, linear response theory has been applied to current flow in the presence of a "potential gradient" in order to observe FQHE physics [10], noise correlation analysis has been applied to bosons in a rotating ring lattice [106], and Bragg spectroscopy has been mentioned as a probe for vortex states [129]. The drawback in these schemes is that the atomic sample is destroyed in the process of making a measurement.

The advantage of cavity QED setups is that they come equipped with a natural measurement device, i.e. the light-field out-coupled through the cavity mirrors. In one proposed detection scheme, a weak probe beam is scattered off of atoms trapped in an optical lattice into a cavity mode, and signatures of many-body states such as Mott insulators and superfluids appear in the out-coupled fields [86]. In another, atoms in a lattice interact with two counter-propagating ring-cavity modes, and atomic number statistics can be inferred from the behavior of the cavity fields [27]. Bloch oscillations of atoms in a lattice can also be monitored via the transmission of light through a

cavity [128].

Related techniques have been applied to nondestructive optical measurements of Rabi oscillations in gases of Cs atoms [131], of the Cs clock transition pseudo-spin [26], and of nonlinear dynamics in cold gases [124]. In addition, state preparation such as atomic spin squeezing via measurements on out-coupled cavity fields has been proposed [85, 87, 93] and measured [73, 115]. It has also been demonstrated that the motion of individual atoms in an optical cavity can be tracked by the transmission of a probe field [58].

Quantum non-demolition measurements of the photon number in microwave cavities by way of Ramsey interferometry of Rydberg atoms sent through the cavity have been performed in Paris. Through these experiments, fundamental concepts such as quantum jumps [46] and non-demolition photon counting have been explored [50]. In addition, this setup was used to perform quantum process tomography to reconstruct the master equation describing dissipative processes for photons trapped in microwave cavities [17].

One final example of an area in which ultracold atomic gases and cavity QED have made great strides is in the area of precision measurement. For instance, the newest generation of optical lattice clocks and ion clocks are becoming competitive with the time and frequency standards of the standard fountain atomic clocks [78, 95, 109]. In addition, there is hope for new technologies that promise to increase the stability of these clocks by two orders of magnitude [84]. Finally, by referencing against a highly stable optical cavity, precision measurements have been performed to test variation of fundamental constants such as the fine structure constant [14, 40].

## 1.2 Overview

Throughout these examples, light-matter interactions have been exploited to explore and measure the quantum behavior of both atomic and electromagnetic systems.

In this thesis, we continue this tradition by investigating the behavior of gases of ultracold atoms in optical lattices and proposing methods for detecting atomic states and dynamics in these systems.

In chapter 2, we review the basic physics of optical lattices and optical resonators. We derive the second-order atomic Stark shift that gives rise to an optical lattice potential. We review the basic physics of band theory and the Bose-Hubbard model. Finally, we discuss the properties of optical cavities and describe the mathematical formalism used to treat cavity-field dynamics.

In chapter 3, motivated by the search for quantum Hall physics in atomic systems, we investigate the ground-state behavior of ultracold Bose and Fermi gases in rotating optical lattices. Using the quasi-angular momentum representation, we use exact diagonalization and imaginary-time propagation techniques to explore the atomic behavior. Exact energy-level crossings in the spectrum indicate the possible existence of quantum phase transitions between states of different quasi-angular momentum. The momentum distributions differ significantly for states of different symmetry, indicating that there may be signatures of these transitions in time-of-flight experiments.

In chapter 4, we demonstrate the utility of the many-body formalism developed in chapter 3 by computing approximations to the Bose-Hubbard phase diagram for superlattices.

In chapter 5, we propose a scheme for nondestructively probing the dynamics of a gas of ultracold atoms confined in an optical lattice and subjected to an external potential by coupling the atoms to the counter-propagating modes of an optical ring-cavity. The light field out-coupled through the mirrors is used as the measurement device. This scheme accomplishes three main goals. The cavity field is used to simultaneously set up both the lattice field and the probe field, so that no extra interrogation fields are necessary. The probe is weak so that the atoms can be continuously monitored without affecting their motion. The signal-to-noise (SNR) ratio is large enough to be readily

experimentally detected. Integration of the signal in time and across the atomic cloud yields measurements of dynamical atomic observables such as the center-of-mass oscillation frequency with a large SNR in a single experimental run. This comes at the price of losing information about single atoms and real-time dynamics, but the atomic sample is not destroyed during the measurement. We apply this scheme to a measurement of the Bloch oscillation frequency of atoms trapped in an optical lattice and subjected to a constant, external force such as gravity. We simulate the atomic dynamics and compute the SNR of a heterodyne signal at the cavity output. The maximum predicted SNR is $10^4$.

In chapter 6, we investigate the dynamics of atoms in tilted optical lattices near the Mott-insulator regime. When the Bose-Hubbard interaction strength $U$ is equal to the energy difference between adjacent lattice wells, the atoms can hop in a restricted way about the lattice. The system can be described by way of a "dipole" Hamiltonian, where the allowed atomic states consist of adjacent two-particle/zero-particle sites. In order to detect the dynamics in this system, we employ the scheme from chapter 5, relaxing the condition that the cavity field acts as the lattice potential. This detection scheme is insensitive to dipole states near the unit-filled (i.e. Mott-insulator) state, but there is a large signal for the state with the maximum possible number of dipoles.

In chapter 7, we propose a quantum non-demolition measurement of the cavity photon number via Ramsey interferometry of atoms allowed to interact with the cavity field in the Bragg regime. We employ quantum Bayesian inference to project the cavity field onto a number state after a certain number of repeated measurements. This method can be used for both quantum state preparation and quantum state tomography of the cavity field.

Finally, we conclude with a summary and outlook for future work in chapter 8.

# Chapter 2

## Optical Lattices and Optical Resonators

Much of the work in this thesis relies on two related light-matter systems. First and foremost, we consider optical lattices, which are external, sinusoidal lattice potentials for atoms made up of one or more laser beams. This system is paradigmatic of systems with a discrete translational symmetry, and it gives rise to physical phenomena from condensed matter physics such as band theory, many-body models such as the Bose-Hubbard Hamiltonian, and quantum phase transitions such as the superfluid/insulator transition. The other system is that of atoms interacting with the quantized, resonant modes of an optical cavity. This system is highly flexible: it can be used to generate external optical lattices for the atoms, to measure the dynamics of atoms trapped in cavities, and it can be used to enter the strongly-interacting regime where single photons can affect the behavior of atoms.

In this chapter, we explain the basic physics of optical lattices and resonators including the general mathematical framework by which we describe these systems and their interactions with ultracold atoms. The discussion of optical lattices relies on the material in references [12, 67, 80, 107]. The discussion of optical resonators, including general characteristics and the Gaussian resonator modes, relies on the material in references [121, 133]. The mathematical description of cavity field dynamics relies on material contained in references [77, 88].

## 2.1 Optical Lattices

Two-level atoms experience a position-dependent Stark shift when subjected to an off-resonant laser field. This shift gives rise to an external potential. In appendix B, we perform a rigorous calculation where high-lying excited states are adiabatically slaved to two low-lying states. Here, we make a plausibility argument through the use of second-order perturbation theory.

Given two internal states $|e\rangle$ and $|g\rangle$ of an atom, the interaction Hamiltonian between the atom and a single quantized mode of the electromagnetic field is given by

$$\hat{H}_{\mathrm{I}} = \frac{\hbar\Omega}{2}\hat{\sigma}^{+}\hat{a}u(\hat{\mathbf{x}}) + \frac{\hbar\Omega}{2}\hat{\sigma}^{-}\hat{a}^{\dagger}u^{*}(\hat{\mathbf{x}}), \tag{2.1}$$

where

$$\hat{\sigma}^{+} = |e\rangle\langle g| = (\hat{\sigma}^{-})^{\dagger}, \tag{2.2}$$

and $\hat{a}$ is the annihilation operator for the field mode with mode function $u(\mathbf{x})$. We have made both the dipole and rotating wave approximations in writing this Hamiltonian. In the optical domain, these are very good approximations. Typical wavelengths for optical fields are in the hundreds of nanometers, two orders of magnitude larger than the size the atoms. In addition, the rotating-wave approximation requires that

$$|\Omega| \ll |\omega + \omega_{eg}|, \tag{2.3}$$

where $\omega$ is the frequency of the field mode, and $\omega_{eg}$ is the atomic transition frequency. This is easily satisfied in the optical domain where $\omega/2\pi \approx 10^{15}$Hz.

When the detuning $\delta = \omega - \omega_{eg}$ between the atomic transition frequency and field frequency satisfies

$$|\delta| \gg |\Omega|\,, \tag{2.4}$$

we can compute the second-order correction to the ground state energy as

$$E_{g}^{(2)} = \frac{|\langle e|\hat{H}_{\mathrm{I}}|g\rangle|^{2}}{\hbar\delta} = \frac{\hbar|\Omega|^{2}}{4\delta}\hat{a}^{\dagger}\hat{a}|u(\hat{\mathbf{x}})|^{2}. \tag{2.5}$$

This expression takes the form of an external potential, the strength of which depends on the field intensity.

If the electromagnetic field is in a coherent state with a large average value, $\alpha$, then the intensity fluctuations $\Delta\hat{a}^\dagger\hat{a}/\hat{a}^\dagger\hat{a}$ are on the order of $1/|\alpha|$, which can be made extremely small. In this case, we can neglect the effects that field fluctuations and atom-field correlations have on the atoms. We absorb the field intensity into an effective coupling constant, and the atoms see a potential,

$$V(\hat{\mathbf{x}}) = \hbar g_0 |u(\hat{\mathbf{x}})|^2. \tag{2.6}$$

If the field mode is a standing-wave, then

$$|u(\hat{\mathbf{x}})|^2 \propto \cos^2(\mathbf{k}\cdot\hat{\mathbf{x}}), \tag{2.7}$$

and we can see that the atoms experience a sinusoidal lattice potential of lattice constant, $2\pi/|\mathbf{k}|$.

This simple model leads to a wealth of physical phenomena. At the single-particle level, the discrete translational symmetry of the system gives rise to band theory and Bloch functions. When the lattice depth is large enough, the system enters the tight-binding regime which is characterized completely by an atomic tunneling rate between adjacent lattice wells. At the many-body level, a gas of ultracold atoms trapped in an optical lattice gives rise to clean realizations of models from condensed matter physics such as the Bose-Hubbard model [64].

### 2.1.1 Band theory

The concept of band physics can be approached from two directions. The particle can be treated as nearly free, in which case the introduction of a weak periodic potential breaks the continuous translational symmetry of the free problem. States with the same symmetry properties mix with each other under the perturbation, giving rise to gaps

in the free-particle dispersion relation. That is, the perturbation gives rise to bands of allowed energies separated by gaps on the order of the perturbing potential. On the other hand, the particle can be treated as being tightly bound to the sites on a periodic lattice, where the energy associated with the particle being localized to specific sites is identical across the lattice. Allowing the particle to hop between adjacent sites at a rate $J$ adds a width to the originally flat energy spectrum, giving rise to a band of allowed energies of width, $2J$. These two ways of viewing the physics of an atom moving in the presence of an external periodic potential are complementary, as one gives rise to a theory about band-gaps, and the other gives rise to a theory about bandwidths.

Here, we introduce band physics using the concept of nearly-free particles. Later, when discussing the Bose-Hubbard model, we use the language of the tight-binding model. Moving between these languages requires the concepts of Bloch and Wannier functions, which we move on to now. In most of what follows, we consider one-dimensional systems. The generalization to two and three dimensional systems is relatively straightforward.

A small periodic potential $V(x)$ of period $d$ couples two free-particle wave functions $\psi_1(x) = e^{ik_1x}/\sqrt{V}$ and $\psi_2(x) = e^{ik_2x}/\sqrt{V}$ only if $k_1$ and $k_2$ differ by $2\pi/d$, as shown by the calculation,

$$\begin{aligned}\int_{-\infty}^{\infty} dx \frac{e^{-ik_2x}}{\sqrt{V}} V(x) \frac{e^{ik_1x}}{\sqrt{V}} &= \int_{-\infty}^{\infty} dx \frac{e^{-ik_2(x-d)}}{\sqrt{V}} V(x-d) \frac{e^{ik_1(x-d)}}{\sqrt{V}} \\ &= e^{-i(k_1-k_2)d} \int_{-\infty}^{\infty} dx \frac{e^{-ik_2x}}{\sqrt{V}} V(x) \frac{e^{ik_1x}}{\sqrt{V}}. \end{aligned} \tag{2.8}$$

Due to the phase multiplying the integral, this matrix element must be zero unless $k_1$ and $k_2$ differ by a multiple of $2\pi/d$. In particular, the two wave functions $\psi_1(x) = e^{i\pi x/d}/\sqrt{V}$ and $\psi_2(x) = e^{-i\pi x/d}/\sqrt{V}$ at the Brillouin zone boundaries ($q = \pm\pi/d$) are coupled to each other. The potential acts as a perturbation that breaks the degeneracy between

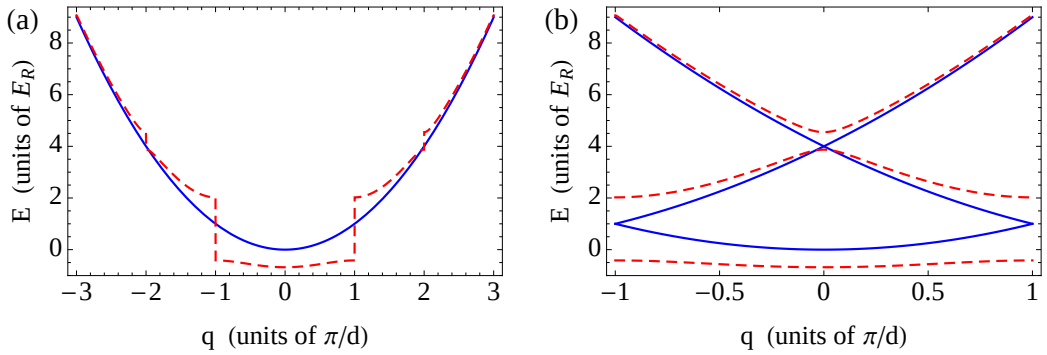


Figure 2.1: Dispersion relation for free particles (blue, solid) and particles moving in a one-dimensional sinusoidal lattice (red, dashed) plotted in (a) extended zone scheme and (b) reduced zone scheme. Free space dispersion relations are plotted versus momentum, and lattice dispersion relations are plotted versus quasi-momentum. Energy is in units of the recoil energy, $E_R = \hbar^2\pi^2/2md^2$, where $d$ is the lattice spacing. The lattice depth is $V_0 = 5E_R$.

these two states, creating new eigenfunctions,

$$\psi_\pm(x) = \frac{1}{\sqrt{2V}}\left(e^{i\pi x/d} \pm e^{-i\pi x/d}\right), \tag{2.9}$$

with corresponding energies,

$$E_\pm = \frac{\hbar^2}{2m}\frac{\pi^2}{d^2} + \langle\psi_\pm|\hat{V}|\psi_\pm\rangle. \tag{2.10}$$

This process opens up a gap,

$$\Delta = |\langle\psi_-|\hat{V}|\psi_-\rangle - \langle\psi_+|\hat{V}|\psi_+\rangle|, \tag{2.11}$$

at the Brillouin zone boundaries. In a reduced zone scheme, this energy spectrum becomes the familiar one-dimensional Bloch band diagram (see figure 2.1).

The introduction of a periodic potential breaks the continuous translational symmetry of the system, and therefore the wave functions are no longer momentum eigenstates. Instead, the eigenfunctions of the Hamiltonian are eigenfunctions of a discrete translation operator, $T_d$, that translates the entire system by one lattice spacing,

$$\psi(x-d) = T_d\psi(x) = e^{-iqd}\psi(x), \tag{2.12}$$

and can be labeled by $q$, the quasi-momentum. A quasi-momentum eigenstate of a periodic Hamiltonian can be written as the product of a plane wave and a function periodic in the lattice:

$$\psi_q^{(n)}(x) = e^{iqx} u_q^{(n)}(x), \tag{2.13}$$

$$u_q^{(n)}(x-d) = u_q^{(n)}(x), \tag{2.14}$$

where $n$ is the band index, and $q$ takes on the values,

$$-\frac{\pi}{d} \leq q \leq \frac{\pi}{d}. \tag{2.15}$$

This is the essence of Bloch's theorem, and these eigenfunctions are called Bloch functions.

When these functions are expanded in the atomic momentum basis, the only momenta contributing to the sum are those that differ from $k$ by a reciprocal lattice vector, $G_j = 2\pi j/d$. The expansion is then given by

$$\psi_q^{(n)}(x) = \int_{-\infty}^{\infty} \frac{dk}{\sqrt{2\pi}} e^{ikx} \psi_q^{(n)}(k) = \sum_{j=-\infty}^{\infty} c_j^{(n)} \frac{e^{i(q+2\pi j/d)x}}{\sqrt{2\pi}}, \tag{2.16}$$

where the expansion coefficients $c_j^{(n)}$ are given by

$$c_j^{(n)} = \int_{-\infty}^{\infty} dx \frac{e^{-i(q+2\pi j/d)x}}{\sqrt{2\pi}} \psi_q^{(n)}(x). \tag{2.17}$$

Figure 2.2(a) is an example of a Bloch function in a sinusoidal lattice, and figure 2.2(b) is its Fourier transform.

#### 2.1.1.1 Lowering the symmetry

Since this will be an important concept in the chapter describing gases of ultracold atoms trapped in rotating optical lattices, we note that the arguments made above can be used again when an extra periodic potential is added to a system already having a discrete translational symmetry. If we introduce an extra potential $U(x)$ satisfying

$$U(x - nd) = U(x), \tag{2.18}$$

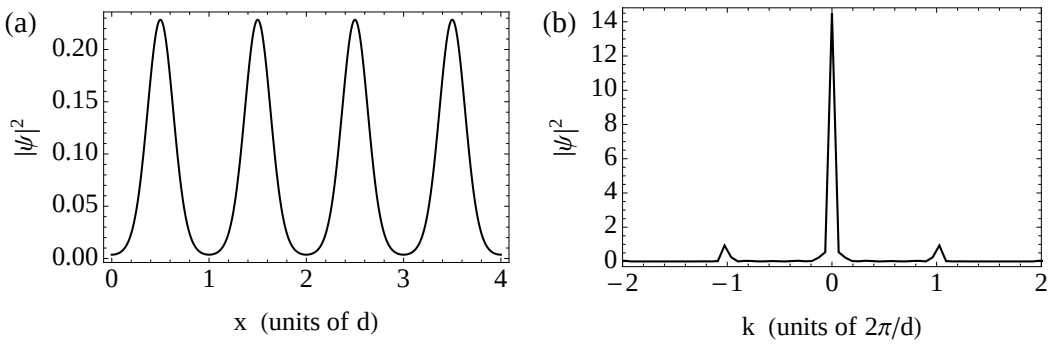


Figure 2.2: The Bloch function for quasi-momentum equal to zero in the first band for an infinite sinusoidal lattice of lattice depth $V_0 = -10E_R$. (a) The real space wave function is concentrated in the lattice sites. (b) The wave function in momentum space exhibits peaks at reciprocal lattice vectors. The envelope of these peaks is given by a Gaussian for large lattice depths, consistent with a lattice of simple harmonic oscillator wells.

where $n \geq 2$ is an integer, and $d$ is the lattice spacing, then Bloch states $\langle x|q\rangle = \psi_q(x)$ and $\langle x|q'\rangle = \psi_{q'}(x)$ will mix with each other if $q$ and $q'$ differ by $2\pi m/nd$. We can show this using a calculation entirely analogous to equation 2.8. Eigenstates of the new Hamiltonian will therefore be linear combinations of these Bloch states. The potential increases the lattice periodicity and, accordingly, decreases the size of the first Brillouin zone to $2\pi/nd$.

In figure 2.3, the lowest band (red, dashed) of a one-dimensional lattice with an arbitrary periodic potential is plotted in a reduced zone scheme. Introducing an infinitesimal potential whose periodicity is three times the lattice spacing $d$, the first Brillouin zone is reduced to the region $-\pi/3d \leq q \leq \pi/3d$. Equation (2.8) shows that the states lying on a vertical line in figure 2.3 mix with each other under the addition of the new potential—i.e., $\langle q'|\hat{U}|q\rangle$ is non-zero for these states. In particular, the degenerate states at $q = 0$ mix, breaking the degeneracy and opening up a gap at $q = 0$ (blue, solid). The single band splits into three bands due to the reduction of the symmetry by $U(x)$.

When the addition of a potential reduces the symmetry of a system as just described, the original eigenstates of the system mix according to their symmetry. As a consequence, gaps open up where there are degeneracies between states of the same symmetry, creating a band structure.

#### 2.1.1.2 Wannier states

Bloch functions can be thought of as the replacements for momentum eigenfunctions when there is no continuous translational symmetry. Indeed, in the infinite lattice case, the Bloch function representation diagonalizes the atomic momentum operator restricted to a single band. It is a natural question to ask whether there is an alternative representation where the functions instead diagonalize the position operator restricted to a single band. This type of representation is a natural one when we are investigating

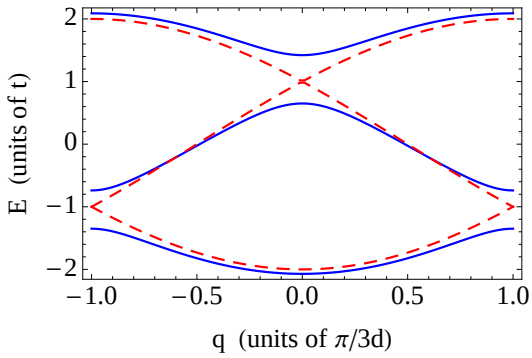


Figure 2.3: Lowest band dispersion relation (red, dashed) for a one-dimensional tight-binding model plotted in a reduced zone scheme that anticipates the lowering of the symmetry via an additional potential with periodicity $3d$. After the introduction of this potential, states with the same quasi-momentum $q$ in the reduced zone mix with each other, opening up gaps anywhere that there is a degeneracy. This results in a modified dispersion relation (blue, solid).

the physics of atoms hopping between sites of a lattice. The Bloch representation can obscure this physics since the Bloch functions are delocalized across the entire lattice.

Such a representation exists, and the resulting functions are called Wannier functions. They take the form,

$$w_j^{(n)}(x) = \frac{1}{\sqrt{N}} \sum_q e^{iqx_j} \psi_q^{(n)}(x), \tag{2.19}$$

where $x_j$ is the position of the center of lattice well $j$. It is easy to show that these Wannier functions are just translations of each other, that is,

$$w_j^{(n)}(x) = w^{(n)}(x - x_j), \tag{2.20}$$

and that they are orthogonal. In addition, $w_j^{(n)}(x)$ is localized to the lattice site $j$. It should be noted here that this localization condition depends on a choice of relative phases between the different Bloch states. For the most part, this is an issue when performing numerical calculations, and we discuss this problem more carefully in appendix A.

In figures 2.4(a) and 2.4(b), we have plotted Wannier functions localized at $x_j = 3d$ for lattices with depth $-E_R$ and $-15E_R$, respectively; $E_R$ is the recoil energy $E_R = \hbar^2 k^2/2m$. As the lattice depth is increased, the Wannier functions get more localized to the lattice sites. The Wannier functions approach Gaussians as the lattice depth goes to infinity.

### 2.1.2 Hubbard models

The Wannier function representation is the natural one in systems where the lattice depth is relatively large. In this case, the atoms are well-described as being localized to individual lattice sites with tunneling allowed only between adjacent sites. This is known as tight-binding, and is it in this regime that models such as the Bose-Hubbard model can be derived. In order to investigate this, we consider the single-

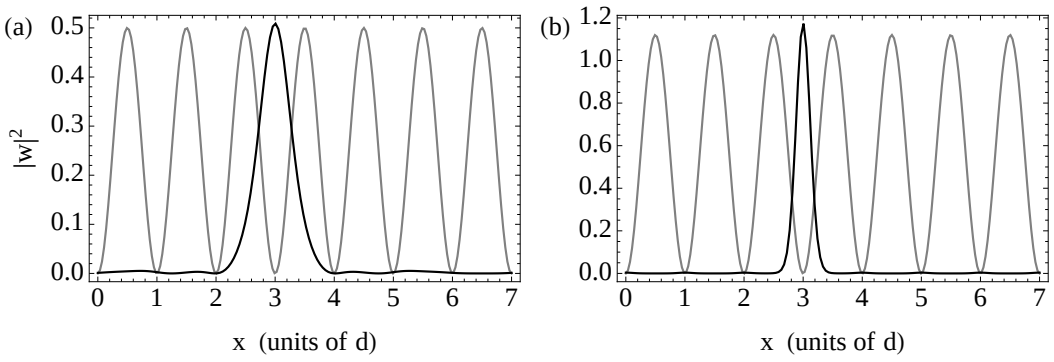


Figure 2.4: Examples of Wannier functions for sinusoidal lattices. Superimposed on these plots is the lattice potential in arbitrary units. (a) Wannier function for a lattice of depth $V_0 = -E_R$, localized to $x = x_j = 3d$. (b) Wannier function for a lattice of depth $V_0 = -15E_R$, localized to $x = 3d$.

particle Hamiltonian,

$$H(x) = -\frac{\hbar^2}{2M}\frac{d^2}{dx^2} + V_0 \cos^2\left(k_{\mathrm{L}} x\right), \tag{2.21}$$

which corresponds to the second-quantized, bosonic Hamiltonian,

$$\hat{H}_0 = \int dx\ \hat{\Psi}^\dagger(x) \left(-\frac{\hbar^2}{2M}\frac{d^2}{dx^2} + V_0 \cos^2\left(k_{\mathrm{L}} x\right)\right) \hat{\Psi}(x). \tag{2.22}$$

If the atoms interact via a short-range, s-wave interaction, we include a term

$$\hat{U} = \frac{\hbar g}{2} \int dx\ \hat{\Psi}^\dagger(x)\hat{\Psi}^\dagger(x)\hat{\Psi}(x)\hat{\Psi}(x), \tag{2.23}$$

where

$$g = \frac{4\pi\hbar a_s}{M} \tag{2.24}$$

with $a_s$ the s-wave scattering length.

We expand the field operators in the Wannier states as

$$\hat{\Psi}(x) = \sum_{n,j} w^{(n)}\left(x - x_j\right) \hat{b}_j^{(n)}, \tag{2.25}$$

in which case the Hamiltonian can be written as

$$\hat{H} = -\sum_{j,k}\sum_{n',n} J_{jk}^{(n)} \hat{b}_j^{(n)\dagger} \hat{b}_k^{(n)} + \frac{1}{2}\sum_{i,j,k,l}\sum_{l,m,n,p} U_{ijkl}^{(mnpr)} \hat{b}_i^{(m)\dagger} \hat{b}_j^{(n)\dagger} \hat{b}_k^{(p)} \hat{b}_l^{(r)}, \tag{2.26}$$

where

$$J_{jk}^{(n)} = -\int dx\ w^{(n)*}(x - x_j) H(x) w^{(n)}(x - x_k), \tag{2.27}$$

$$U_{ijkl}^{(mnpr)} = \hbar g \int dx\ w^{(m)*}(x - x_i) w^{(n)*}(x - x_j) w^{(p)}(x - x_k) w^{(r)}(x - x_l). \tag{2.28}$$

Clearly, $J_{jk}^{(n)} = J_{j-k+1,1}^{(n)}$.

In figure 2.5, we have plotted $J = J_{2,1}^{(1)}$ and $J_{3,1}^{(1)}/J_{2,1}^{(1)} = J_2/J$ as a function of lattice depth. At about $V_0 = 5E_R$, $J_{1,1}^{(1)}/J_{2,1}^{(1)} = 0.05$, and we can neglect all but nearest-neighbor hopping. This defines the tight-binding regime. Without numerical justification, we also assume that the dominant interaction term comes only from the on-site, single-band interaction $U = U_{1111}^{(1111)}$. This approximation come about because

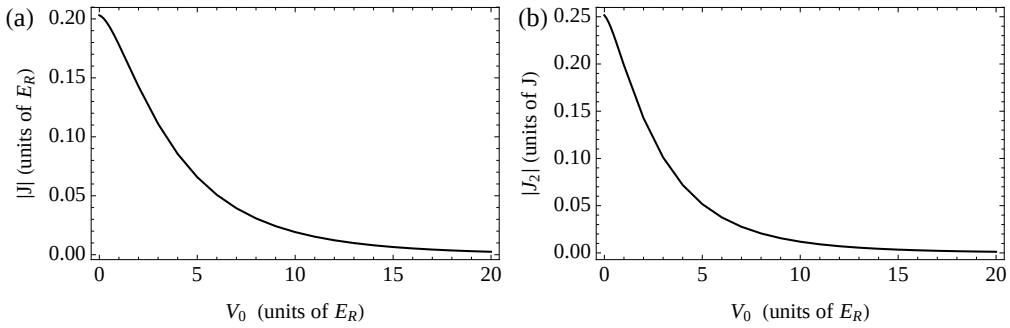


Figure 2.5: Tight-binding tunneling energies for nearest neighbor and next-to-nearest neighbor hopping, plotted as a function of lattice depth. (a) Nearest-neighbor hopping parameter $J$ has a maximum of about $0.2E_R$. This quickly decays as a function of lattice depth. (b) Next-to-nearest neighbor hopping rate as a function of $V_0$. At $V_0 = 5E_R$, the ratio $|J_2/J|$ is about 0.05. This is the cut-off for neglecting all but nearest neighbor hopping, which defines the tight-binding regime.

the Wannier functions are highly peaked about the centers of the lattice wells for large lattice depths. In this case, the Wannier functions between different sites do not overlap to a great extent, indicating that the other interaction parameters are small.

We have therefore arrived at the single-band Bose-Hubbard model,

$$\hat{H} = \sum_j \epsilon \hat{b}_j^\dagger \hat{b}_j - \sum_{\langle j,k \rangle} J \hat{b}_j^\dagger \hat{b}_k + \frac{U}{2} \sum_j \hat{b}_j^\dagger \hat{b}_j^\dagger \hat{b}_j \hat{b}_j, \tag{2.29}$$

where

$$\epsilon = \int dx \; w^{(n)*}(x - x_j) H(x) w^{(n)}(x - x_j). \tag{2.30}$$

This model has been very well-studied in both the condensed-matter and atomic physics communities. There is a quantum phase transition that occurs in the $(\mu/U, J/U)$-plane—where $\mu$ is the chemical potential—between superfluid and insulator phases, known as the Mott-insulator to superfluid transition [39]. We briefly outline the derivation of this transition in a mean-field approximation.

As described in references [111, 127], we introduce an order parameter $\psi = \langle \hat{b}_i \rangle$ which characterizes the superfluid phase of the system. Interpreting this quantity as an

order parameter is *a posteriori* justified by the calculations performed below and *a priori* justified by the expectation of an insulator-superfluid transition: in an insulator state $\langle\hat{b}_i\rangle = 0$, and in a superfluid state $\langle\hat{b}_i\rangle \neq 0$. Assuming that the quantum fluctuations

$$\hat{b}_i - \langle\hat{b}_i\rangle = b_i - \psi \tag{2.31}$$

are small, we write the Hamiltonian in terms of the order parameter as

$$\hat{H}_j = -zJ\left((\hat{b}_j^\dagger + \hat{b}_j)\psi - \psi^2\right) + \frac{U}{2}\sum_j \hat{n}_j(\hat{n}_j - 1), \tag{2.32}$$

where $\hat{n}_j = \hat{b}_j^\dagger\hat{b}_j$, $z$ is the number of nearest-neighbor lattice sites for site $j$, and the full Hamiltonian is a sum over the $\hat{H}_j$. We now have a set of non-interacting Hamiltonians that describe each lattice site independently, treating the atoms on all other lattice sites in a mean-field approximation.

Near the superfluid-insulator transition, the order parameter is small, so we treat

$$H^{(1)} = -z\psi J(\hat{b}^\dagger + \hat{b}) + zJ\psi^2 \tag{2.33}$$

as a perturbation of the on-site Hamiltonian

$$H^{(0)} = -\mu\hat{n} + \frac{U}{2}\hat{n}(\hat{n} - 1), \tag{2.34}$$

where $\mu$ is the chemical potential. We work in the grand canonical ensemble.

The first-order and second-order corrections to the unperturbed energies $\epsilon^{(0)} = -\mu n + Un(n-1)/2$ yield an approximate ground-state energy given by

$$\epsilon_g \approx -\mu n + \frac{U}{2}n(n-1) + \left(zJ + z^2J^2\left(\frac{n}{-\mu + U(n-1)} + \frac{n+1}{\mu - Un}\right)\right)\psi^2 \tag{2.35}$$

$$= A_0 + A_2\psi^2. \tag{2.36}$$

In order to determine the true ground state and the phase boundaries, we minimize $\epsilon_g$ with respect to $\psi$. If $A_2 > 0$, then $\psi = 0$ minimizes $\epsilon_g$; if $A_2 < 0$, then some $\psi \neq 0$ minimizes $\epsilon_g$. Thus, setting $A_2$ equal to zero determines the boundary between insulator

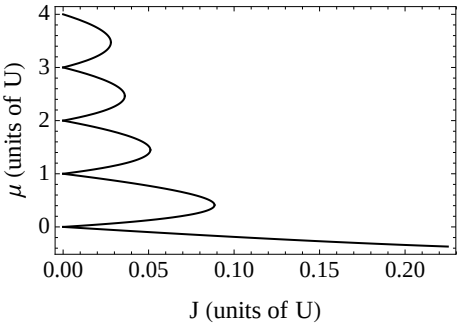


Figure 2.6: The Mott-insulator to superfluid phase diagram as computed in one dimension using mean-field theory. Inside the rounded lobes are insulator ground states of integer-filling. Outside these so-called Mott lobes, the system is a superfluid.

and superfluid phases. Solving for $\mu$, this yields

$$\mu = \frac{1}{2}(U(2n-1) - zJ) \pm \frac{1}{2}\sqrt{(zJ)^2 - 2zJU(1+2n) + U^2}. \tag{2.37}$$

We plot these phase boundaries in figure 2.6 for a one-dimensional lattice, i.e. $z = 2$. The phase diagram consists of a sequence of lobes. The parameter $A_2$ is positive within these lobes, so that $\psi = 0$, and the ground state is an insulator with a fixed number of particles on each site. Outside of these lobes, $A_2 < 0$, so the ground state is a superfluid.

The Bose-Hubbard model is a jumping-off point for the simulation of a variety of condensed-matter systems in gases of ultracold atoms trapped in optical lattices. In this thesis, we investigate two in particular. In chapter 3, atoms trapped in a two-dimensional rotating lattice are investigated with an eye to emulating quantum Hall physics in optical lattices. In chapter 6, a linear shift is added to the lattice, and the dynamics of atoms near the Mott-insulator regime are investigated.

## 2.2 Optical Cavities

Our interest in marrying the fields of atomic gases in optical lattices and cavity quantum electrodynamics (QED) is two-fold. First, the resonant modes in optical cav-

ities are isolated from each other, allowing access to the regime where atoms interact with single electromagnetic field modes. This not only simplifies the mathematical description of the light-matter interaction, but it also allows investigation of fundamental models from quantum optics such as the Jaynes-Cummings model. In addition, there is an enhancement of the atom-field interaction strength due to the presence of the cavity, allowing access to the strong-coupling regime of cavity QED, where single photons have an effect on the atomic dynamics. Second, these systems come equipped with an inherent measurement device via detection of the light-field out-coupled through the cavity mirrors. This can be exploited for schemes for non-destructive measurement of atomic dynamics in optical lattices. This is discussed in detail in chapters 3 and 6. Here, we discuss the basic characteristics of optical cavities, the resonant field modes that they support, and the mathematical treatment of cavity field dynamics in terms of a master equation.

We consider the simple case of a linear resonator geometry consisting of two spherical mirrors with equal radii of curvature (see figure 2.7). A laser pumps a resonant cavity mode through the cavity mirrors. The geometry of the resonant mode is determined by the geometry of the cavity. These mode functions can be made from linear combinations of free-space Hermite-Gaussian or Laguerre-Gaussian functions, which are solutions to the paraxial wave equation. These modes are defined by a beam waist $w_0$, a resonant frequency $\omega$, and the length $L$ of the cavity.

The presence of the mirrors enforce approximately box-like boundary conditions, in which case the spectral response of the cavity consists of a set of discrete peaks separated in frequency by the free spectral range $\omega_{\text{fsr}}$, as illustrated in figure 2.8. Since the mirrors are not perfectly reflecting, the modes couple weakly to electromagnetic field modes outside the cavity. This means that there is a finite decay time $1/\kappa$ for photons in the cavity, and the resonant peaks acquire a linewidth $\kappa$. To the extent that the linewidths of the cavity and of the in-coupled laser are much smaller than the free

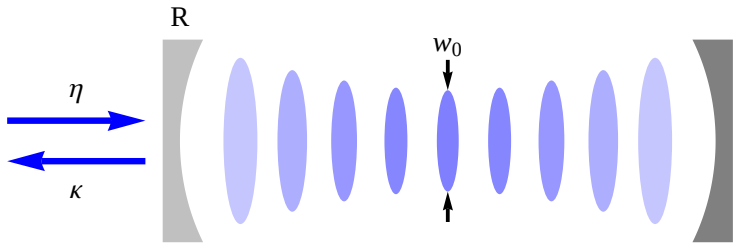


Figure 2.7: Schematic of a linear optical cavity. A laser couples with strength $\eta$ to the cavity modes through a mirror of reflectivity $R$. A standing-wave pattern is set up within the cavity. Photons leak out the cavity through the mirrors at a rate $\kappa$.

spectral range, these modes can be populated independently.

In place of the parameters, $\omega$, $\omega_{\text{fsr}}$, and $\kappa$, cavity properties are often expressed in terms of the quality factor $\mathcal{Q}$ and the finesse $\mathcal{F}$. These are defined as

$$\mathcal{Q} = \frac{\omega}{\kappa}, \tag{2.38}$$

$$\mathcal{F} = \frac{\omega_{\text{fsr}}}{\kappa}. \tag{2.39}$$

In order to get an idea as to what the state-of-the-art is for cavities, we quote the quality factor and finesse for an optical cavity used as the reference to stabilize an optical lattice clock [78] and for a microwave cavity used in quantum-non-demolition measurements [46]. For both cavities, $\mathcal{Q} \approx 10^{10} - 10^{9}$ and $\mathcal{F} \approx 10^{5}$. Of course, these two cavities operate in wildly different regimes: the optical cavity operates at $4.2 \times 10^{14}$Hz, and the microwave cavity operates at $5.1 \times 10^{10}$Hz. The lifetime of a photon in the microwave cavity is about 0.1s, whereas in the optical cavity, the lifetime is about $10^{-4}$s.

We make one final note: if the reflectivity $R$ of the mirror is large enough, then the finesse takes the approximate form,

$$\mathcal{F} \approx \frac{\pi\sqrt{R}}{1-R}. \tag{2.40}$$

This means that the ratio of free spectral range to cavity linewidth is determined solely by the properties of the mirror and not by any other aspects of the cavity design such

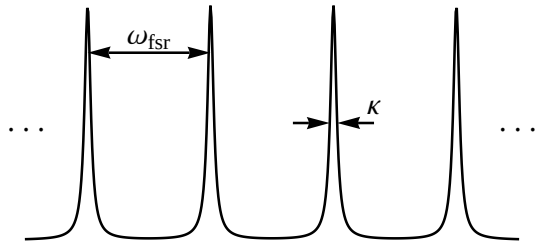


Figure 2.8: Schematic of the spectrum of a linear optical cavity. The discrete spectral peaks are separated by the free spectral range $\omega_{\text{fsr}}$ and acquire a width $\kappa$ due to the finite coupling to modes outside the cavity.

as the length. In other words, the isolation of the resonant modes from each other is determined solely by the reflectivity of the mirror.

In the following, we examine the structure of the resonant modes more carefully.

### 2.2.1 Resonant modes

Electromagnetic fields in free space follow the Helmholtz equation,

$$\left(\nabla^2 + k^2\right) E(\mathbf{r}) = 0, \tag{2.41}$$

where $E(\mathbf{r}, t) = E(\mathbf{r})e^{-i\omega t}$, and $\omega = ck$. Due to the mirror geometry discussed above, we will be concerned with beams that primarily propagate along the axis $\hat{z}$ of the cavity, in which case we define

$$E(x, y, z) = f(x, y, z)e^{-ikz}. \tag{2.42}$$

The Helmholtz equation becomes

$$\frac{\partial^2 f}{\partial x^2} + \frac{\partial^2 f}{\partial y^2} + \frac{\partial^2 f}{\partial z^2} - 2ik\frac{\partial f}{\partial z} = 0. \tag{2.43}$$

Having removed the "fast" spatial dependence along $\hat{z}$, we make the paraxial approximation,

$$\left|\frac{\partial^2 f}{\partial z^2}\right| \ll \left|\frac{\partial^2 f}{\partial x^2}\right|, \left|\frac{\partial^2 f}{\partial y^2}\right|, \left|2k\frac{\partial f}{\partial z}\right|. \tag{2.44}$$

This approximation only holds as long as the plane waves that have appreciable overlap with $f$ have wave vectors that lie within an angle $\theta_0 \approx \pi/6$ of the $z$-axis [121].

To solve the paraxial wave equation, we separate variables as

$$f_{nm}(x, y, z) = f_n(x, z) f_m(y, z), \tag{2.45}$$

where both $f_n(x, z)$ and $f_m(y, z)$ satisfy the equation,

$$\frac{\partial^2 f}{\partial x^2} - 2ik\frac{\partial f}{\partial z} = 0. \tag{2.46}$$

A set of solutions to this equation are given by

$$f_n(x, z) = \left(\frac{2}{\pi}\right)^{1/4} \sqrt{\frac{1}{2^n n!}} \frac{e^{i(n+1/2)\psi(z)}}{w(z)} H_n\left(\frac{\sqrt{2}x}{w(z)}\right) \exp\left(-ik\frac{x^2}{2R(z)} - \frac{x^2}{w^2(z)}\right), \tag{2.47}$$

where

$$w(z) = w_0\left(1 + \left(\frac{z}{z_0}\right)^2\right)^{1/2}, \tag{2.48}$$

$$R(z) = z\left(1 + \left(\frac{z_0}{z}\right)^2\right), \tag{2.49}$$

$$\psi(z) = \arctan\left(\frac{z}{z_0}\right), \tag{2.50}$$

$$z_0 = kw_0^2/2, \tag{2.51}$$

and $H_n$ is a Hermite polynomial. We reconstruct the full solution as

$$\begin{aligned} f_{nm}(x, y, z; k) &= f_n(x, z) f_m(y, z) e^{-ikz} \\ &= \left(\frac{2}{L\pi}\right)^{1/2} \sqrt{\frac{1}{2^{n+m} n! m!}} \frac{e^{i(n+m+1)\psi(z)} e^{-ikz}}{w(z)} \\ &\quad \times H_n\left(\frac{\sqrt{2}x}{w(z)}\right) H_m\left(\frac{\sqrt{2}y}{w(z)}\right) \exp\left(-ik\frac{(x+y)^2}{2R(z)} - \frac{(x+y)^2}{w^2(z)}\right), \end{aligned} \tag{2.52}$$

called Hermite-Gaussian modes. They satisfy the orthogonality relation,

$$\delta_{nn'}\delta_{mm'}\delta_{kk'} = \int_{-\infty}^{\infty} dz \int_{-\infty}^{\infty} dx \int_{-\infty}^{\infty} dy \; f^*_{n'm'}(x, y, z; k') f_{nm}(x, y, z; k). \tag{2.53}$$

From equation 2.52, we can see that the function $w(z)$ determines the width of a Gaussian function that falls off away from the $z$-axis. This is a minimum at $z = 0$

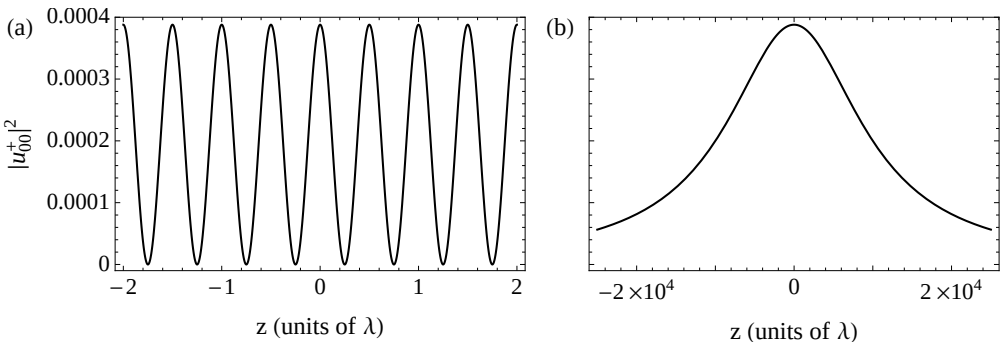


Figure 2.9: Longitudinal cross-section and envelope of a Hermite-Gaussian mode as a function of $z$ with $w_0 = 57\lambda$, $L \approx 5 \times 10^4\lambda$, and $x = y = 0$. (a) The mode is approximately a cosine function near $z = 0$. (b) The envelope of the mode function decreases away from $z = 0$.

and takes on the value $w_0$. For this reason, $w_0$ is called the beam-waist. The width of the Gaussian increases as $|z|$ is increased from zero, indicating that the mode spreads out away from $z = 0$. This is a diffraction effect that arises because the electric field is being confined to some finite region in space.

We construct standing wave modes from equation 2.52 as

$$u^{\pm}_{nm}(x,y,z;k) = u_{nm}(x,y,z)\begin{Bmatrix}\cos\\ \sin\end{Bmatrix}\left(kz + k\frac{(x+y)^2}{2R(z)} - (n+m+1)\psi(z)\right), \tag{2.54}$$

$$u_{nm}(x,y,z) = \sqrt{\frac{1}{L\pi}\frac{1}{2^{n+m-2}n!m!}}\frac{e^{-(x+y)^2/w^2(z)}}{w(z)}H_n\left(\frac{\sqrt{2}x}{w(z)}\right)H_m\left(\frac{\sqrt{2}y}{w(z)}\right), \tag{2.55}$$

where $u_{nm}$ determines the envelope and transverse behavior of the mode function. In figure 2.9, we plot the longitudinal behavior of the standing-wave mode $|u^+_{k00}(x,y,z;k)|^2$ for $x = y = 0$. For this particular choice of parameters, explained below, the envelope $|u_{00}(0,0,z)|^2$ is roughly constant over hundreds of wavelengths, meaning that the mode function is well-described by a cosine function in this region. The envelope eventually appreciably decreases far enough away from $z = 0$. In figure 2.10, we plot the transverse behavior of $|u^+_{k00}(x,y,z;k)|^2$. The width $w(z)$ of the Gaussian decay of the mode function away from the $z$-axis increases as $|z|$ is increased. Finally, in figure 2.11, we plot

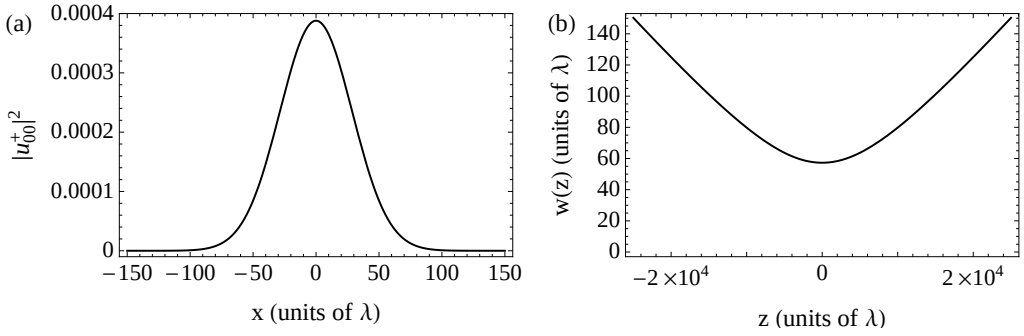


Figure 2.10: Transverse behavior of the (00) Hermite-Gaussian mode with $w_0 = 57\lambda$ and $L \approx 5 \times 10^4 \lambda$. (a) The mode at $z = 0$ falls off as a Gaussian away from the $z$-axis with width given by the beam waist $w_0$. (b) The effective width $w(z)$ of the Gaussian increases from $w_0$ as $|z|$ is increased.

transverse cross-sections of three Hermite-Gaussian modes. These modes have markedly different transverse structures but essentially the same longitudinal behavior. We now turn to the exact formulas for the resonant frequencies.

#### 2.2.1.1 Resonant frequencies and mode parameters

The total phase shift that the Hermite-Guassian modes undergo as they traverse the cavity is given by

$$\begin{aligned}\phi(z_2 - z_1) &= k(z_2 - z_1) - (n + m + 1)(\psi(z_2) - \psi(z_1)) \\ &= kL - (n + m + 1)(\arctan(z_2/z_0) - \arctan(z_1/z_0)).\end{aligned} \tag{2.56}$$

The parameters $z_2$ and $z_1$ are the positions of the right-hand and left-hand mirrors, respectively. We take them to be $z_1 = -L/2$ and $z_2 = L/2$. The resonance condition for a standing-wave cavity mode states that the total round-trip phase shift must be an integral multiple of $2\pi$, leading to

$$\omega_{qnm} = \omega_{\text{fsr}} \left( q + (n + m + 1)\frac{1}{\pi} \left( \arctan\left(\frac{z_2}{z_0}\right) - \arctan\left(\frac{z_1}{z_0}\right) \right) \right) \tag{2.57}$$

where $\omega_{\text{fsr}} = \pi c/L$, and $q$ is an integer. Defining

$$g = 1 - \frac{L}{R}, \tag{2.58}$$

where $R$ is the radius of curvature for the mirrors, we can show that

$$\cos^{-1}(g^2) = \arctan(z_2/z_0) - \arctan(z_1/z_0), \tag{2.59}$$

$$g = \frac{4\pi^2(w_0/\lambda)^4 - (L/\lambda)^2}{4\pi^2(w_0/\lambda)^4 + (L/\lambda)^2}. \tag{2.60}$$

This implies that the resonant frequencies are given by

$$\omega_{qnm} = \omega_{\text{fsr}}(q + (n + m + 1)\pi^{-1}\cos^{-1}(g^2)). \tag{2.61}$$

These are also the resonant frequencies for the Laguerre-Gaussian beams.

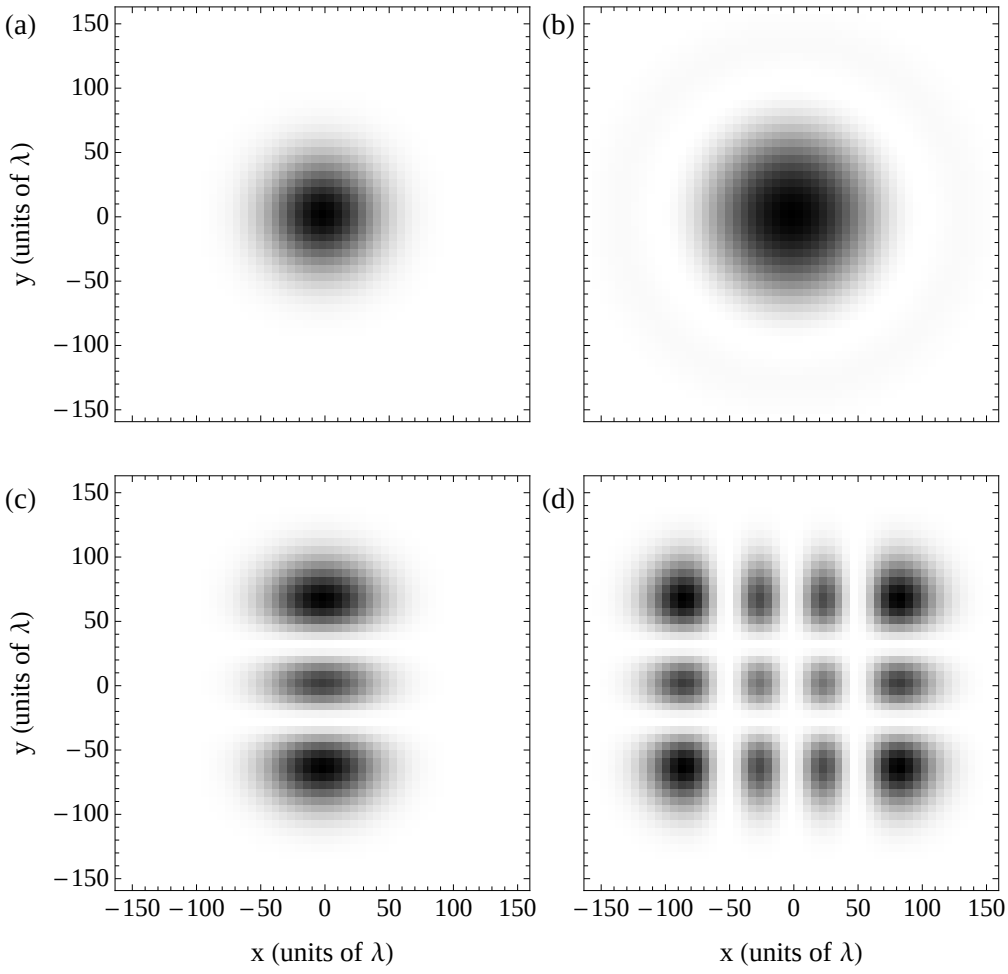


Figure 2.11: Cross-sections of sample Hermite-Gaussian modes with $w_0 = 57\lambda$ and $L \approx 5 \times 10^4\lambda$. (a) The (00)-mode at $z = 0$. (b) The (00)-mode at $z = \sqrt{2}z_0 \approx 10^4\lambda$. (c) The (20)-mode at $z = 0$. (d) The (23)-mode at $z = 0$.

### 2.2.2 Cavity field dynamics and atom-field coupling

We now turn to the quantum description of cavity field dynamics in a cavity. The Hamiltonian for a set of resonant cavity modes being pumped by an in-coupled laser of frequency $\omega_{\mathrm{P}}$ is given by

$$\hat{H} = \sum_{\mathbf{k},\lambda} \hbar \left(\omega_k - \omega_{\mathrm{P}}\right) \hat{a}^{\dagger}_{\mathbf{k},\lambda} \hat{a}_{\mathbf{k},\lambda} + \sum_{\mathbf{k},\lambda} \hbar \left( \eta^{*}_{\mathbf{k},\lambda} \hat{a}_{\mathbf{k},\lambda} + \eta_{\mathbf{k},\lambda} \hat{a}^{\dagger}_{\mathbf{k},\lambda} \right), \tag{2.62}$$

where $\mathbf{k} = \omega/c$ is the wave-number of the resonator mode corresponding to $\hat{a}_{\mathbf{k},\lambda}$, and $\lambda$ indexes its polarization. The parameter $\eta_{\mathbf{k},\lambda}$ measures the coupling strength of the in-coupled laser to the resonant mode $(\mathbf{k}, \lambda)$. It is a function of the mirror reflectivity and the pumping laser intensity. The decay of photons through the mirrors is governed by a Liouvillian,

$$\hat{\mathcal{L}}\hat{\rho} = -\sum_{\mathbf{k},\lambda} \frac{\hbar \kappa_{\mathbf{k},\lambda}}{2} \left( \hat{a}^{\dagger}_{\mathbf{k},\lambda} \hat{a}_{\mathbf{k},\lambda} \hat{\rho} + \hat{\rho} \hat{a}^{\dagger}_{\mathbf{k},\lambda} \hat{a}_{\mathbf{k},\lambda} - 2 \hat{a}_{\mathbf{k},\lambda} \hat{\rho} \hat{a}^{\dagger}_{\mathbf{k},\lambda} \right), \tag{2.63}$$

where $\hat{\rho}$ is the reduced density matrix of the cavity field, and $\kappa_{\mathbf{k},\lambda}$ is the rate at which photons in mode $(\mathbf{k}, \lambda)$ decay. The density matrix follows the equation of motion,

$$i\hbar \frac{d\hat{\rho}}{dt} = [\hat{H}, \hat{\rho}] + i\hat{\mathcal{L}}\hat{\rho}. \tag{2.64}$$

It is apparent from this equation of motion that each mode acts independently. For this reason, we treat only a single mode $\hat{a}$ in what follows. This will not be the case when atoms are allowed to interact with the field.

The field amplitude within the cavity is proportional to $\langle \hat{a} \rangle = \alpha$. This quantity's equation of motion is given by

$$i \frac{d\alpha}{dt} = \left( \omega - \omega_{\mathrm{P}} - i\frac{\kappa}{2} \right) \alpha + \eta. \tag{2.65}$$

This equation is solved by

$$\alpha(t) = \alpha(0) e^{-i(\omega - \omega_{\mathrm{P}})t} e^{-\kappa t/2} + (1 - e^{-i(\omega - \omega_{\mathrm{P}})t} e^{-\kappa t/2}) \frac{-\eta}{\omega - \omega_{\mathrm{P}} - i\kappa/2}, \tag{2.66}$$

which describes some transient phase evolution $e^{-i(\omega-\omega_{\rm P})t}$ of $\alpha$ and a steady state value,

$$\alpha(t\rightarrow\infty)=\frac{-\eta}{\omega-\omega_{\rm P}-i\kappa/2}. \tag{2.67}$$

We turn to the interaction of these modes with a gas of atoms. As we have mentioned, we will consider the special cases of a single-mode linear cavity and a two-mode, degenerate ring cavity. In addition, we will assume that the cavity field is far enough detuned from the atomic transition that high-lying excited states of the atoms can be adiabatically slaved to the lower lying states, as described in appendix B. In this case, we can write the interaction as

$$\hat{H}_{\rm I}=\hbar g\int dz\ \hat{\Psi}^{\dagger}(z)\left(\hat{a}_{k}^{\dagger}\hat{a}_{k}+\hat{a}_{-k}^{\dagger}\hat{a}_{-k}+\hat{a}_{k}^{\dagger}\hat{a}_{-k}e^{-i2kz}+\hat{a}_{-k}^{\dagger}\hat{a}_{k}e^{i2kz}\right)\hat{\Psi}(z) \tag{2.68}$$

for the ring cavity and

$$\hat{H}_{\rm I}=\hbar g\ \hat{a}^{\dagger}\hat{a}\int dz\ \hat{\Psi}^{\dagger}(z)\cos^{2}(kz)\hat{\Psi}(z) \tag{2.69}$$

for the linear cavity.

# Chapter 3

## Bose and Fermi Gases in Rotating Optical Lattices

**The results in this chapter were published in the Physical Review A as Phys. Rev. A 74, 063606 (2006) [11] and in the Journal of Physics B: Atomic, Molecular, and Optical Physics as J. Phys. B: At. Mol. Phys. 40, 3725 (2007) [101].**

One of the current thrusts of research in cold quantum gases trapped in optical lattices is demonstrating and investigating strongly-correlated physics. In particular, there have been a number of theoretical efforts aimed at observing quantum Hall physics in systems comprised of ultracold atomic gases in optical lattices [10, 65]. A promising line of research takes advantage of a mapping between the Hamiltonian of electrons confined in two dimensions in the presence of a constant transverse magnetic field and that of a rotating atomic gas. This has led to various theoretical studies predicting fractional quantum Hall effect (FQHE) behavior in rotating BEC's [5, 38, 100, 130]. However, experimentally reaching the parameter regimes necessary to observe this behavior is difficult [117]. Optical lattices offer a solution to this problem by tightly confining atoms in the lattice wells, thereby enhancing correlations.

Motivated by this, preliminary exact diagonalization studies of bosonic atoms in rotating lattices were carried out using a Bose-Hubbard model modified by a rotation term [9]. This work identified quantum phase transitions between states of different vorticity as the rotation rate was increased. It was then extended to explicit studies of quantum Hall physics in rotating lattices [10].

Further work is required for a physical understanding of the transitions. In this chapter, we present analytical and numerical results for strongly-interacting bosons and non-interacting fermions in rotating optical lattices. These results are based on the notion of quasi-angular momentum, which is a quantum number for systems with a discrete rotational symmetry. Quasi-angular momentum is analogous to quasi-momentum for periodic translationally invariant systems and has been previously used in the context of rotating ring lattices [19, 20, 126] and carbon nanotubes [105] to label eigenstates. A formalism for this quantum number for second-quantized systems is presented here and applied to gases of bosons and fermions in rotating optical lattices. We identify transitions between states of different symmetry for the ground state of a rotating system. A possible avenue for experimentally detecting these results via the momentum distribution of the ground state is presented.

The chapter is structured as follows. In section 3.1, we draw the analogy between systems with a discrete translational symmetry and systems with a discrete rotational symmetry, thereby generating a Bloch theory for the latter and introducing the notion of quasi-angular momentum. The theory of one particle on a rotating ring lattice is used to illustrate these ideas in section 3.2. This is extended to a many-body description in section 3.3, where a many-particle, tight-binding model is diagonalized. Specific investigations of quantum gases of strongly-interacting bosons and non-interacting fermions in ring and square lattice geometries are carried out in section 3.4. In section 3.5, signatures of the quasi-angular momentum in the momentum distribution of a state are identified. Finally, section 3.6 summarizes the main results of this chapter.

## 3.1 Bloch Theory for Systems With Discrete Rotational Symmetry

The concepts discussed in section 2.1 hold for systems with symmetries other than discrete translational symmetry. We can see this by investigating the fact that a moving $N$-site linear lattice with periodic boundary conditions is analogous to a rotating $N$-site

ring lattice. We can make this analogy explicit by considering the Hamiltonian of a moving, one-dimensional, sinusoidal $N$-site lattice in the co-moving frame, given by

$$H(x) = -\frac{\hbar^2}{2M}\frac{\partial^2}{\partial x^2} + V_0 \cos^2(qx) - v\frac{\hbar}{i}\frac{\partial}{\partial x}, \tag{3.1}$$

where $v$ is the velocity of the lattice. In this expression, we have used the fact that in a moving frame,

$$\hat{H} = \hat{H}_0 - \hat{\mathbf{p}} \cdot \mathbf{v}, \tag{3.2}$$

where $\hat{H}_0$ is the time-independent Hamiltonian in the non-moving frame, and $\mathbf{v}$ is the velocity of the moving frame with respect to the lab frame [69].

The lattice wave-number $q$ can be rewritten as $q = \pi/d$, where $d$ is the lattice spacing. If periodic boundary conditions,

$$\psi(x + Nd) = \psi(x), \tag{3.3}$$

are included, then the Hamiltonian describes the system illustrated in figure 3.1(a) for the explicit case of an 8-site lattice. On the other hand, the Hamiltonian of a rotating, sinusoidal $N$-site ring lattice (figure 3.1(b)) is given in the rotating frame by

$$H(\phi) = -\frac{\hbar^2}{2M}\frac{1}{R^2}\frac{\partial^2}{\partial \phi^2} + V_0 \cos^2\left(N\frac{\phi}{2}\right) - \Omega\frac{\hbar}{i}\frac{\partial}{\partial \phi}, \tag{3.4}$$

where $\Omega$ is the rotation frequency, and $R$ is the radius of the ring. The inclusion of the term $-\Omega L_z$ has the effect of moving to a frame co-rotating with the lattice [69]. The two Hamiltonians, equations (3.1) and (3.4), are mathematically identical if we perform a transformation $x = \phi N d/2\pi$ and identify $Nd/2\pi$ with $R$ and $v/R$ with $\Omega$.

Since the Hamiltonians are exactly identical, all of the properties of one-dimensional systems with a discrete translational invariance carry over for ring systems with a discrete rotational invariance. The analogy can be carried further, starting with the two-dimensional free-space solution in polar coordinates,

$$\psi_j(\phi, \rho) = e^{ij\phi} R_j(\rho), \tag{3.5}$$

where $R_j(\rho)$ is a radial function, irrelevant for our discussion, and $j$ is an integer. In the presence of a potential that breaks the rotational symmetry, the eigenstates are linear combinations of these free-space solutions. If this potential has a discrete $N$-fold rotational symmetry, its eigenstates can be expanded in the free space solutions as

$$\psi_m(\phi,\rho) = \sum_{j=-\infty}^{\infty} a_j^{(m)} \frac{e^{i(Nj+m)\phi}}{\sqrt{N\pi}} R_j(\rho). \tag{3.6}$$

It is evident from this expansion that

$$\psi_m(\phi - \frac{2\pi}{N},\rho) = \sum_{j=-\infty}^{\infty} a_j^{(m)} \frac{e^{i(Nj+m)(\phi-2\pi/N)}}{\sqrt{N\pi}} R_j(\rho) = e^{-i2\pi m/N}\psi_m(\phi,\rho). \tag{3.7}$$

and that therefore $\psi_m(\phi,\rho)$ is an eigenvector with eigenvalue $e^{-i2\pi m/N}$ of the discrete rotation operator $R_{2\pi/N}$ that rotates the system by the angle $2\pi/N$; $R_{2\pi/N}$ takes the place of the discrete translation operator, $T_d$. The analogy is complete when we note that the eigenstates are linear combinations of angular momentum eigenstates, in which case we call the number $\hbar m$ the quasi-angular momentum of the state, $\psi_m(\phi,\rho)$. For simplicity, we drop the factor of $\hbar$ and call the value $m$ the quasi-angular momentum.

## 3.2 Single Particle on a Rotating Ring Lattice

As an application of the discussions in the previous section, we examine the problem of a single particle trapped on a rotating ring lattice. This problem is analytically solvable in terms of Mathieu functions, and we can examine the effects of rotation on both the spectrum and the eigenstates.

The Hamiltonian for a single particle trapped on a rotating ring lattice is given by equation (3.4). The $N$ lattice sites are situated at

$$(\rho_j,\phi_j) = \left(R, \frac{2\pi n_j}{N}\right), \tag{3.8}$$

where $j = 1,\ldots,N$. To simplify the problem, we make a transformation $\phi \to 2\phi/N$ ($\phi \in [0, N\pi]$) and scale energies by the "recoil energy",

$$E_R = \frac{\hbar^2}{2m}\left(\frac{N}{2R}\right)^2 = \frac{\hbar^2}{2m}\left(\frac{\pi}{d}\right)^2. \tag{3.9}$$

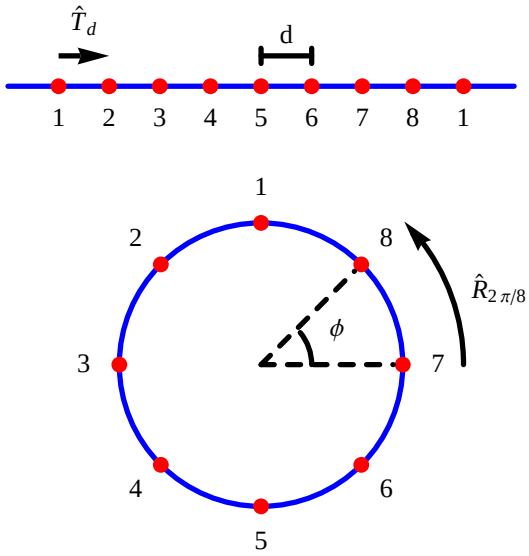


Figure 3.1: Equivalence between a ring lattice and a one-dimensional lattice with periodic boundary conditions. The translation operator $\hat{T}_d$ that translates through one lattice site maps onto the rotation operator $\hat{R}_{2\pi/8}$ that rotates the lattice through one lattice site.

In this case, the Schrödinger equation is given by

$$E\psi(\phi) = E_R\left(-\frac{\partial^2}{\partial\phi^2} + i\frac{N}{2}\omega\frac{\partial}{\partial\phi} + \frac{v_0}{2}\cos(2\phi) + \frac{v_0}{2}\right)\psi(\phi), \tag{3.10}$$

where $\omega = \hbar\Omega/E_R$, $v_0 = V_0/E_R$, and $\psi(\phi - N\pi) = \psi(\phi)$.

In order to take into account the effect of rotation, we "imprint" an angular momentum on the wave function that coincides with the rotation rate, i.e.

$$\psi(\phi) = e^{i\phi\omega N/4}\varphi(\phi). \tag{3.11}$$

In this case, the Schrödinger equation becomes

$$E\varphi(\phi) = E_R\left(-\frac{\partial^2}{\partial\phi^2} + \frac{v_0}{2}\cos(2\phi) + \frac{v_0}{2} - \omega^2\frac{N^2}{16}\right)\varphi(\phi). \tag{3.12}$$

Defining

$$a = \frac{E}{E_R} - \frac{v_0}{2} + \frac{\omega^2 N^2}{16}, \tag{3.13}$$

$$t = \frac{v_0}{4}, \tag{3.14}$$

this equation may be re-written as

$$0 = \frac{\partial^2}{\partial\phi^2}\varphi(\phi) + (a - 2t\cos(2\phi))\varphi(\phi). \tag{3.15}$$

This is exactly Mathieu's equation. See appendix A for a discussion of the solutions of this equation.

### 3.2.1 Effects of rotation

We know that the eigenfunctions, $\psi_m^{(n)}(\phi)$, of equation (3.15) should satisfy

$$\psi_m^{(n)}(\phi - \pi) = e^{-i2\pi m/N}\psi_m^{(n)}(\phi). \tag{3.16}$$

In this case,

$$\psi_m^{(n)}(\phi) = e^{i\phi\omega N/4}\varphi_q^{(n)}(\phi). \tag{3.17}$$

Thus,

$$e^{-i2\pi m/N}\psi_m^{(n)}(\phi) = \psi_m^{(n)}(\phi - \pi) = e^{-i\pi(q+\omega N/4)}\psi_m^{(n)}(\phi). \tag{3.18}$$

The quantity $q$ is then a function of the quasi-angular momentum number $m$ and the rotation rate $\omega$, given by

$$q \to q_m(\omega) = \mathrm{mod}_2\left(\frac{2m}{N} - \frac{\omega N}{4} + 1\right) - 1, \tag{3.19}$$

in which case

$$\psi_m^{(n)}(\phi) = e^{i\phi\omega N/4}\left(C^{(n)}_{q_m(\omega)}(\phi) + i\ \mathrm{Sign}(q) S^{(n)}_{q_m(\omega)}(\phi)\right), \tag{3.20}$$

where $C$ and $S$ are Mathieu cosine and sine functions.

We can make two interesting observations about this solution. First, apart from the integer values of $q_m(\omega)$, we may write the energy of one of the quasi-angular momentum states as

$$E_m^{(n)}(\omega) = E_R\left(a_{k_{n,q_m(\omega)}} + \frac{v_0}{2} - \frac{\omega^2 N^2}{16}\right). \tag{3.21}$$

Let's consider the ground state of the system. At $\omega = 0$, this is clearly the state $\psi_0^{(1)}(\phi)$ since

$$q_0(0) = 0 \Longrightarrow a_{k_{n,q_m(\omega)}} = a_0, \tag{3.22}$$

which is the smallest Mathieu characteristic value. However, when, say, $\omega = \frac{8}{N^2}$, we can see from equation (3.19) that

$$|q_0(\omega)| = \left|\mathrm{mod}_2\left(-\frac{2}{N} + 1\right) - 1\right| \geq 0, \tag{3.23}$$

$$|q_1(\omega)| = |\mathrm{mod}_2(1) - 1| = 0. \tag{3.24}$$

The $m = 1$ quasi-angular momentum state is now the ground state. It is clear from equation (3.19) that this behavior generalizes, and as $\omega$ increases, the ground state cycles through the different quasi-angular momentum states. Since these states do not mix with each other, this is signaled by exact energy level crossings in the spectrum as

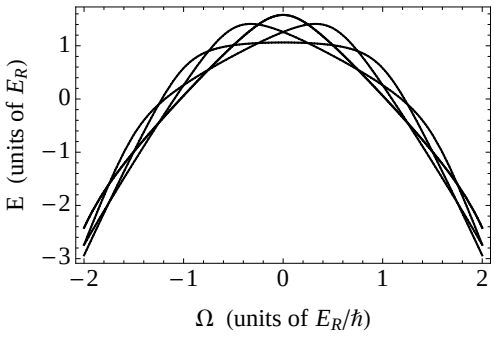


Figure 3.2: Exact energy-level crossings due to rotation for a four-site sinusoidal lattice with periodic boundary conditions. At zero velocity, the zero quasi-momentum state is the ground state. At some finite positive velocity, the $k = \pi/2d$ state is energetically favorable and becomes the ground state. The ground state eventually cycles through all quasi-momenta.

a function of rotation. This is illustrated in figure 3.2, where the $m = -2$, $-1$, 0, and 1 states in the first band for a four-site lattice are plotted as a function of the rotation speed.

This behavior is general, and we can understand it by invoking first-order perturbation theory. In a stationary one-dimensional ring lattice, the zero quasi-angular momentum Bloch function is always the ground state. When the lattice is rotating, the energetically favored state is one that rotates along with the lattice. In order to investigate this phenomenon, we consider the Hamiltonian,

$$\hat{H} = \hat{H}_0 - \Omega \hat{L}_z, \tag{3.25}$$

where $\hat{H}_0$ is the time-independent Hamiltonian in the non-moving frame. The ground state of $\hat{H}$ is the ground state in the lab frame but written in rotating frame coordinates.

We consider an eigenstate of $\hat{H}_0$, $\psi_k(x)$. In first-order perturbation theory, the energy $E_k$ of an eigenstate $\psi_k(x)$ of $\hat{H}_0$ is shifted by the rotation term to

$$E_k = \langle k|\hat{H}_0 - \Omega \hat{L}_z|k\rangle = E_k^{(0)} - \Omega\langle k|\hat{L}_z|k\rangle. \tag{3.26}$$

At zero rotation rate, the ground state is a zero quasi-angular momentum state, $\psi_0(x)$. However, the energy of a state that has a positive average angular momentum, $\langle k|\hat{L}_z|k\rangle >$

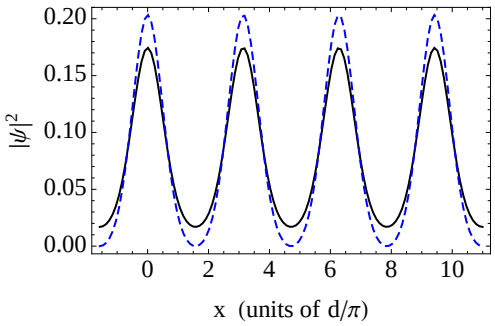


Figure 3.3: The $m = 0$ Bloch function at $\omega = 0$ (black, solid) and $\omega = 1$ (blue, dashed). The Bloch function is squeezed tighter within the wells for larger rotation rates.

0, falls below that of $\psi_0(x)$ for large enough $\Omega$. This change is signaled by an exact energy level crossing in the energy spectrum between two quasi-angular momentum states (see figure 3.2). As the rotation rate is increased, the effect of the rotation term is to reorder the energies of the quasi-momentum states.

The second observation we can make is about the Bloch function solutions themselves. In figure 3.3 are plotted the densities for the $m = 0$ state in the first band for two different rotation speeds. The Bloch function with the larger rotation speed, $\omega = 1$, is more localized to the lattice sites. In fact, we can observe that the ground state is always the state that is least-localized to the lattice sites. This effect may be understood in the following way. A particle that is moving slower than the lattice will be pulled along, effectively "piling up" the wave function against the side of the lattice well. This simultaneously decreases the width of the wave packet within the well and increases the kinetic energy. A particle at the same speed as the lattice will not feel this effect, and its wave function will not be "squeezed" by the lattice wells. This is the physical basis of both the wave function for $m = 0$ being more localized for higher rotation rates and for the exact energy level crossings in the spectrum as a function of rotation.

## 3.3 Many-Body Description of Quasi-Angular Momentum

The symmetry considerations of the previous sections necessarily hold for many-particle systems where the underlying single-particle Hamiltonian has a discrete rotational symmetry. The eigenstates of the many-particle Hamiltonian can then be chosen to be quasi-angular momentum eigenstates. Alternatively, it is sometimes possible to re-cast the symmetry properties of the eigenstates in terms of the creation and annihilation operators in a second quantized formalism. In this section, we examine the special case of a Hubbard Hamiltonian for non-interacting fermions, which for instance describes fermions in a one-dimensional optical lattice in the tight-binding regime.

The Hamiltonian takes the simple form,

$$\hat{H} = \sum_{j=1}^{N} \epsilon \hat{a}_j^\dagger \hat{a}_j - \sum_{j=1}^{N} \left( J^* \hat{a}_{j+1}^\dagger \hat{a}_j + J \hat{a}_j^\dagger \hat{a}_{j+1} \right), \tag{3.27}$$

where $\hat{a}_{N+1} = \hat{a}_1$ in order to satisfy periodic boundary conditions, and

$$\left[ \hat{a}_i, \hat{a}_j^\dagger \right]_+ = \delta_{ij}, \tag{3.28}$$

$$\left[ \hat{a}_i, \hat{a}_j \right]_+ = 0, \tag{3.29}$$

so that the particles are fermions. This Hamiltonian can be diagonalized using operator methods. To this end, we define new fermionic operators by means of

$$\hat{d}_m = \frac{1}{\sqrt{N}} \sum_{k=1}^{N} e^{-i2\pi mk/N} \hat{a}_k, \tag{3.30}$$

$$\hat{a}_k = \frac{1}{\sqrt{N}} \sum_{m=0}^{N-1} e^{-i2\pi mk/N} \hat{d}_m. \tag{3.31}$$

Under this canonical transformation, the on-site energy term becomes

$$\hat{H}_0 = \sum_{j=1}^{N} \epsilon \hat{a}_j^\dagger \hat{a}_j = \epsilon \sum_{m=0}^{N-1} \hat{d}_m^\dagger \hat{d}_m, \tag{3.32}$$

and the hopping term becomes

$$\hat{H}_1 = -2t \sum_{m=0}^{N-1} \hat{d}_m^\dagger \hat{d}_m \cos\left( \frac{2\pi m}{N} - \phi \right), \tag{3.33}$$

where $t$ and $\phi$ are defined by the relation $J = te^{i\phi}$. The eigenstates of this Hamiltonian are then

$$|n_0, \ldots, n_{N-1}\rangle = (d_0^\dagger)^{n_0} \cdots (d_{N-1}^\dagger)^{n_{N-1}}|0\rangle, \tag{3.34}$$

where $|0\rangle$ is the vacuum, $n_m$ can take on the values 0 or 1, and the corresponding eigenvalues are

$$E_{n_0,\ldots,n_{N-1}} = \sum_{m=0}^{N-1} n_m \left(\epsilon - 2t\cos(\frac{2\pi m}{N} - \phi)\right). \tag{3.35}$$

As we can see from its solutions, this Hamiltonian is exactly the many-body generalization of the tight-binding model for atoms hopping around a one-dimensional lattice.

From the expansion of $\hat{d}_m^\dagger$ in the $\hat{a}_k^\dagger$'s we can see that $d_m^\dagger$ adds one particle to the system, populating each site with equal probability but differing phase. We can conclude that particles created by $\hat{d}_m^\dagger$ carry quasi-angular momentum. To make this statement exact, we define a discrete rotation operator $\hat{R}$ by

$$\hat{R}\hat{a}_k^\dagger\hat{R}^{-1} = \hat{a}_{k+1}^\dagger, \tag{3.36a}$$

$$\hat{R}|0\rangle = |0\rangle. \tag{3.36b}$$

This operator commutes with the Hamiltonian, and acting it on $\hat{d}_m$ yields

$$\begin{aligned}\hat{R}\hat{d}_m^\dagger\hat{R}^{-1} &= \frac{1}{\sqrt{N}}\sum_{k=1}^{N} e^{i2\pi mk/N}\hat{R}\hat{a}_k^\dagger\hat{R}^{-1} = \frac{1}{\sqrt{N}}\sum_{k=1}^{N} e^{-i2\pi m/N}e^{i2\pi m(k+1)/N}\hat{a}_{k+1}^\dagger \\ &= e^{-i2\pi m/N}\hat{d}_m^\dagger.\end{aligned} \tag{3.37}$$

Therefore,

$$\hat{R}(d_1^\dagger)^{n_1}\cdots(d_N^\dagger)^{n_N}|0\rangle = \exp\left(-i2\pi\sum_{m=0}^{N-1}\frac{mn_m}{N}\right)(d_1^\dagger)^{n_1}\cdots(d_N^\dagger)^{n_N}|0\rangle. \tag{3.38}$$

This state carries quasi-angular momentum,

$$m = \mathrm{mod}_N\left(\sum_{m=1}^{N} mn_m\right). \tag{3.39}$$

A pictorial representation of this discussion is shown in figure 3.4 for the specific case of one particle in an eight-site ring lattice.

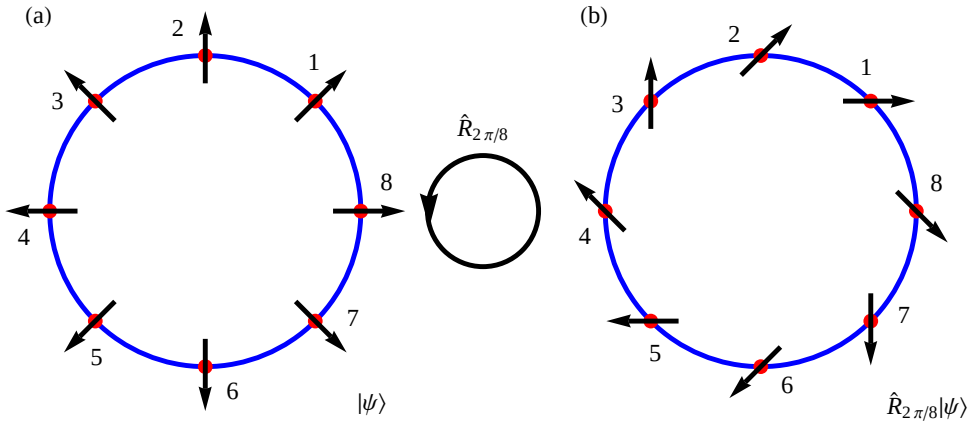


Figure 3.4: Illustration of the rotation operator in the many-body formalism. (a) The operator $\hat{d}_1^\dagger$ adds one particle to the system, populating every site with equal probability but a phase that differs by $2\pi/8$ between lattice sites. The state that is illustrated is $|\psi\rangle = \hat{d}_1^\dagger |0\rangle$; arrows indicate phase. (b) When this state is rotated by one lattice site, the resulting state is $\hat{R}_{2\pi/8}|\psi\rangle$. Subtracting the phases at a site before and after rotation, we get $\phi = -2\pi/8$. The picture then illustrates the fact that $|\psi\rangle$ is an eigenstate of $\hat{R}_{2\pi/8}$ with eigenvalue $e^{-i2\pi/8}$.

Armed with an understanding of the eigenstates of this system, it is straightforward to compute physical quantities such as the energy. The ground state of the system is particularly easy to find, as we simply populate the lowest energy levels to create a "Fermi sea".

If there is an additional potential that reduces the symmetry of the problem, quasi-angular momentum can still be exploited to simplify the problem. The $\hat{d}_m$ operators act as a natural basis in which to describe problems that have some rotational symmetry. For instance, we can consider an additional potential that is some arbitrary function of the creation and annihilation operators on an $N$-site lattice,

$$\hat{V} = \sum_{j,k=1}^{N} V_{jk} \hat{d}_j^\dagger \hat{d}_k, \tag{3.40}$$

with $V_{jk} = V_{kj}^*$. We suppose for simplicity that this potential is only 4-fold symmetric, i.e. it is symmetric under rotation by $N/4$ sites, effected by the operator $\hat{R}^{N/4}$. This limits the possible terms $\hat{d}_j^\dagger \hat{d}_k$ that can appear, which we can see by computing

$$\hat{R}^{N/4} \hat{V} \hat{R}^{-N/4} = \sum_{j,k=1}^{N} V_{jk} \hat{R}^{N/4} \hat{d}_j^\dagger \hat{R}^{-N/4} \hat{R}^{N/4} \hat{d}_k \hat{R}^{-N/4} = \sum_{j,k=1}^{N} V_{jk} e^{i\pi 2(j-k)/4} \hat{d}_j^\dagger \hat{d}_k. \tag{3.41}$$

In order for the potential to be invariant under this four-fold rotation, we must have that $e^{i\pi 2(j-k)/4} = 1$, in which case $\mathrm{mod}_4(k-j) = 0$. Any terms involving $\hat{d}_j^\dagger \hat{d}_k$ where this equation is not satisfied are zero. We define

$$k = 4l_1 + m_1, \tag{3.42a}$$

$$j = 4l_2 + m_2, \tag{3.42b}$$

$$l_i = 1, \ldots, N/4, \tag{3.42c}$$

$$m_i = 0, 1, 2, 3, \tag{3.42d}$$

which allows us to write the potential as

$$\hat{V} = \sum_{m=0}^{3} \sum_{l_1,l_2=1}^{N/4} V_{l_1,l_2}^{(m)} \hat{d}_{4l_1+m}^\dagger \hat{d}_{4l_2+m}, \tag{3.43}$$

$$V_{l_1,l_2}^{(m)} = V_{4l_1+m,4l_1+m}. \tag{3.44}$$

This re-writing automatically sorts the operators appearing in $\hat{V}$ according to their four-fold symmetry, which is the one relevant to the new problem. The full Hamiltonian $\hat{H}+\hat{V}$ is then block-diagonal in the four-fold quasi-angular momentum, $m$, making numerical solutions to this problem more tractable. This scheme can be used to facilitate the solution for a system of atoms in a rotating two-dimensional lattice.

## 3.4 Bose and Fermi Gases in Rotating Optical Lattices

Interacting bosons in one dimension enter the Tonks-Girardeau regime when interactions get very strong [45, 75]. The gas takes on many of the characteristics of a gas of non-interacting fermions; for instance, the number density in position space is the same in both cases. It differs in certain aspects, however; for instance, the momentum distribution is more highly peaked about a central value for strongly-interacting bosons than it is for fermions [61]. It then becomes particularly interesting to compare the cases of strongly-interacting bosons and non-interacting fermions in rotating lattices. In this section, gases of non-interacting fermions and hard-core bosons in rotating optical lattices are investigated. The many-particle formalism for quasi-angular momentum states discussed previously is used to monitor the symmetry of the ground state as a function of rotation. The second-quantized Hamiltonians described below are generalizations of those found in reference [37].

The Hamiltonian for interacting bosons or fermions in a rotating, two-dimensional, square, optical lattice is

$$\begin{aligned}\hat{H} = &\sum_{\sigma} \int d^2x \; \hat{\Psi}^{\dagger}_{\sigma}(\mathbf{x}) \left( -\frac{\hbar^2}{2M}\nabla^2 + V_{\mathrm{L}}(\mathbf{x}) - \Omega L_z \right) \hat{\Psi}_{\sigma}(\mathbf{x}) \\ &+ \sum_{\lambda\lambda',\mu\mu'} \int d^2x \int d^Dx' \; \hat{\Psi}^{\dagger}_{\lambda}(\mathbf{x}) \hat{\Psi}^{\dagger}_{\lambda'}(\mathbf{x}') V_{\lambda\lambda',\mu\mu'}(\mathbf{x},\mathbf{x}') \hat{\Psi}_{\mu'}(\mathbf{x}) \hat{\Psi}_{\mu}(\mathbf{x}'), \end{aligned} \tag{3.45}$$

where

$$V_{\mathrm{L}}(\mathbf{x}) = V_0 \cos^2(k_{\mathrm{L}}x) + V_0 \cos^2(k_{\mathrm{L}}y), \tag{3.46}$$

$V_{\lambda\lambda',\mu\mu'}(\mathbf{x},\mathbf{x}')$ is a two-particle interaction that is possibly spin-dependent, $\lambda$, $\mu$, and $\sigma$ are spin indices, and $\hat{\Psi}_\sigma(\mathbf{x})$, $\hat{\Psi}^\dagger_\sigma(\mathbf{x})$ are field operators satisfying the (anti-)commutation relations,

$$\left[\hat{\Psi}_\sigma(\mathbf{x}),\hat{\Psi}^\dagger_{\sigma'}(\mathbf{x}')\right]_\pm = \delta_{\sigma\sigma'}\delta(\mathbf{x}-\mathbf{x}'), \tag{3.47}$$

$$\left[\hat{\Psi}_\sigma(\mathbf{x}),\hat{\Psi}_{\sigma'}(\mathbf{x}')\right]_\pm = 0. \tag{3.48}$$

The two-particle interaction Hamiltonian, $V_{\lambda\lambda',\mu\mu'}(\mathbf{x},\mathbf{x}')$, is chosen to be an $s$-wave contact-interaction.

A Hubbard Hamiltonian can be derived in a lowest-band, tight-binding approximation by expanding the field operators in the lowest-band Wannier functions, $w(\mathbf{x}-\mathbf{x}_j)$ [64]. A basis better suited in the presence of rotation is given by the modified Wannier functions,

$$W_j(\mathbf{x}) = \exp\left(-i\frac{M}{\hbar}\int_{\mathbf{x}_j}^{\mathbf{x}}\mathbf{A}(\mathbf{x}')\cdot d\mathbf{x}'\right)w(\mathbf{x}-\mathbf{x}_j), \tag{3.49}$$

where $\mathbf{A}(\mathbf{x}') = \boldsymbol{\Omega}\times\mathbf{x}'$. This modification captures the effect of rotation at low rotation speeds [11]. However, as we have seen, at higher rotation speeds, the density of the Wannier functions changes along with the phase, and in this case the approximation needs to be further modified.

The result for spinless bosons is [10]

$$\begin{aligned}\hat{H}_{\mathrm{B}} = &-\sum_{\langle i,j\rangle}\left(J+\frac{1}{2}M\Omega^2A_1\right)\left(e^{-i\phi_{ij}}\hat{a}_i^\dagger\hat{a}_j+e^{i\phi_{ij}}\hat{a}_j^\dagger\hat{a}_i\right)\\ &+\sum_j\left(\epsilon-\frac{1}{2}M\Omega^2\left(r_j^2+A_2\right)\right)\hat{a}_j^\dagger\hat{a}_j+\frac{U}{2}\sum_j\hat{a}_j^\dagger\hat{a}_j^\dagger\hat{a}_j\hat{a}_j.\end{aligned} \tag{3.50}$$

A similar derivation for spin-1/2 fermions yields

$$\begin{aligned}\hat{H}_{\mathrm{F}} = &-\sum_{\langle i,j\rangle,\sigma}\left(J+\frac{1}{2}M\Omega^2A_1\right)\left(e^{-i\phi_{ij}}\hat{a}_{i,\sigma}^\dagger\hat{a}_{j,\sigma}+e^{i\phi_{ij}}\hat{a}_{j,\sigma}^\dagger\hat{a}_{i,\sigma}\right)\\ &+\sum_{j,\sigma}\left(\epsilon-\frac{1}{2}M\Omega^2\left(r_j^2+A_2\right)\right)\hat{a}_{j,\sigma}^\dagger\hat{a}_{j,\sigma}+\frac{U}{2}\sum_j\hat{a}_{j,\uparrow}^\dagger\hat{a}_{j,\downarrow}^\dagger\hat{a}_{j,\downarrow}\hat{a}_{j,\uparrow}.\end{aligned} \tag{3.51}$$

For both cases, $i, j$ are site indices with $\langle i, j\rangle$ indicating a sum over only nearest neighbors, and $r_i$ is the radial position of the $i$'th site. The phase $\phi_{ij}$ is given by the expression,

$$\phi_{ij} = \frac{M}{\hbar}\int_{\mathbf{x}_j}^{\mathbf{x}_i} \mathbf{A}(\mathbf{x}')\cdot d\mathbf{x}' = \frac{M\Omega}{\hbar}(x_i y_j - x_j y_i). \tag{3.52}$$

The parameters $\epsilon$, $J$, and $U$ are the on-site zero-point energy, the hopping parameter, and the on-site interaction energy, respectively, as computed in chapter 2. The parameters $A_1$ and $A_2$ arise due to the phase factor in equation (3.49) and are given by

$$A_1 = \int dx\ w^*(x - x_i)(x - x_i)^2 w(x - x_j), \tag{3.53}$$

$$A_2 = 2\int dx\ w^*(x - x_i)(x - x_i)^2 w(x - x_i), \tag{3.54}$$

where $w(x - x_i)$ are one-dimensional Wannier functions. All of these parameters can be numerically evaluated for a lattice of specific shape, period, and depth [10]. If a harmonic trap of trapping frequency $\Omega_T$ is included, we replace every instance of $\Omega^2$ with $\Omega^2 - \Omega_T^2$.

### 3.4.1 Strongly-interacting bosons

In this section, we describe hard-core bosons in a rotating ring lattice. The quasi-angular momentum of an eigenstate for a one-dimensional system is then defined and monitored as a function of rotation speed. The analytic results derived here are consistent with a previous numerical treatment of a two-dimensional system [11].

In the limit of very strong interactions, $U \to \infty$, a gas of bosons enters the hard-core boson regime. In an optical lattice, this regime can be characterized by using a number basis where the occupation number of each site is either $l$ or $l + 1$, with $l$ an integer. We define new operators $\hat{b}_j$ that satisfy the relations,

$$\left[\hat{b}_j, \hat{b}_j^\dagger\right]_+ = 1, \tag{3.55a}$$

$$\left[\hat{b}_j, \hat{b}_j\right]_- = 0, \tag{3.55b}$$

$$\left[\hat{b}_{i\neq j}, \hat{b}_j^\dagger\right]_- = 0. \tag{3.55c}$$

and

$$\hat{a}_j^\dagger \hat{a}_j = \hat{b}_j^\dagger \hat{b}_j + l, \tag{3.56a}$$

$$\hat{a}_j^\dagger \hat{a}_{j\pm1} = (l+1)\hat{b}_j^\dagger \hat{b}_{j\pm1}. \tag{3.56b}$$

The particles described by these operators have boson-like properties except for the fact that no more than one particle can occupy a single site, which is enforced by equation (3.55a). In terms of these new operators, the Hamiltonian for hard-core bosons on a ring lattice is given by

$$\begin{aligned}\hat{H} = U\frac{1}{2}Nl(l-1) + Ul\sum_{j=1}^{N}\hat{b}_j^\dagger\hat{b}_j + \sum_{j=1}^{N}\epsilon(\omega)\hat{b}_j^\dagger\hat{b}_j \\ - J(l+1)\sum_{j=1}^{N}e^{-i\pi\omega N/4}\hat{b}_j^\dagger\hat{b}_{j+1} + \text{H.c.},\end{aligned} \tag{3.57}$$

where

$$\epsilon(\omega) = \epsilon - \frac{N^2\omega^2}{16}. \tag{3.58}$$

The first two terms respectively represent the energy of a particle on site $j$ interacting with the $l$ particles already there and the interaction energy of the $l$ particles on site $j$ summed over all sites. For practical purposes, $U = 100J$, where $J$ is the tunneling energy, is large enough to enter this regime [11].

The mixed commutation/anti-commutation relations of equation (3.55) make this Hamiltonian hard to interpret, since we have neither bosons nor fermions. However, for one-dimensional problems of this sort, we can perform a second transformation of the annihilation operators that transforms this Hamiltonian into a purely fermionic one. This is called the Jordan-Wigner (JW) transformation.

The essence of this transformation is to include a factor of $\pm1$ in the definition of $\hat{b}_j$, where the sign depends on the number of particles to the "left" of the site $j$. It is standard to first map this Hamiltonian onto an $N$-spin-$\frac{1}{2}$ Hamiltonian [66, 116], but we prefer to work strictly with the creation and annihilation operators.

The JW transformation is given by defining new annihilation operators,

$$\hat{c}_j = \hat{b}_j e^{i\pi \sum_{i=1}^{j-1} \hat{b}_i^\dagger \hat{b}_i}, \tag{3.59}$$

These operators are fermionic, as we show in appendix A. The Hamiltonian can then be written as

$$\begin{aligned}\hat{H} = U\frac{1}{2}Nl(l-1) + Ul\sum_{j=1}^{N}\hat{c}_j^\dagger\hat{c}_j + \sum_{j=1}^{N}\epsilon(\omega)\hat{c}_j^\dagger\hat{c}_j \\ - J(l+1)\sum_{j=1}^{N-1} e^{-i\pi\omega N/4}\hat{c}_j^\dagger\hat{c}_{j+1} + \text{H.c.} \\ - J(l+1)e^{-i\pi\omega N/4}\hat{c}_N^\dagger\hat{c}_1(-1)^{\hat{N}+1} + \text{H.c.}\end{aligned} \tag{3.60}$$

This Hamiltonian is manifestly not strictly quadratic in the $\hat{c}$ operators since $\hat{N}$ appears in an exponential. However, as we will soon see, the fact that $\hat{N}$ is conserved allows us to diagonalize the Hamiltonian in even- and odd-number particle subspaces separately.

Before we move on, we note that for two-dimensional lattices, the remaining phase factors are non-trivial, and therefore the JW transformation is not useful in this case.

#### 3.4.1.1 Diagonalization

The Hamiltonian just derived has a form identical to that of equation (3.27) except for the factor of $(-1)^{\hat{N}+1}$. This factor is a constant within a constant particle-number subspace. For this reason, we replace this factor with $(-1)^{n+1}$, where $n$ is the number of particles, and diagonalize $\hat{H}$ as if it were subspace-independent, resulting in two separate sets of fermionic operators. At the end of the derivation, we describe how the normal picture of fermionic excitations is modified by this procedure.

We modify the definition of the operators form section 3.3, defining two sets of

fermionic operators as

$$\hat{d}_m^{(o)} = \frac{1}{\sqrt{N}} \sum_{j=1}^{N} e^{-i\pi 2mj/N} \hat{c}_j, \tag{3.61}$$

$$\hat{d}_m^{(e)} = \frac{1}{\sqrt{N}} \sum_{j=1}^{N} e^{-i\pi (2m-1)j/N} \hat{c}_j. \tag{3.62}$$

The Hamiltonian in terms of the $\hat{d}_m$ operators is given by

$$\hat{H} = U\frac{1}{2}Nl(l-1) + \sum_{m=0}^{N-1} E_m \hat{d}_m^{(\sigma)\dagger} \hat{d}_m^{(\sigma)}, \tag{3.63a}$$

$$E_m = Ul + \epsilon - \frac{N^2\omega^2}{16} - 2(l+1)t\cos\left(\frac{\pi f_m}{N} - \frac{\pi N}{4}\omega\right), \tag{3.63b}$$

$$f_m = \begin{cases} 2m-1 & \text{if} \quad n = \text{even} \\ 2m & \text{if} \quad n = \text{odd} \end{cases}, \tag{3.63c}$$

where $n$ is the number of particles, and $\sigma = e$ for $n$ even and $\sigma = o$ for $n$ odd.

The eigenstates of the system are given by

$$|n_0, \ldots, n_{N-1}\rangle = \begin{cases} \left(\hat{d}_0^{(e)\dagger}\right)^{n_0} \cdots \left(\hat{d}_{N-1}^{(e)\dagger}\right)^{n_{N-1}} |0\rangle & \text{if} \quad \sum_{m=0}^{N-1} n_j = \text{even} \\ \left(\hat{d}_0^{(o)\dagger}\right)^{n_0} \cdots \left(\hat{d}_{N-1}^{(o)\dagger}\right)^{n_{N-1}} |0\rangle & \text{if} \quad \sum_{m=0}^{N-1} n_j = \text{odd} \end{cases}, \tag{3.64}$$

and the corresponding eigenenergies are

$$\begin{aligned} E_{n_0,\ldots,n_N} = {} & U\frac{1}{2}Nl(l-1) \\ & - \sum_{m=0}^{N-1} n_m \left(Ul + \epsilon - \frac{N^2\omega^2}{16} - 2(l+1)t\cos\left(\frac{\pi f_m}{N} - \frac{\pi N}{4}\omega\right)\right). \end{aligned} \tag{3.65}$$

We note that states that mix the two operator definitions are not eigenstates, e.g.

$$|\psi\rangle = \hat{d}_0^{(e)\dagger} \hat{d}_1^{(o)\dagger} |0\rangle \tag{3.66}$$

is not an eigenstate of $\hat{H}$.

In order to complete the diagonalization procedure, we need to interpret $\hat{d}^{(\sigma)\dagger}$ as an operator that creates a particle in the quasi-angular momentum state $m$. As in the previous section, we can do this by first defining a rotation operator. Due to the many phases $e^{i\pi \hat{c}_k^\dagger \hat{c}_k}$ in this problem, it is not *a priori* obvious that the rotation operator

as defined in section 3.3 is a convenient choice for the definition of the quasi-angular momentum. For this reason, we consider the Hamiltonian in terms of the JW fermions, equation (3.60), rather than the original. Defining

$$\hat{R}\hat{c}^\dagger_{j\neq N}\hat{R}^{-1} = \hat{c}^\dagger_{j+1}, \tag{3.67a}$$

$$\hat{R}\hat{c}^\dagger_{N}\hat{R}^{-1} = (-1)^{n+1}\hat{c}^\dagger_{1}, \tag{3.67b}$$

$$R|0\rangle = |0\rangle, \tag{3.67c}$$

we have that

$$\begin{aligned}\hat{R}\hat{d}^\dagger_m\hat{R}^{-1} &= \frac{1}{\sqrt{N}}\sum_{k=1}^{N-1} e^{i\pi f_m k/N}\hat{R}\hat{c}^\dagger_k\hat{R}^{-1} + \frac{1}{\sqrt{N}}e^{i\pi f_m N/N}\hat{R}\hat{c}^\dagger_N\hat{R}^{-1} \\ &= e^{-i\pi f_m/N}\frac{1}{\sqrt{N}}\sum_{k=1}^{N-1} e^{i\pi f_m (k+1)/N}\hat{c}^\dagger_{k+1} \\ &\quad + e^{-i\pi f_m/N}e^{i\pi f_m/N}\frac{1}{\sqrt{N}}e^{i\pi f_m}(-1)^{n+1}\hat{c}^\dagger_1.\end{aligned} \tag{3.68}$$

Noting that $e^{i\pi f_m} = (-1)^{n+1}$, this becomes

$$\begin{aligned}\hat{R}\hat{d}^\dagger_m\hat{R}^{-1} &= e^{-i\pi f_m/N}\frac{1}{\sqrt{N}}\sum_{k=2}^{N} e^{i\pi f_m k/N}\hat{c}^\dagger_k + e^{-i\pi f_m/N}\frac{1}{\sqrt{N}}e^{i\pi f_m/N}\hat{c}^\dagger_1 \\ &= e^{-i\pi f_m/N}\hat{d}^\dagger_m.\end{aligned} \tag{3.69}$$

Thus,

$$\hat{R}\left(d^\dagger_0\right)^{n_0}\cdots(d^\dagger_{N-1})^{n_{N-1}}|0\rangle = \exp\left(-i\frac{\pi}{N}\sum_{m=0}^{N-1} n_m f_m\right)(d^\dagger_0)^{n_0}\cdots(d^\dagger_{N-1})^{n_{N-1}}|0\rangle. \tag{3.70}$$

The quasi-angular momentum of this state is defined to be

$$m = \begin{cases} \mathrm{mod}_N\left(\sum_{m=0}^{N-1} m n_m - \frac{n}{2}\right) & \text{if} \quad n = \text{even} \\ \mathrm{mod}_N\left(\sum_{m=0}^{N-1} m n_m\right) & \text{if} \quad n = \text{odd} \end{cases}. \tag{3.71}$$

#### 3.4.1.2 Results

We are now in a position to use this formalism to investigate the ground state of the system. The ground state is determined by populating the lowest energy levels in

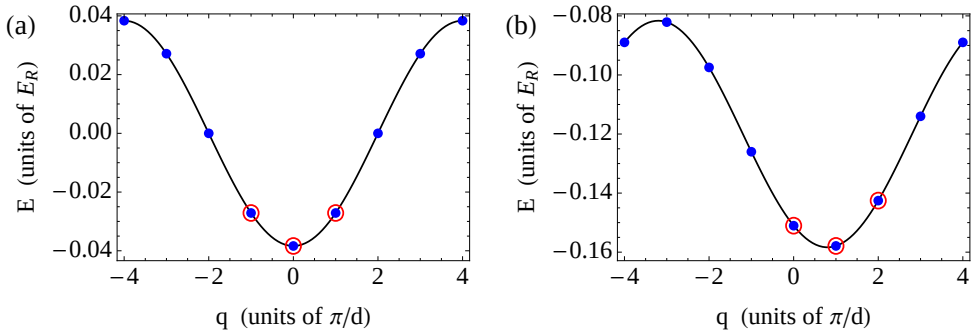


Figure 3.5: Ground state of three strongly-interacting bosons in a rotating 8-site ring lattice. Solid curves are guides for the eye. (a) At $\Omega = 0$, the three lowest single-particle energies carry quasi-angular momentum $m = -1$, 0, and 1. The three-particle ground state therefore has quasi-angular momentum $m = \mathrm{mod}_8(-1+0+1) = 0$. (c) At $\Omega = 0.14E_R/\hbar$, the three lowest single-particle energies carry quasi-angular momentum $m = 0$, 1, and 2. The three-particle ground state therefore has quasi-angular momentum $m = \mathrm{mod}_8(0+1+2) = 3$.

the way standard for fermions. Equation (3.63b) is the single-particle energy spectrum $E_m$. The qualitative behavior of the system does not depend on the filling $l$ and we therefore set $l = 0$; in addition, the zero-point energy $\epsilon$ has no physical effect, so we set it to zero.

As $\omega$ is increased, the minimum value of the cosine moves to the right, as illustrated in figure 3.5. The ground state is then determined by populating the lowest energy $\hat{d}_m^\dagger \hat{d}_m$ eigenstates. In figures 3.5(b) and 3.5(c), this process is illustrated for the case of three particles in an eight-site ring.

For an odd number of particles, $n = 2p+1$, if the minimum of the cosine function in $E_m$ is near $m = m_0$, we populate the states $m_0,\ m_0 \pm 1, \ldots,\ m_0 \pm p$. The quasi-angular momentum of the state is then

$$m = \mathrm{mod}_N \left( \sum_{l=-p}^{p} (m_0 + l) \right) = \mathrm{mod}_N((2p+1)m_0 + 0) = \mathrm{mod}_N(m_0 n). \tag{3.72}$$

For an even number of particles, $n = 2p$, when the minimum of the cosine function is between $m_0$ and $m_0 + 1$, we populate the states $m_0 - p + 1$, $m_0 - p + 2$, $\ldots$, $m_0 + p$.

The quasi-angular momentum of the state is then

$$m = \mathrm{mod}_N \left( \sum_{l=-p+1}^{p} (m_0 + l) - \frac{n}{2} \right) = \mathrm{mod}_N \left( 2pm_0 + p - \frac{n}{2} \right) = \mathrm{mod}_N(m_0 n). \quad (3.73)$$

Thus, as rotation is increased from $\omega = 0$, the quasi-angular momentum cycles through the values,

$$m = \mathrm{mod}_N(jn): \quad j = 0, 1, 2 \ldots \quad (3.74)$$

We make one final note for the case of bosons. If there is an infinitesimal potential, $\hat{V}$, that breaks the symmetry of the original Hamiltonian, $\hat{H}_0$, down to a four-fold rotational symmetry, then the $N$-fold quasi-angular momentum is no longer a good quantum number. We treat the problem perturbatively. Tiny band gaps in the single-particle energy spectrum, equation (3.63b), open up at the new Brillouin zone boundaries. The eigenstates of $\hat{H}_0$ are independent of $\Omega$. Therefore, to first order in $\hat{V}$, the energy level shifts are independent of $\Omega$, and the eigenstates remain unchanged. The effect of rotation is then exactly the same as in the non-perturbed case, and the quasi-angular momenta have the same behavior as a function of rotation. However, since the old quasi-angular momentum is no longer a good quantum number, we have to take

$$m \to \mathrm{mod}_4(m). \quad (3.75)$$

These results are consistent with the numerical treatments in references [9, 11].

### 3.4.2 Non-interacting fermions

Moving beyond the bosonic systems previously studied, we consider non-interacting fermions in rotating optical lattices. Because of the JW mapping, this system should have properties similar to those of the bosonic case. In addition, by considering fermions, we move closer to the system originally displaying quantum Hall physics, that of a two-dimensional gas of electrons moving in the presence of a constant transverse magnetic field.

#### 3.4.2.1 Ring lattice

Here, we describe non-interacting fermions in ring lattices and compare to the boson case. The quasi-angular momentum of the ground state changes as rotation is increased. The allowed values of this quantity for fermions differ from those of the boson case.

For single-species, non-interacting fermions, we drop the spin index, and the Hamiltonian for a ring lattice is given by

$$\hat{H} = \sum_{j=1}^{N} \left( \epsilon - \frac{N^2\omega^2}{16} \right) \hat{c}_j^\dagger \hat{c}_j - J \sum_{j=1}^{N} e^{-i\pi\omega N/4} \hat{c}_{j+1}^\dagger \hat{c}_j + \text{H.c.} \tag{3.76}$$

With the identifications,

$$\epsilon \to \epsilon - \frac{N^2\omega^2}{16}, \tag{3.77a}$$

$$J \to te^{i\pi\omega N/4}, \tag{3.77b}$$

this Hamiltonian is identical to the one discussed in section 3.3, and it can be written in the form

$$\hat{H} = \sum_{m=0}^{N-1} E_m \hat{d}_m^\dagger \hat{d}_m, \tag{3.78a}$$

$$E_m = \epsilon - \frac{N^2\omega^2}{16} - 2t \cos\left( \frac{2\pi m}{N} - \frac{\omega N}{4} \right), \tag{3.78b}$$

$$\hat{d}_m = \frac{1}{\sqrt{N}} \sum_{k=1}^{N} e^{i2\pi mk/N} \hat{c}_k. \tag{3.78c}$$

The calculation of the quasi-angular momentum of an odd particle-number eigenstate is identical to that of equation (3.72). However, for an even particle-number eigenstate, the $n/2$ in equation (3.73) does not appear, and we have

$$m = \text{mod}_N \left( \sum_{l=-p+1}^{p} (m_0 + l) \right) = \text{mod}_N(2pm_0 + p) = \text{mod}_N \left( \left( m_0 + \frac{1}{2} \right) n \right). \tag{3.79}$$

Thus, the quasi-angular momentum assumes the values,

$$m = \begin{cases} \text{mod}_N(nj) & \text{if} \quad n = \text{odd} \\ \text{mod}_N(n(j+1/2)) & \text{if} \quad n = \text{even} \end{cases}, \tag{3.80}$$

as $\omega$ is increased.

As expected, the single-particle cases for both bosons and fermions are identical. It turns out that all cases of odd numbers of particles also coincide. However, there is an interesting distinction between the two cases when the number of particles in the system is even (compare equations (3.73) and (3.79)). For instance, a system of two fermions in a four-site lattice cycles between quasi-angular momenta 1 and 3 whereas a system of two bosons cycles between values 0 and 2. This is one way in which non-interacting fermions and strongly-interacting bosons in one dimension differ despite the JW transformation that maps between the two cases.

#### 3.4.2.2 Two-dimensional square lattice

Differences between fermions and bosons remain when considering two-dimensional systems. Here we describe non-interacting fermions in a two-dimensional $2P \times 2P$ square lattice, which consists of $P$ square ring lattices, as illustrated in figure **??** for $P = 2$.

The Hamiltonian is given by

$$\begin{aligned}\hat{H} = &-\sum_{\langle i,j\rangle}\left(J + \frac{1}{2}M\Omega^2 A_1\right)\left(e^{-i\phi_{ij}}\hat{c}_i^\dagger\hat{c}_j + e^{i\phi_{ij}}\hat{c}_j^\dagger\hat{c}_i\right) \\ &+\sum_j\left(\epsilon - \frac{1}{2}M\Omega^2\left(r_j^2 + A_2\right)\right)\hat{c}_j^\dagger\hat{c}_j. \end{aligned} \tag{3.81}$$

We numerically diagonalize this Hamiltonian for one particle in a 16-site lattice. We then determine the quasi-angular momentum of the ground state as a function of rotation rate for different particle numbers by filling up the lowest-energy states in the way standard for fermions. Since the states are sorted according to their quasi-angular momentum, we can directly compute the quasi-angular momentum of the eigenstate. We illustrate this process for the case of $n$ particles in a sixteen site lattice. In figure 3.6(a) is plotted the single-particle energy spectrum for the Hamiltonian in the absence of hopping between the rings ($\hat{J}_m^{(2,1)} = 0$) and $\Omega = 0$. When the hopping is "turned on" (figure 3.6(b)), level crossings become avoided crossings due to the mixing of states with the same four-fold

quasi-angular momentum. In figure 3.6(c), the case for zero hopping between rings is plotted for $\Omega = 0.05E_R/\hbar$, whereas in figure 3.6(d), the hopping has turned on, and the avoided crossing behavior is again observed.

In figure 3.7 are plotted the quasi-angular momenta of the ground state as a function of rotation speed for non-interacting fermions in a sixteen-site lattice. Similar to the ring lattice case, the results for odd numbers of particles are identical to those for hard-core bosons, but differ for even numbers of particles. There are however other interesting properties that do not appear in the ring lattice case. The most obvious such property in 3.7 is the lack of particle-hole symmetry. The rate at which transitions between quasi-angular momenta occur as a function of rotation speed is much higher for small particle numbers. This is easy to understand once we see that holes have a negative effective mass, meaning that they move in the opposite direction as particles and also seek regions of higher potential. Due to the effective inverse-parabolic potential in the third term of equation (3.81)—a result of the centrifugal barrier—particles are pushed to the outer ring of the lattice whereas holes are pushed to the inner ring. Transitions between quasi-angular momenta occur faster as a function of rotation speed for the outer lattice rings as compared to the inner lattice rings, since the tangential speed of particles is greater at larger radii. Thus, for small particle-numbers (1, 2, 3) where the particles are mostly confined to the outer ring, the transitions occur faster than for large particle numbers (9, 10, 11) where the outer ring is filled, and the dynamics occurs mainly on the inner ring due to Pauli exclusion.

This argument is further verified in figure 3.8, where a strong trapping potential of trap frequency $\Omega_T = 2E_R/\hbar$ reverses the situation. Since $\Omega < \Omega_T$ in this series of plots, the particles are first attracted to the center of the lattice, so that the dynamics for small numbers of particles occur on the inner ring, and thus the transitions between quasi-angular momentum states occur further apart in rotation rate. Finally, in figure 3.9 where we include a trapping potential with $\Omega_T = \Omega$ so that the lattice is flat at

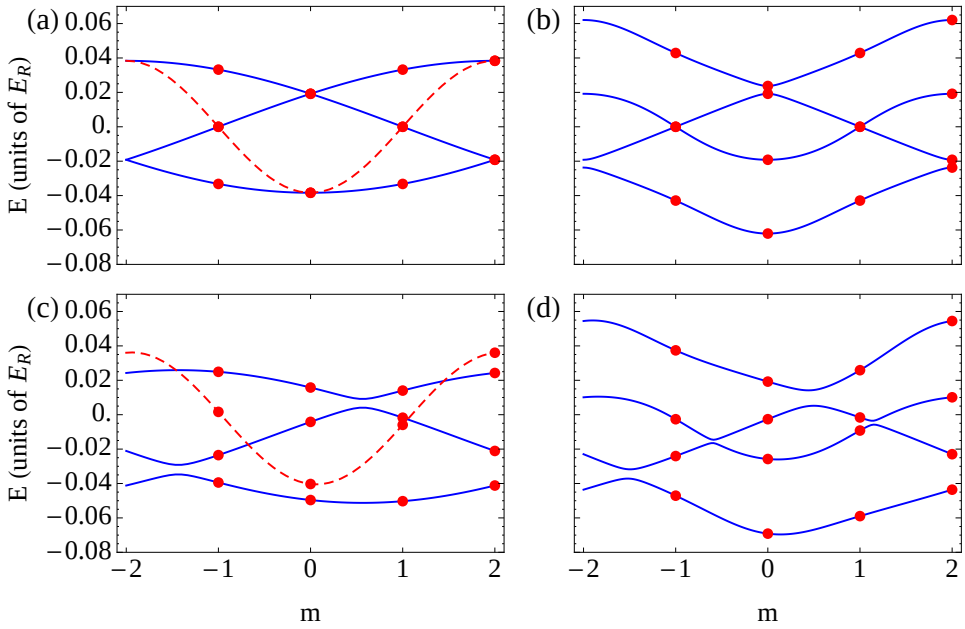


Figure 3.6: Single-particle energy spectrum in a $4 \times 4$ square lattice for (a) zero rotation and zero hopping between inner and outer rings, (b) zero rotation and non-zero hopping, (c) $\Omega = 0.05E_R/\hbar$ and zero hopping, and (d) $\Omega = 0.05E_R/\hbar$ and non-zero hopping between inner and outer rings. The dashed and solid line are aids to the eye that indicate the band. In (a) and (c), the red dashed line is the spectrum for the inner 4-site lattice.

all rotation speeds, the system exhibits particle-hole symmetry up to the fact that particles and holes travel in opposite azimuthal directions. This can be seen by for instance comparing figures 3.9(a) and 3.9(e) where the plots are identical up to the fact that they cycle through quasi-angular momenta in opposite directions as a function of rotation speed.

The case of $\Omega_T = \Omega$ is particularly important for quantum Hall physics, as this is the condition necessary to reach the degenerate lowest Landau level. In this regime, phenomena such as the Hofstadter butterfly energy spectrum and the quantized resistance characteristics of quantum Hall systems arise [10].

## 3.5 Experimental Signatures of Quasi-Angular Momentum

While the quasi-angular momentum $m$ is a good quantum number and a useful tool in investigating the symmetry properties of the ground state, it is not a quantity that can be directly measured in experiments. Instead, experiments are routinely performed in which time-of-flight, far-field, density images of the gas contain information about the momentum distribution before expansion. As a first step towards detecting quasi-angular momentum states, we look for a signature of quasi-angular momentum in the momentum distribution of a state.

The momentum distribution of the many-body state, $|\psi\rangle$, is given by

$$n(\mathbf{k}) = \langle\psi|\hat{\Psi}^\dagger(\mathbf{k})\hat{\Psi}(\mathbf{k})|\psi\rangle, \tag{3.82}$$

where $\hat{\Psi}(\mathbf{k})$ is the Fourier transform of the field operator $\hat{\Psi}(\mathbf{x})$. Recalling that we expand the field operators as

$$\hat{\Psi}(\mathbf{x}) = \sum_j \hat{a}_j W_j(\mathbf{x}) = \sum_j \hat{a}_j e^{-i\phi_{ij}} w(\mathbf{x} - \mathbf{x}_j), \tag{3.83}$$

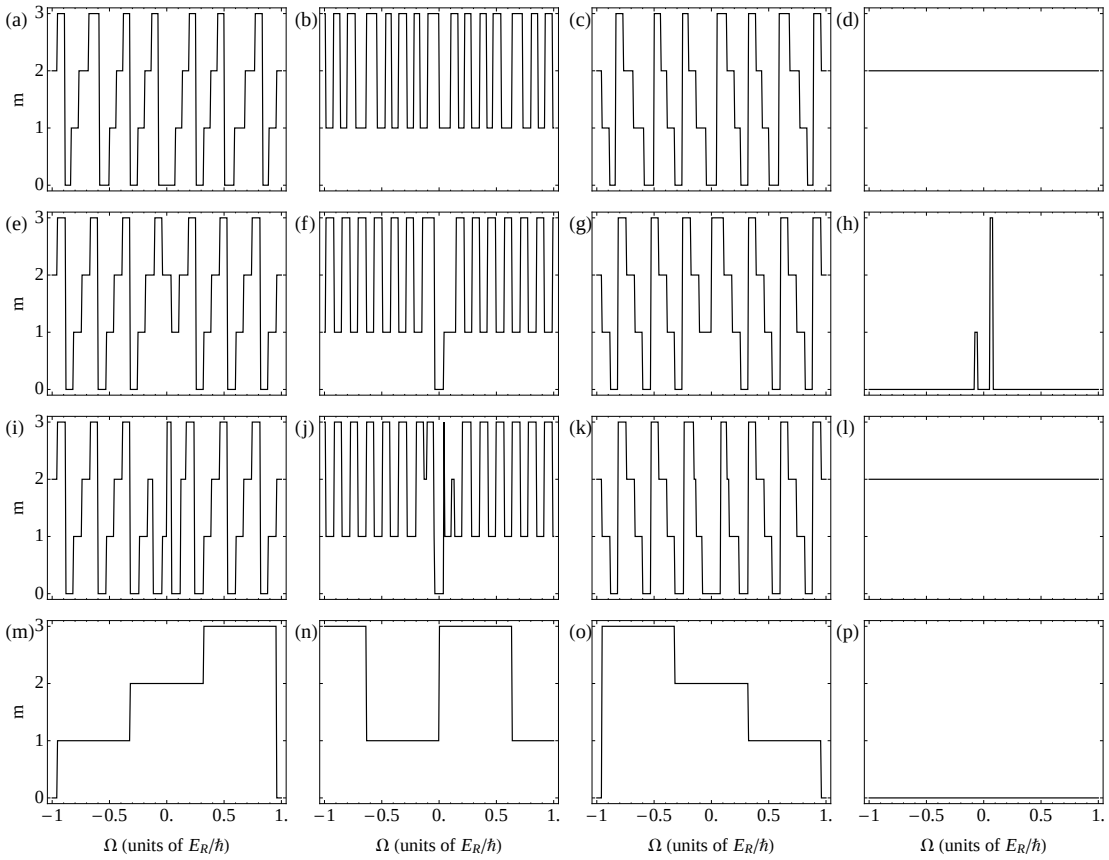


Figure 3.7: Quasi-angular momentum as a function of rotation for 1 - 16 particles in a sixteen-site lattice in the absence of a trapping potential. The number of particles is (a) 1, (b) 2, (c) 3, etc.

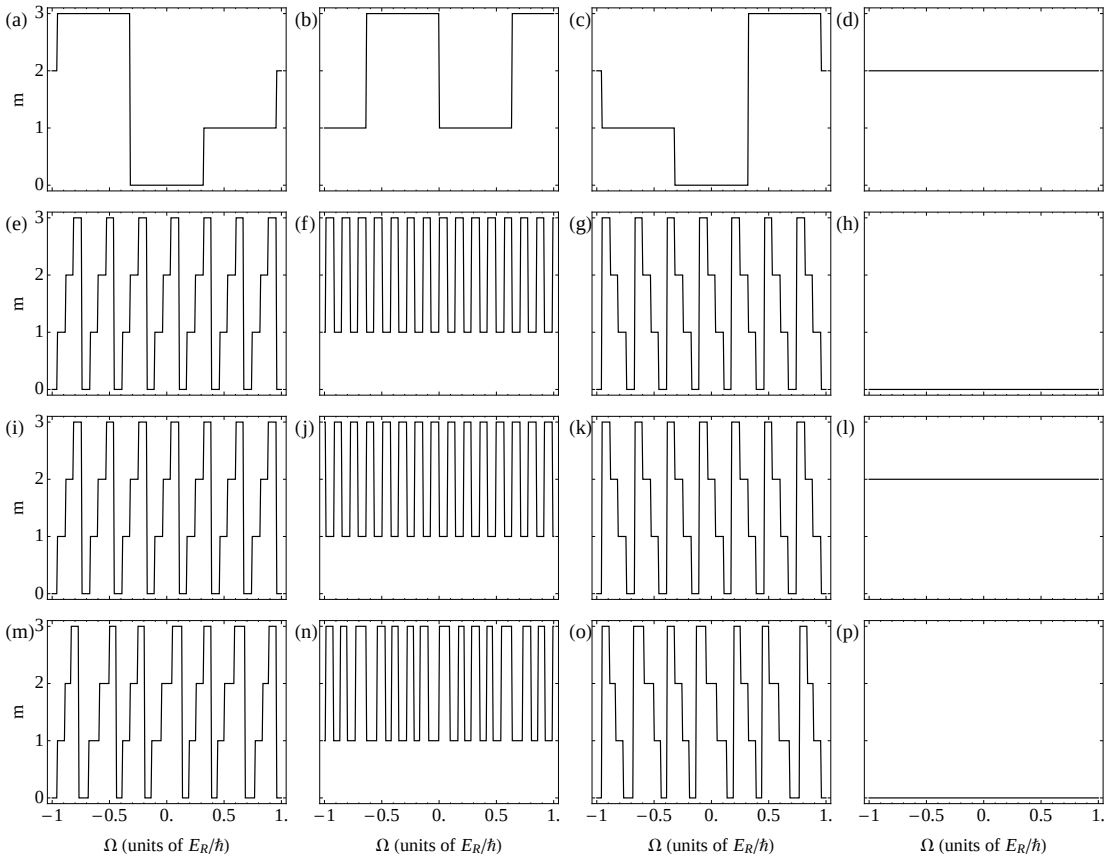


Figure 3.8: Quasi-angular momentum as a function of rotation for 1 - 16 particles in a sixteen-site lattice in the presence of a strong trapping potential, $\hbar\Omega_T = 2E_R$. The number of particles is (a) 1, (b) 2, (c) 3, etc.

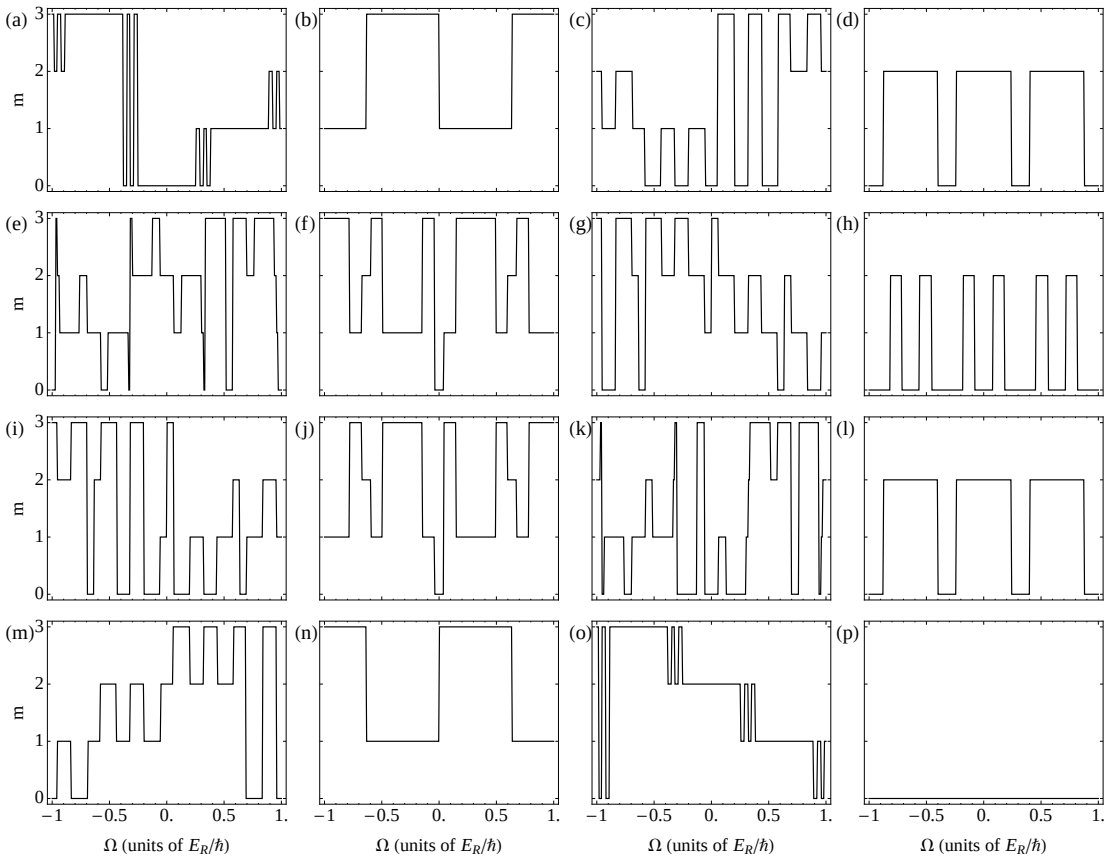


Figure 3.9: Quasi-angular momentum as a function of rotation for 1 - 16 particles in a sixteen-site lattice in the presence of a trapping potential equal in strength to the effective centrifugal potential: $\Omega_T = \Omega$. The number of particles is (a) 1, (b) 2, (c) 3, etc.

we have

$$\begin{aligned} n(\mathbf{k}) &= \langle\psi|\Phi^\dagger(\mathbf{k})\Phi(\mathbf{k})|\psi\rangle \\ &= \langle\psi|\int d^2x\ \frac{e^{i\mathbf{k}\cdot\mathbf{x}}}{\sqrt{V}}\sum_l \hat{a}_l^\dagger W_l^*(\mathbf{x})\int d^2x'\ \frac{e^{-i\mathbf{k}\cdot\mathbf{x}'}}{\sqrt{V}}\sum_{l'}\hat{a}_{l'}W_{l'}(\mathbf{x}')|\psi\rangle \\ &= \sum_{ll'}\langle\psi|\hat{a}_l^\dagger\hat{a}_{l'}|\psi\rangle W_l^*(\mathbf{k})W_{l'}(\mathbf{k}). \end{aligned} \tag{3.84}$$

Defining

$$\mathbf{k}_l = \mathbf{k} + \Omega\frac{M}{\hbar}\mathbf{x}_l\times\hat{z}, \tag{3.85}$$

the modified Wannier function can be re-written as

$$W_l(\mathbf{k}) = e^{-i\mathbf{k}\cdot\mathbf{x}_l}w(\mathbf{k}_l), \tag{3.86}$$

$$w(\mathbf{k}_l) = \int d^2x\ \frac{e^{-i\mathbf{k}_l\cdot(\mathbf{x}-\mathbf{x}_l)}}{\sqrt{V}}w(\mathbf{x}-\mathbf{x}_l). \tag{3.87}$$

Thus, the momentum distribution takes the form,

$$n(\mathbf{k}) = \sum_{l,l'} w^*(\mathbf{k}_l)w(\mathbf{k}_{l'})e^{i\mathbf{k}\cdot(\mathbf{x}_l-\mathbf{x}_{l'})}\langle\psi|\hat{a}_l^\dagger\hat{a}_{l'}|\psi\rangle. \tag{3.88}$$

This distribution is written in the momentum coordinates, $\mathbf{k}$, corresponding to the rotating frame coordinates, $\mathbf{x}$. Since the number density rotates in the lab frame coordinates, $\mathbf{x}_\mathrm{L}$, the momentum distribution also rotates in the lab frame momentum coordinates, $\mathbf{k}_\mathrm{L}$. However, far-field pictures of the gas will be snapshots of the momentum distribution at the moment the trap and lattice are turned off, provided the switch-off time is fast enough. Thus, the momentum distributions presented here are accurate representations of what will be measured in time-of-flight measurements, although they may be rotated relative to each other.

Since quasi-angular momentum is a reflection of the symmetry of the system, considering single-particle states should be sufficient to capture the basics of how this quantum number affects the momentum distribution. We therefore concentrate on single-particle states only. In this case, $n(\mathbf{k})$ is merely the square of the Fourier transform of the wave function.

In order to develop an understanding of the momentum distribution, we first neglect the Wannier functions, which neglects the envelope of the momentum distribution. In this case, $n(\mathbf{k})$ is the Fourier transform of a sum of weighted delta functions. On a four site-lattice, the wave function is of the form

$$\psi(\mathbf{x}) \propto \sum_{j=1}^{4} e^{i2\pi mj/4}\delta(\mathbf{x}-\mathbf{x}_j), \tag{3.89}$$

where $\mathbf{x}_j$ are the four corners of a square centered at $\mathbf{x}=0$. In figure 3.10 are plotted the momentum distributions for $m = 0$, 1, 2, and 3. The $m = 0$ state is peaked at $\mathbf{k} = 2\pi n/d$, with $n$ an integer and $d$ the lattice spacing, whereas the other states vanish at these points. The spacing between peaks for both $m = 0$ and $m = 2$ is $\Delta k = 2\pi/d$, whereas for $m = 1, 3$ this spacing is $\Delta k = 2\pi/\sqrt{2}d$. Since the lattice spacing is known, there are clear measurable distinctions between different generic quasi-angular momentum states. Note that $m = 1$ and $m = 3$ are identical as they represent similar states with counter-propagating current patterns.

Including the Wannier functions contributes to the momentum distribution an overall envelope of approximate width $\sqrt{V_0/E_R}/4$, where $V_0$ is the depth of the lattice. The modification $\mathbf{k} \to \mathbf{k}_l$, equation (3.85), moves the peak of this envelope away from $\mathbf{k} = 0$ as rotation is increased, though the center of the envelope is always located at $\mathbf{k} = 0$. This is consistent with higher momenta being accessed for higher rotation rates.

At this point, it is important to note that locating $\mathbf{k} = 0$ in the distribution is necessary for distinguishing the $m = 0$ and $m = 2$ states. This can be done easily due to the overall envelope in momentum space that is centered at $\mathbf{k} = 0$.

There are two additional considerations that come into play for larger lattices, both system-size effects. An overall envelope in position space determines the width of the peaks in momentum space. This envelope determines the size of the system, and if the width is roughly $L$, then the width of the peaks in momentum space scales as $1/L$. If the lattice spacing is increased by a factor of $n$, then the peak-spacing in

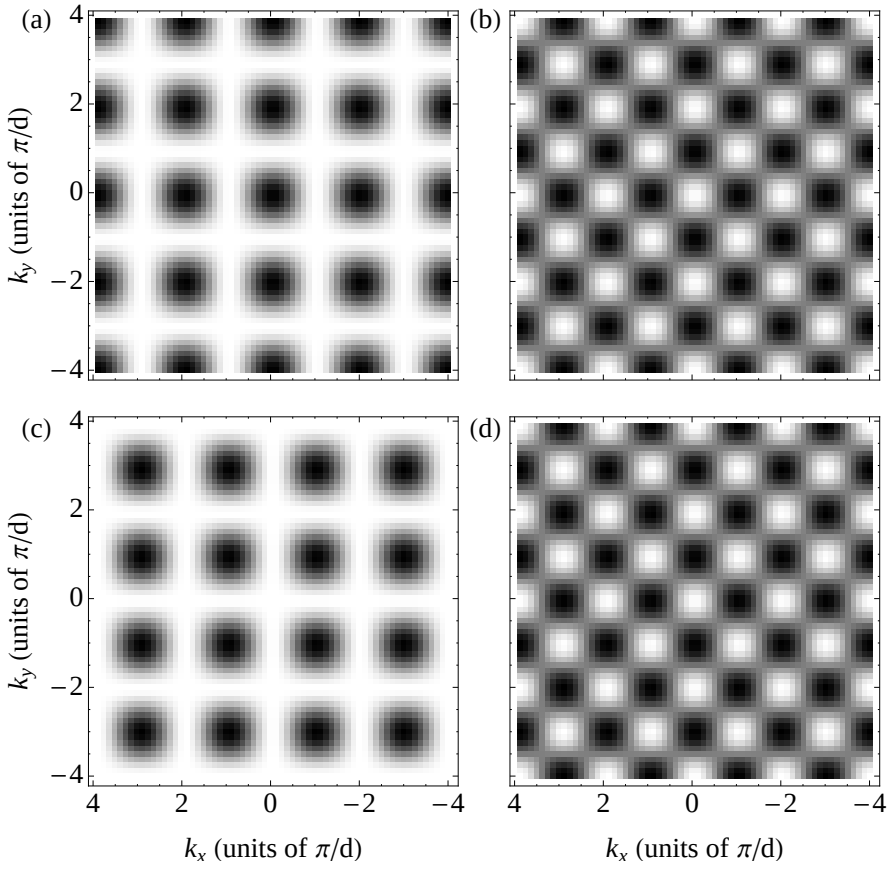


Figure 3.10: Fourier transform of single-particle quasi-angular momentum states on four sites, neglecting an overall envelope caused by the width of the Wannier functions. The quasi-angular momentum is (a) $m = 0$, (b) $m = 1, 3$, (c) $m = 2$, and (d) $m = 3$, and the momentum distributions are plotted over a range $4\pi/d \leq k_x, k_y \leq 4\pi/d$; the first Brillouin zone is given by $\pi/d \leq k_x, k_y \leq \pi/d$.

momentum space is decreased be a factor of $1/n$. The general peak structure is not modified by these considerations. We can conclude that the distinctions between quasi-angular momentum states are sustained for more physical systems, which we turn to now.

The ground state momentum distribution for a one-hundred-site lattice in the presence of a harmonic trap of frequency $\Omega_T = 0.15E_R/\hbar$ is computed via imaginary time propagation. The trap ensures that the number density falls off to zero outside the central 36 sites, eliminating the edge effects of the hard-wall boundary at the edges of the lattice.

The results are summarized in figure 3.11, where we have plotted the momentum distributions for the $m = 0$, 1, 2, and 3 states at rotation speeds of 0, $0.1E_R/\hbar$, and $0.145E_R\hbar$, increasing to the right. We can again make the observation that the $m = 0$ state is the only one that is non-zero at exactly the reciprocal lattice vectors, i.e. $\mathbf{k} = \frac{2\pi n}{d}\hat{\mathbf{k}}_x + \frac{2\pi m}{d}\hat{\mathbf{k}}_y$. The peak-spacing is smaller for the $m = 1$ state than for the $m = 2$ state, distinguishing them from each other. However, the exact peak-spacing is unclear due to complex interference effects between sites at different radii.

These differences are washed out at higher rotation speeds. The $m = 1$, $m = 2$, and $m = 3$ states have very similar structures for large rotation. The peaks overlap so that it is difficult to resolve them; the momentum distributions all appear to be rings centered at reciprocal lattice vectors. They are distinguishable via the radius of the ring, as the radius is smallest for $m = 1$ and largest for $m = 3$, but as this is in order of increasing energy, the larger radius may just be an artifact of the larger width in the number density envelope at higher energies. Indeed, figures 3.11(a), 3.11(b), and 3.11(c) are consistent with this conclusion, as the momentum peaks are narrowing due to the number density spreading out in real space. These results are consistent with those calculated via direct diagonalization of the Hubbard models previously discussed.

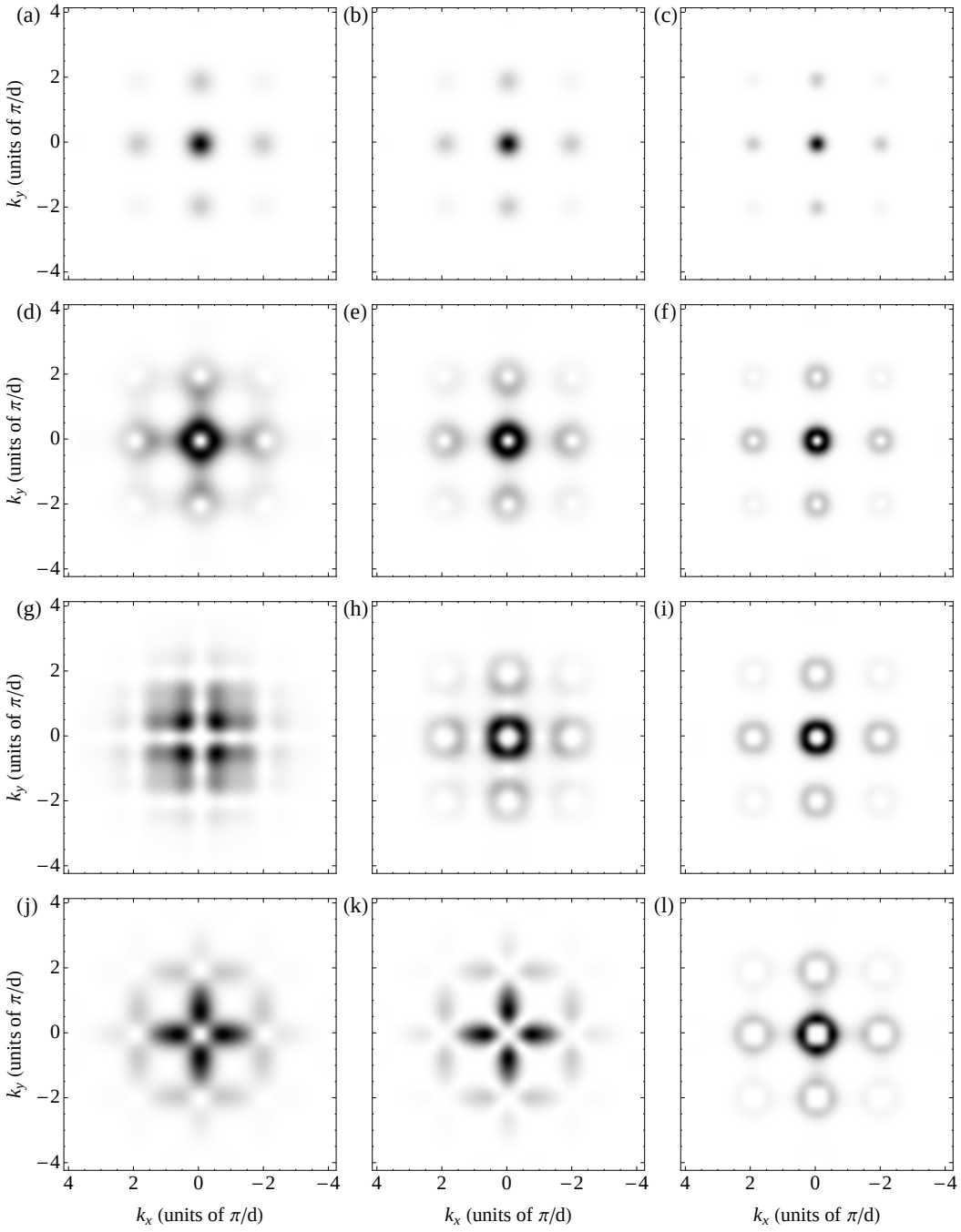


Figure 3.11: Momentum distributions computed via imaginary time propagation for one particle in a 100-site lattice in the presence of a trap of frequency $\Omega_T = 0.15E_R/\hbar$. Plotted are $m = 0$ ((a), (b), and (c)), $m = 1$ ((d), (e), and (f)), $m = 2$ ((g), (h), and (i)), and $m = 3$ ((j), (k), and (l)) states for rotation speeds of $\Omega = 0$ ((a), (d), (g), and (j)), $\Omega = 0.1E_R/\hbar$ ((b), (e), (h), and (k)), and $\Omega = 0.145E_R/\hbar$ ((c), (f), (i), and (l)). At zero rotation, the distinctions between different quasi-angular momenta are sustained. As rotation is increased, it becomes harder to distinguish the $m = 1$ and $m = 2$ states. Due to the centrifugal term, higher rotation increases the width of the envelope of the number density, decreasing the width of the peaks in momentum space.

## 3.6 Conclusion

By analogy with quasi-momentum in translationally invariant periodic systems, the notion of quasi-angular momentum has been introduced to label the eigenstates of a Hamiltonian that has a discrete rotational symmetry. We have shown that quasi-angular momentum is useful in analyzing the ground-state properties of quantum gases of bosons or fermions in rotating optical lattices. In particular, monitoring the quasi-angular momentum of the ground state as a function of rotation allows us to identify transitions between different circulation values.

We have also presented a possible avenue by which the quasi-angular momentum of a state can be experimentally determined. We identify characteristics in the momentum distribution distinguishing between different quasi-angular momentum states at low rotation speeds, such as the existence of a peak at reciprocal lattice vectors for an $m = 0$ state only, the peak-spacing, and the overall structure of the momentum distribution.

There are still open questions as to how the momentum distributions will change when the lattice size or number of particles is increased. The effects of statistics will be of fundamental importance for many-particle systems; there is a question of how well the peaks can be resolved for larger lattices, since peak-spacing decreases with increasing lattice size; and interference effects between adjacent sites and between rings complicates our treatment of the exact spacing between peaks in the momentum distribution. However, there will always be signatures of the quasi-angular momentum in the momentum distribution, as it is connected with the phase information of the ground state, which in turn influences the momenta of the system. In addition, a zero quasi-angular momentum state can be distinguished from a non-zero one, which allows the experimenter to verify that vorticity has entered the system.

The approximations used to describe strongly-interacting bosons can be used to

analyze many different ground-state features of the system. In particular, we can use these results to generate Mott-insulator to superfluid phase diagrams for both flat and superlattices, indicating changes in dynamical behavior.

# Chapter 4

## Mott-Insulator to Superfluid Phase Diagrams

One of the first successes in the AMO physics subfield of simulation of many-body models using ultracold, neutral atoms trapped in optical lattices was the verification of the superfluid (SF) to Mott-insulator (MI) transition in the Bose-Hubbard model [39, 47]. The experiment set off an explosion of research investigating the phase diagram of various models related to the Bose-Hubbard Hamiltonian, including the introduction of superlattices and the effects of the presence of both fermionic and bosonic particles. Unanswered questions from condensed matter systems, including the nature of quantum criticality and the behavior of certain dynamical structure factors of one-dimensional systems, might be resolved in ultracold, atomic systems. A complete understanding of the phase transitions that occur in the simplest of many-body systems, such as those modeled by the Bose-Hubbard Hamiltonian, is therefore essential.

As a final application of the formalism developed and discussed in the previous chapter, we compute the phase diagrams for strongly-interacting bosons in a two-state (i.e. fermionized) approximation in the presence of a superlattice. This captures the exact nature of the diagram for small $J/U$. The behavior of the Mott-insulator lobes as a function of the energy difference between adjacent wells was useful in an early version of atomtronics [118]. We compare the phase diagram in this approximation to that generated via the mean field calculation in section 2.1.2.

## 4.1 MI-SF Phase Diagram for Strongly-Interacting Bosons

In this section, by diagonalizing a one-dimensional, fermionized Bose-Hubbard Hamiltonian, we generate the phase for strongly-interacting bosons trapped in an optical lattice. The phase boundaries in the $(\mu/U, J/U)$-plane are the contours of zero energy in the single-particle spectrum.

We previously derived the fermionized Hamiltonian for strongly-interacting bosons in a rotating ring lattice, equation 3.60. Taking $\omega = 0$ and eliminating the periodic boundary conditions, we have the Hamiltonian for bosons on a one-dimensional lattice,

$$\hat{H}^{(l)} = UN\frac{l(l-1)}{2} - \mu Nl + (Ul - \mu)\sum_{j=1}^{N}\hat{c}_j^\dagger\hat{c}_j + \sum_{j=1}^{N}\epsilon(\omega)\hat{c}_j^\dagger\hat{c}_j - J(l+1)\sum_{j=1}^{N-1}\hat{c}_j^\dagger\hat{c}_{j+1} + \text{H.c.} \tag{4.1}$$

where $U$ is the on-site, two-particle interaction strength, $J$ is the tunneling energy, and $l$ is the filling fraction, i.e. the number of particles per lattice site. In this approximation, the fermionic operator $\hat{c}_j^\dagger$ adds one particle to site $j$, raising the number of particles from $l$ to $l+1$. We have introduced the chemical potential, $\mu$, so that we can work in the grand-canonical ensemble. We perform the canonical transformation,

$$\hat{c}_k = \sqrt{\frac{2}{N+1}}\sum_{m=1}^{N}\sin\left(\frac{\pi mk}{N+1}\right)\hat{d}_m, \tag{4.2}$$

which diagonalizes the Hamiltonian, yielding

$$\hat{H}^{(l)} = \sum_{m=1}^{N}\left(Ul - \mu - 2(l+1)J\cos\left(\frac{\pi m}{N+1}\right)\right)\hat{d}_m^\dagger\hat{d}_m - \mu Nl + UN\frac{l(l-1)}{2}. \tag{4.3}$$

Fixing $l$, we can see that the ground state is given by populating those eigenstates of the $\hat{d}_m^\dagger\hat{d}_m$ operators for which the energy $Ul-\mu-2(l+1)J\cos(\pi m/(N+1))$ is negative. Therefore, every time there is an $m$ for which this energy is zero, the particle number changes by one. This argument implies that the boundaries between phases of different particle number are truly given by

$$\frac{\mu}{U} = l - 2(l+1)\frac{J}{U}\cos\left(\frac{\pi m}{N+1}\right). \tag{4.4}$$

The phase diagram with these phase boundaries is plotted in figure 4.1(a) for the case of an eight-site lattice. The overlaps of the phase boundaries completes the story. Each time there is an intersection between boundaries, a different particle-number becomes the global ground state of the system. As the number of sites goes to infinity, the number of phase boundaries goes to infinity, and the area outside the empty triangles in the figure becomes a continuum of particle-number states. This implies that outside the empty triangular regions, the ground state is a state of uncertain site-number, or a superfluid. Within the empty triangles, the ground state is a number state. We can then interpret these empty spaces as Mott lobes in the Mott-insulator to superfluid phase diagram, with the triangular regions the Mott insulator states and outside these regions superfluid.

This approximate phase diagram has been derived in a slightly modified form in [24] using a semiclassical approach.

### 4.1.1 Comparison between two-state and mean-field approximations

In figure 4.2, we plot the MI-to-SF phase diagram as computed in the two-state approximation and as computed via the mean-field calculation from section 2.1.2. The two methods agree in the strong-interaction regime, i.e. for small $J/U$, but significantly differ from each other for larger values of the tunneling parameter. The most visible difference is the behavior of the phase boundaries near the tip of the Mott lobe. In the two-state approximation, this tip is pointed, whereas in the mean-field approximation, the tip is rounded.

The true character of the phase diagram may lie somewhere in between. In reference [39], it is noted that the phase transition that occurs at the tip of the Mott lobe is of a markedly different character than the one that occurs away from this tip. This is because the transition at the tip occurs at a fixed density—or rather, at a fixed integer filling fraction—whereas the transition that occurs at the phase boundaries away

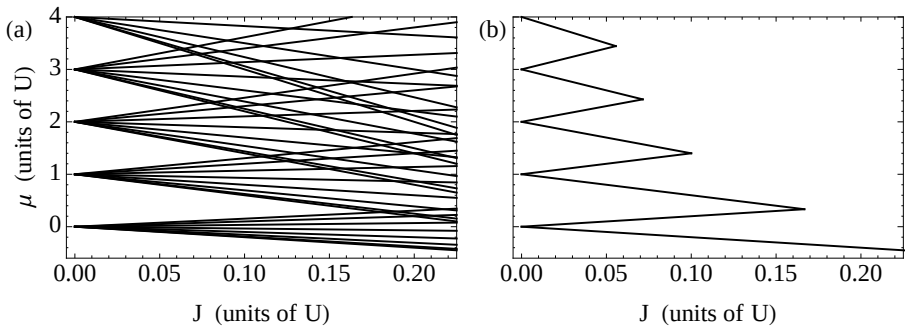


Figure 4.1: Bose-Hubbard phase diagram for strongly-interacting bosons in a one-dimensional lattice. In the large-$N$ limit, for large enough $J/U$, the strongly-interacting approximation breaks down, and the tips of the Mott lobes become rounded. (a) Phase boundaries for an eight-site lattice. Each white region is a region where the ground-state is a state of exact particle-number. (b) As the number of sites increases, the region outside the triangular spaces becomes a continuum of different particle-number ground states. This region is then considered to be superfluid.

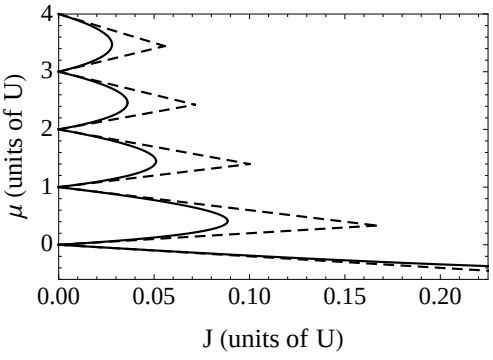


Figure 4.2: Comparison between the MI to SF phase diagrams computed using a two-state approximation and a mean-field approximation.

from the lobe tip involves adding or subtracting a particle from the system.

## 4.2 Superlattices

A direct generalization of the procedure above is to introduce an extra periodic potential with periodicity larger than the original lattice. The simplest way to implement this is to add an energy to every $M$'th site, leaving the rest of the lattice flat. The ring and one-dimensional lattices should be identical in the large-$N$ limit, so for ease of future calculation, we re-include periodic boundary conditions in this section.

This extra periodic potential takes the form,

$$\hat{V} = \sum_{j=1}^{N/M} \epsilon \hat{c}^{\dagger}_{Mj} \hat{c}_{Mj}. \tag{4.5}$$

In terms of the operators that diagonalize the Hamiltonian for the flat lattice, this is

$$\begin{aligned}\hat{V} &= \sum_{j=1}^{N/M} \epsilon \frac{1}{\sqrt{N}} \sum_{n=0}^{N-1} e^{-i2\pi nMj/N} \hat{d}^{\dagger}_n \frac{1}{\sqrt{N}} \sum_{m=0}^{N-1} e^{i2\pi mMj/N} \hat{d}_m \\ &= \frac{\epsilon}{M} \sum_{m,n=1}^{N} \hat{d}^{\dagger}_m \hat{d}_n \delta_{\mathrm{mod}_{N/M}(m-n),0}. \end{aligned} \tag{4.6}$$

Taking

$$m = \frac{N}{M} q_1 + m_1, \tag{4.7}$$

$$n = \frac{N}{M} q_2 + m_2, \tag{4.8}$$

$$m_j = 0, \ldots, \frac{N}{M} - 1, \tag{4.9}$$

$$q_j = 0, \ldots, M-1, \tag{4.10}$$

We can re-write the full transformed Hamiltonian as

$$\begin{aligned}\hat{H}^{(l)} = &-\mu N l + UN \frac{l(l-1)}{2} \\ &+ \sum_{m=0}^{N/M-1} \sum_{q=0}^{M-1} \left( Ul - \mu - 2(l+1)J \cos\left( \frac{2\pi}{N} \left( \frac{N}{M} q + m \right) \right) \right) \hat{d}^{\dagger}_{(N/M)q+m} \hat{d}_{(N/M)q+m} \\ &+ \frac{\epsilon}{M} \sum_{m=0}^{N/M-1} \sum_{q_1,q_2=0}^{M-1} \hat{d}^{\dagger}_{(N/M)q_1+m} \hat{d}_{(N/M)q_2+m}. \end{aligned} \tag{4.11}$$

This Hamiltonian can be diagonalized separately at every $m$. In order to do this, we define the column vector,

$$\mathbf{d}^{(m)} = \left(\hat{d}_m, \hat{d}_{N/M+m}, \hat{d}_{2N/M+m}, \ldots, \hat{d}_{(M-2)N/M+m}, \hat{d}_{(M-1)N/M+m}\right). \tag{4.12}$$

The Hamiltonian can then be rewritten as

$$\hat{H}^{(l)} = -\mu N l + UN\frac{l(l-1)}{2} + \sum_{m=0}^{N/M-1} \mathbf{d}^{(m)\dagger}\bar{\mathbf{h}}^{(l,m)}\mathbf{d}^{(m)}, \tag{4.13}$$

where $\bar{\mathbf{h}}^{(l,m)}$ is an $M \times M$ matrix with elements,

$$h^{(l,m)}_{q'q} = \delta_{q',q}\left(Ul - \mu - 2(l+1)J\cos\left(\frac{2\pi}{M}q + \frac{2\pi}{N}m\right)\right) + \frac{\epsilon}{M}. \tag{4.14}$$

Diagonalizing $\bar{\mathbf{h}}^{(l,m)}$ yields eigenvectors, $\psi^{(l,m;n)}$, with corresponding eigenvalues $\lambda^{(l,m)}_n$. The canonical transformation,

$$\hat{f}^{(l,m)}_n = \sum_{q=1}^{M} \psi^{(l,m;n)*}_j \hat{d}_{(N/m)q+m}, \tag{4.15}$$

results in the manifestly diagonal Hamiltonian,

$$\hat{H}^{(l)} = -\mu N l + UN\frac{l(l-1)}{2} + \sum_{m=0}^{N/M-1}\sum_{n=1}^{M} \lambda^{(l,m)}_n \hat{f}^{(l,m)\dagger}_n \hat{f}^{(l,m)}_n. \tag{4.16}$$

The eigenvalues, $\lambda^{(l,m)}_n$, can be used to determine the phase boundaries in a modified MI-SF phase diagram.

As an example, we consider the case of $M = 3$. We first take the large-$N$ limit where the matrix elements of $\bar{\mathbf{h}}^{(l,m)}$ take the form,

$$h^{(l,m)}_{q'q} = \delta_{q',q}\left(Ul - \mu - 2(l+1)J\cos\left(\frac{2\pi}{3}q\right)\right) + \frac{\epsilon}{3}. \tag{4.17}$$

The eigenvalues of this matrix are

$$\lambda^{(l)}_{\pm} = \frac{\epsilon}{2} + lU - \mu - \frac{1}{2}(l+1)J \pm \frac{1}{2}\sqrt{\epsilon^2 + 2(l+1)J\epsilon + 9(l+1)^2J^2}, \tag{4.18}$$

$$\lambda^{(l)}_0 = lU - \mu + (l+1)J. \tag{4.19}$$

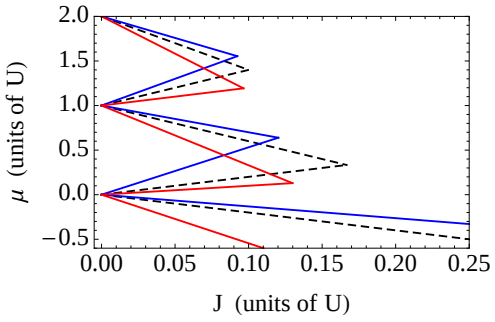


Figure 4.3: MI-SF phase diagram for an infinite one-dimensional lattice. The dashed black curve is the phase diagram for the flat lattice. The red curve is the phase diagram for a lattice with every third site shifted down in energy by $\epsilon = -5J$. The blue curve is the phase diagram for a lattice with every third site shifted up in energy by $\epsilon = 5J$.

We consider the special case where the on-site energy shift is proportional to the hopping rate, $\epsilon = \alpha J$, in which case these reduce to

$$\lambda_{\pm}^{(l)} = lU - \mu + \frac{J}{2}\left(\alpha - (l+1) \pm \sqrt{\alpha + 2(l+1)\alpha + 9(l+1)^2}\right). \tag{4.20}$$

An argument similar to that in the previous section yields the boundaries between the MI and SF phases. As we can see in figure 4.3, the Mott lobes are sheared upwards when every third lattice site is shifted up in energy relative to the rest of the lattice, whereas the Mott lobes are sheared downwards when every third lattice site is shifted down.

## 4.3 Conclusion

We have generated the Mott-insulator to superfluid phase diagram for strongly-interacting bosons trapped in a one-dimensional lattice. This computation is exact for small enough $J/U$, since in this regime, the bosons are well-described via the Jordan-Wigner transformation that maps strongly-interacting bosons onto non-interacting fermions. One significant difference between this computation and the phase diagram as computed via mean-field theory is the character of the tip of the Mott lobe, where the diagram in

the two-state approximation has pointed tips.

The hard-core boson approximation breaks down for large enough $J/U$, which means that it does not correctly capture the behavior of the phase boundaries near the tip of the Mott lobe. On the other hand, the mean-field computation assumes that fluctuations in the order parameter $\langle c_i \rangle$ are small near the phase transition, which is also a bad approximation. The truth probably lies somewhere in between these two extremes.

# Chapter 5

## Non-Destructive Cavity QED Probe of Atomic Dynamics in an Optical Lattice

**The bulk of this chapter was published in the Physical Review A as Phys. Rev. A 80, 043803 (2009) [102].**

In this chapter, we propose a method for optically probing atomic gases in optical lattices subject to an external potential. The method is *in situ* and non-destructively measures properties of the atomic motion via weak-coupling to the existing lattice fields. The technique satisfies three main goals. The probe is weak so that the atoms can be continuously monitored without affecting their dynamics; the existing lattice fields are employed as the probe, so that no additional, external interrogation fields are necessary; and the signal-to-noise ratio (SNR) is large enough for experimental detection. In a ring-cavity, two counter-propagating running-wave modes interact with a gas of ultracold atoms and simultaneously set up both a conservative, external lattice potential for the atoms and a weak, quantum optical probe of the atomic center-of-mass dynamics. The probe field leaks out of the cavity and is detected with a balanced heterodyne scheme at the cavity output.

This method is in a sense dual to strong measurement schemes such as time-of-flight absorption imaging and Bragg spectroscopy. In these schemes, laser light is either absorbed by or scattered off of the atomic cloud. This allows for high resolution images and a strong signal using only a single measurement, but the atomic sample is destroyed in the process. In contrast, in our measurement scheme, the probe field is very

weak so that a continuous measurement is made without affecting the atomic dynamics. Integration of the signal in time and across the atomic cloud yields measurements of dynamical properties of the atoms with a measurable SNR in a single experimental run at the price of losing information about individual atoms and real-time dynamics.

The procedure is similar in spirit to recent proposals for optical detection of many-body atomic states [27, 86, 128] and occupies a place in AMO physics shared by proposals for state preparation in cavity QED systems [85, 87, 93]. In addition, experiments have already been carried out for nondestructive probing of various systems [26, 58, 124, 131].

We here provide a test of the technique for the conceptually simple motion of non-interacting atoms in an optical lattice driven by a constant force, which leads to Bloch oscillations [8]. This choice is motivated by the fact that Bloch oscillations can be viewed as a probe for investigating quantum gases in optical lattices. These oscillations may be used in the measurement of fundamental constants [28], to provide levels of precision up to $\delta g/g \approx 10^{-7}$ in the measurement of the acceleration of gravity [3, 23, 36, 62, 108], and to measure Casimir forces on small length scales [132]. When interactions are significant, damping of Bloch oscillations provides information on correlation-induced relaxation processes [18, 34, 42, 82, 94]. Finally, this investigation is a starting point for other measurement schemes, such as periodically driven lattices acting as a spectroscopic probe of atomic motion [62].

## 5.1 Model and Detection Scheme

We briefly outline the physical basis of the model and approximations used. This includes a discussion of obstacles in the way of satisfying the goals outlined above, avoiding these problems, and the conditions required for the method to work.

To set up a conservative lattice potential, many photons must be present in the cavity field so that fluctuations can be neglected, and this necessitates strong pumping

from the in-coupled lasers. On the other hand, the probe field amplitude must be small enough so that it does not affect the atomic dynamics, requiring weak pumping. In addition, the probe and lattice fields are coupled to each other through the scattering of photons off of the atoms. This acts as an extra source for probe dynamics. The probe field is then not a direct measure of atomic dynamics and can act back on the atoms, altering the properties we are attempting to measure.

We can circumvent these problems by first choosing the relative phase on the in-coupled lasers so that only one of two standing-wave modes in the cavity is pumped. Strong pumping and the properties of a bad cavity—where the fields are at all times in steady state—ensure that the pumped mode acts as a lattice potential. The other standing-wave mode is not pumped. Any field leaking out of the cavity from this mode arises solely because of events occurring in the cavity, and it can therefore act as a probe for system dynamics.

Ensuring that the non-pumped mode acts as a probe of atomic dynamics requires that two conditions be met. The probe must have as its source *only* the motion of the atoms. This means that any probe dynamics due to the effective coupling to the lattice field must be small compared to that induced by the motion of the atoms. The back-action of this mode on the atoms must also be negligible. Any atomic motion induced by coupling to the probe field must be small compared to the motion induced by both lattice and external potentials.

Two conditions are also required for the pumped field to act as a conservative lattice potential. The back-action of the atoms on the lattice field must be negligible, meaning that deviations from the mean field amplitude caused by coupling to the atoms is small compared to the mean field amplitude itself. In addition, any atomic motion induced by fluctuations away from the mean lattice field must be small compared to that induced by the external potential, since this is the interesting dynamics.

The scheme is realized in the setup illustrated in figure 5.1. We consider $N_a$

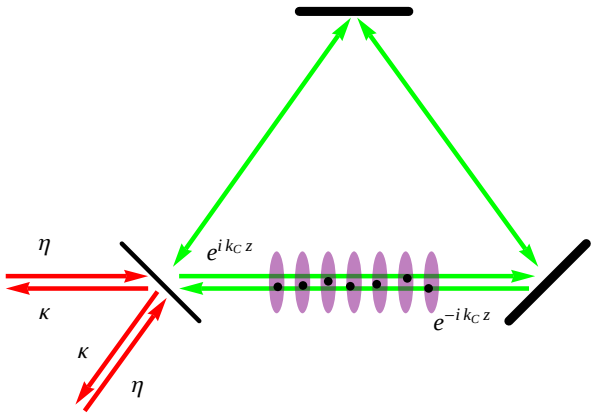


Figure 5.1: Schematic of the coupled atom-cavity system. In-coupled lasers set up two counter-propagating fields within the cavity. The atoms interact with the cavity fields via the optical dipole potential. Photons from the cavity beams exit the cavity through the mirrors at a rate $\kappa$.

ground-state atoms interacting with two counter-propagating running-wave cavity modes in a ring resonator setup. The two modes of the cavity have frequency $\omega_{\rm C}$ and wave vectors $\pm k_{\rm C}\hat{z}$. The two cavity modes are coherently pumped at a detuning $\Delta_p = \omega_L - \omega_{\rm C}$ where $\omega_L$ is the frequency of the pumping lasers. Photon decay through the cavity mirrors is treated within the Born-Markov approximation. We treat the atom-cavity-field interaction in rotating wave and dipole approximations. The cavity-modes are far-detuned from atomic transitions. This same setup has been used in a cooling scheme for atoms [49].

### 5.1.1 Model

The effective Hamiltonian for the coupled atom-cavity system is given by

$$\hat{H} = \int dz\ \hat{\Psi}^\dagger(z)\left(-\frac{\hbar^2}{2m}\frac{d^2}{dz^2} + V_{\rm ext}(z)\right)\hat{\Psi}(z) + \sum_{k=\pm k_{\rm C}}\left(\hbar\eta\hat{a}_k + \hbar\eta\hat{a}_k^\dagger - \hbar\Delta_p\hat{a}_k^\dagger\hat{a}_k\right)$$
$$+ \int dz\ \hat{\Psi}^\dagger(z)\ \hbar g_0\left(\hat{a}_{k_{\rm C}}^\dagger e^{-ik_{\rm C}z} + \hat{a}_{-k_{\rm C}}^\dagger e^{ik_{\rm C}z}\right)\left(\hat{a}_{k_{\rm C}}e^{ik_{\rm C}z} + \hat{a}_{-k_{\rm C}}e^{-ik_{\rm C}z}\right)\hat{\Psi}(z). \quad (5.1)$$

Here, $\hat{\Psi}$ is the atomic field operator, and $\hat{a}_k$ is the annihilation operator for the cavity mode, $k$. The parameter, $m$, is the the mass of the atom, $g_0$ is the two-photon atom-

cavity coupling, and $\eta$ is the strength of the cavity field pumping, taken to be real. Due to the far detuning of the cavity fields from the atomic transition, excited states of the atom have been adiabatically eliminated, and the atoms couple to the field intensity. The three terms in equation (5.1) are respectively the atomic kinetic energy and external potential, the bare cavity mode Hamiltonian, and the atom-cavity interaction. Cavity losses through the cavity mirrors are treated via a master equation with Liouvillian,

$$\hat{\mathcal{L}}\hat{\rho} = -\frac{\hbar\kappa}{2}\sum_{k=\pm k_{\mathrm{C}}}\left(\hat{a}_k^\dagger\hat{a}_k\hat{\rho} + \hat{\rho}\hat{a}_k^\dagger\hat{a}_k - 2\hat{a}_k\hat{\rho}\hat{a}_k^\dagger\right), \tag{5.2}$$

where $\hat{\rho}$ is the reduced density matrix for the atom-cavity system, and $\kappa$ is the cavity linewidth.

We perform a canonical transformation of the cavity mode operators to symmetric and anti-symmetric modes,

$$\hat{b}_\pm = \frac{\hat{a}_{k_{\mathrm{C}}} \pm \hat{a}_{-k_{\mathrm{C}}}}{\sqrt{2}}. \tag{5.3}$$

The bare cavity Hamiltonian in terms of these operators is given by

$$\hat{H}_{\mathrm{C}} = \sqrt{2}\hbar\eta\left(\hat{b}_+ + \hat{b}_+^\dagger\right) - \hbar\Delta_p\left(\hat{b}_+^\dagger\hat{b}_+ + \hat{b}_-^\dagger\hat{b}_-\right). \tag{5.4}$$

The symmetric mode, $\hat{b}_+$, is pumped by the in-coupled lasers whereas the anti-symmetric mode, $\hat{b}_-$, is not. The $\hat{b}_+$ mode has a mode function proportional to $\cos(k_{\mathrm{C}}z)$ and sets up the lattice potential, as follows.

The equation of motion for the symmetric field amplitude is

$$i\frac{d\langle\hat{b}_+\rangle}{dt} = \left(-i\frac{\kappa}{2} - \Delta_p\right)\langle\hat{b}_+\rangle + \sqrt{2}\eta + 2g_0\langle\hat{b}_+\hat{C}\rangle + ig_0\langle\hat{b}_-\hat{S}_2\rangle, \tag{5.5}$$

where

$$\hat{C} = \int dz\cos^2(k_{\mathrm{C}}z)\,\hat{\Psi}^\dagger(z)\hat{\Psi}(z), \tag{5.6}$$

$$\hat{S}_2 = \int dz\sin(2k_{\mathrm{C}}z)\,\hat{\Psi}^\dagger(z)\hat{\Psi}(z). \tag{5.7}$$

We perform another transformation to a fluctuation operator, $\hat{d}_+ = \hat{b}_+ - \beta$, leaving the anti-symmetric mode unchanged, $\hat{d}_- = \hat{b}_-$. The mean steady-state amplitude, $\beta$, is given by

$$\beta = \langle \hat{b}_+ \rangle = \frac{\sqrt{2}\eta}{\Delta_p - 2g_0\langle \hat{C} \rangle_0 + i\kappa/2}, \tag{5.8}$$

where $\langle \hat{C} \rangle_0$ is $\langle \hat{C} \rangle$ evaluated at $t = 0$.

The equations of motion for both $\hat{d}_+$ and $\hat{d}_-$ are given by

$$i\frac{d\langle \hat{d}_- \rangle}{dt} = \left(-\Delta_p - i\frac{\kappa}{2}\right)\langle \hat{d}_- \rangle + 2g_0\langle \hat{d}_- \hat{S} \rangle - ig_0\langle \hat{d}_+ \hat{S}_2 \rangle - ig_0\beta\langle \hat{S}_2 \rangle, \tag{5.9}$$

and

$$i\frac{d\langle \hat{d}_+ \rangle}{dt} = \left(-\Delta_p - i\frac{\kappa}{2}\right)\langle \hat{d}_+ \rangle + 2g_0\langle \hat{d}_+ \hat{C} \rangle + ig_0\langle \hat{d}_- \hat{S}_2 \rangle + 2g_0\beta\left(\langle \hat{C} \rangle - \langle \hat{C} \rangle_0\right), \tag{5.10}$$

where

$$\hat{S} = \int dz \sin^2(k_C z)\hat{\Psi}^\dagger(z)\hat{\Psi}(z). \tag{5.11}$$

Finally, the equation of motion for the atomic field operator is given by

$$\begin{aligned} i\hbar\frac{d\hat{\Psi}(z)}{dt} = &\left(-\frac{\hbar^2}{2m}\frac{d^2}{dz^2} + V_{\text{lat}}(z) + V_{\text{ext}}(z)\right)\hat{\Psi}(z) \\ &+ i\hbar g_0\left(\beta^*\hat{d}_- - \beta\hat{d}_-^\dagger\right)\sin(2k_C z)\hat{\Psi}(z) + 2\hbar g_0\left(\beta\hat{d}_+^\dagger + \beta^*\hat{d}_+\right)\cos^2(k_C z)\,\hat{\Psi}(z) \\ &+ 2\hbar g_0\,\hat{d}_-^\dagger\hat{d}_-\sin^2(k_C z)\hat{\Psi}(z) + 2\hbar g_0\,\hat{d}_+^\dagger\hat{d}_+\cos^2(k_C z)\,\hat{\Psi}(z) \\ &+ i\hbar g_0\left(\hat{d}_+^\dagger\hat{d}_- - \hat{d}_-^\dagger\hat{d}_+\right)\sin(2k_C z)\hat{\Psi}(z), \end{aligned} \tag{5.12}$$

where $V_{\text{lat}}(z) = V_0\cos^2(k_C z)$ is a conservative lattice potential of depth, $V_0 = 2\hbar g_0|\beta|^2$.

This depth is proportional to the number of photons $|\beta|^2$ in the symmetric mode. Since the coupling strength $\hbar g_0$ will be relatively small due to the large detuning between cavity fields and atomic resonances, the number of photons in the symmetric mode will have to be relatively large. Using the parameters below, we arrive at a coupling strength of about $10^{-4}E_R$, and assuming that we want lattice depths of at least a couple $E_R$, $|\beta|^2$ must be on the order of $10^4$–$10^5$. In addition, in order to be able to neglect field

fluctuations relative to the mean field, we must have that $|\beta| \ll |\beta|^2$. This is clearly satisfied for $|\beta|^2 \sim 10^4$–$10^5$.

At the beginning of this section, we outlined the conditions that need to be met in order for the cavity fields to act as both an external, lattice potential and a weak probe for the atoms. We can now put a more precise spin on these conditions.

First, in equations (5.9) and (5.10), the third term represents an effective coupling to the other mode mediated by the atoms, i.e. coherent scattering of photons off of the atoms between the modes. In order for $\hat{d}_-$ to act as an atomic probe, it needs to be decoupled from $\hat{d}_+$, so we need to be able to neglect this term. Examination of these equations indicates that the symmetric fluctuation field amplitude $\langle \hat{d}_+ \rangle$ must be much smaller than the steady-state symmetric mode amplitude $\beta$. Equivalently, the number of photons in the fluctuation field must be much smaller than the number of photons in the mean field. Using the scaling arguments described below, this condition translates into satisfying the relation

$$\frac{|g_0 \beta| N_a}{\kappa} \ll |\beta| \Longrightarrow \frac{|g_0| N_a}{\kappa} \ll 1. \tag{5.13}$$

Secondly, we can interpret the terms in lines two, three, and four of equation (5.12) as extra effective lattice potentials that arise due to the presence of photons in the anti-symmetric mode and in the symmetric fluctuation field. For instance, the first term in line three is a sine-squared lattice whose depth is $2g_0 \hat{d}_-^\dagger \hat{d}_-$. In this case, it is necessary that the number of photons in the anti-symmetric mode is much smaller than the number of photons in the symmetric mean field. Equation (5.13) again guarantees this condition.

### 5.1.2 Eliminating higher-order correlations

We make the preceding discussion more rigorous by computing the equations of motion for higher-order moments in order to generate scaling relations for correlations

such as $\langle \hat{d}_- \hat{S} \rangle$. By comparing these scales, we can eliminate many of the offending terms in equations (5.9), (5.10), and (5.12).

Upon examining equations (5.9) and (5.10), it is apparent that in order for $\hat{d}_-$ to act as a probe field, we must be able to neglect the higher-order atom-field correlations such as $\langle \hat{d}_+ \hat{S}_2 \rangle$. In addition, we must be able to neglect all but the first term in equation (5.12) in order that the lattice field act as an external, conservative potential.

To ensure that these conditions are satisfied, we examine the equations of motion for operators such as $\langle \hat{d}_+ \hat{C} \rangle$. Specifically, we compute the equation of motion for $\langle \hat{d}_\pm \hat{\Psi}^\dagger \hat{\Psi} \rangle$, given by

$$i\hbar \frac{d\langle \hat{d}_\pm \hat{\Psi}^\dagger \hat{\Psi} \rangle}{dt} = \langle \hat{d}_\pm [\hat{\Psi}^\dagger \hat{\Psi}, \hat{H}] \rangle + \langle [\hat{d}_\pm, \hat{H}] \hat{\Psi}^\dagger \hat{\Psi} \rangle - i \frac{\hbar \kappa}{2} \langle \hat{d}_\pm \hat{\Psi}^\dagger \hat{\Psi} \rangle. \tag{5.14}$$

The first term is small and can be neglected. For this reason, we drop it in the following discussion and return to it at the end. For $\hat{d}_-$ and $\hat{d}_+$ separately, the equations of motion become

$$\begin{aligned} i\hbar \frac{d\langle \hat{d}_- \hat{\Psi}^\dagger \hat{\Psi} \rangle}{dt} = & \left( -\hbar \Delta_p - i \frac{\hbar \kappa}{2} \right) \langle \hat{d}_- \hat{\Psi}^\dagger \hat{\Psi} \rangle - i\hbar g_0 \beta \langle \hat{S}_2 \hat{\Psi}^\dagger \hat{\Psi} \rangle \\ & + 2\hbar g_0 \langle \hat{d}_- \hat{S} \hat{\Psi}^\dagger \hat{\Psi} \rangle - i\hbar g_0 \langle \hat{d}_+ \hat{S}_2 \hat{\Psi}^\dagger \hat{\Psi} \rangle, \end{aligned} \tag{5.15}$$

and

$$\begin{aligned} i\hbar \frac{d\langle \hat{d}_+ \hat{\Psi}^\dagger \hat{\Psi} \rangle}{dt} = & \left( -\hbar \Delta_p - i \frac{\hbar \kappa}{2} \right) \langle \hat{d}_+ \hat{\Psi}^\dagger \hat{\Psi} \rangle + 2\hbar g_0 \langle \hat{d}_+ \hat{C} \hat{\Psi}^\dagger \hat{\Psi} \rangle \\ & + 2\hbar g_0 \beta \left( \langle \hat{C} \hat{\Psi}^\dagger \hat{\Psi} \rangle - \langle \hat{C} \rangle_0 \langle \hat{\Psi}^\dagger \hat{\Psi} \rangle \right) + i\hbar g_0 \langle \hat{d}_- \hat{S}_2 \hat{\Psi}^\dagger \hat{\Psi} \rangle. \end{aligned} \tag{5.16}$$

For the purpose of making a scaling argument, we drop all terms involving the product of a field operator with four atomic operators. Scaling relations for these quantities can be derived by adiabatically slaving them to the lower-order correlation functions. This is done by setting the time derivatives to zero, resulting in

$$\langle \hat{d}_+ \hat{\Psi}^\dagger \hat{\Psi} \rangle = -i \frac{4 g_0 \beta}{\kappa} (\langle \hat{C} \hat{\Psi}^\dagger \hat{\Psi} \rangle - \langle \hat{C} \rangle_0 \langle \hat{\Psi}^\dagger \hat{\Psi} \rangle), \tag{5.17}$$

$$\langle \hat{d}_- \hat{\Psi}^\dagger \hat{\Psi} \rangle = -\frac{2 g_0 \beta}{\kappa} \langle \hat{S}_2 \hat{\Psi}^\dagger \hat{\Psi} \rangle, \tag{5.18}$$

implying that

$$\langle \hat{d}_+ \hat{S}_2 \rangle = -i\frac{2g_0\beta}{\kappa}(\langle \hat{C}\hat{S}_2\rangle - \langle \hat{C}\rangle_0\langle \hat{S}_2\rangle), \tag{5.19}$$

$$\langle \hat{d}_- \hat{S}\rangle = -\frac{g_0\beta}{\kappa}\langle \hat{S}_2\hat{S}\rangle. \tag{5.20}$$

Plugging these back into the equations of motion for $\langle \hat{d}_\pm \rangle$, we have

$$i\frac{d\langle \hat{d}_-\rangle}{dt} = \left(-\Delta_p - i\frac{\kappa}{2}\right)\langle \hat{d}_-\rangle - 2\frac{g_0}{\kappa}g_0\beta(\langle \hat{C}\hat{S}_2\rangle - \langle \hat{C}\rangle_0\langle \hat{S}_2\rangle - \langle \hat{S}_2\hat{S}\rangle) - ig_0\beta\langle \hat{S}_2\rangle, \tag{5.21}$$

and

$$\begin{aligned} i\frac{d\langle \hat{d}_+\rangle}{dt} = &-i\frac{\kappa}{2}\langle \hat{d}_+\rangle - 4ig_0\frac{g_0\beta}{\kappa}(\langle \hat{C}^2\rangle - \langle \hat{C}\rangle_0\langle \hat{C}\rangle) \\ &- ig_0\frac{g_0\beta}{\kappa}\langle \hat{S}_2\hat{S}_2\rangle + 2g_0\beta(\langle \hat{C}\rangle - \langle \hat{C}\rangle_0). \end{aligned} \tag{5.22}$$

The terms with four atomic operators scale as

$$\begin{aligned} \left|\frac{g_0}{\kappa}g_0\beta\langle \hat{C}\rangle\langle \hat{S}_2\rangle\right| &\sim \frac{|g_0N_a|}{\kappa}|g_0\beta\langle \hat{S}_2\rangle| \\ \left|\frac{g_0}{\kappa}g_0\beta(\langle \hat{C^2}\rangle - \langle \hat{C}\rangle\langle \hat{C}_0\rangle)\right| &\sim \frac{|g_0N_a|}{\kappa}|g_0\beta\langle \hat{C}-\hat{C}_0\rangle| \\ \left|\frac{g_0}{\kappa}g_0\beta\langle \hat{S}_2\hat{S}_2\rangle\right| &\sim \frac{|g_0N_a|}{\kappa}|g_0\beta\langle \hat{S}_2\rangle|. \end{aligned} \tag{5.23}$$

As long as $|g_0N_a|/\kappa \ll 1$, these higher-order correlations can be neglected.

The scaling relations for $\hat{d}_\pm$ are then

$$\langle \hat{d}_-\rangle = \frac{2g_0\beta}{\kappa}\langle \hat{S}_2\rangle, \tag{5.24}$$

$$\langle \hat{d}_+\rangle = -i\frac{4g_0\beta}{\kappa}(\langle \hat{C}\rangle - \langle \hat{C}\rangle_0). \tag{5.25}$$

We can use these relations to determine the approximate size of the non-conservative terms in equation 5.12. Recalling that $V_0 = 2\hbar g_0|\beta|^2$, we have

$$2\hbar g_0\hat{d}_-^\dagger\hat{d}_- \approx V_0\frac{4g_0^2}{\kappa^2}|\langle \hat{S}_2\rangle|^2 \sim V_0\left(\frac{g_0N_a}{\kappa}\right)^2, \tag{5.26}$$

$$2\hbar g_0\hat{d}_+^\dagger\hat{d}_+ \approx V_0\frac{16g_0^2}{\kappa^2}|\langle \hat{C}\rangle - \langle \hat{C}\rangle_0|^2 \sim V_0\left(\frac{g_0N_a}{\kappa}\right)^2, \tag{5.27}$$

$$i\hbar g_0(\hat{d}_+^\dagger\hat{d}_- - \hat{d}_-^\dagger\hat{d}_+) = -V_0\frac{8g_0^2}{\kappa^2}\langle \hat{S}_2\rangle(\langle \hat{C}\rangle - \langle \hat{C}\rangle_0) \sim V_0\left(\frac{g_0N_a}{\kappa}\right)^2. \tag{5.28}$$

Each of these coupling constants is down from $V_0$ by at least a factor of $(g_0 N_a/\kappa)^2$; we can neglect them. The last terms involve products of $\beta$ with the fluctuation operators $\hat{d}_\pm$, which come in scaling as $V_0(g_0 N_a/\kappa)$ rather than $V_0(g_0 N_a/\kappa)^2$. It turns out that these are zero to first order, however:

$$\beta^* \hat{d}_+ + \beta \hat{d}_+^\dagger \sim -i\beta^* \frac{4g_0\beta}{\kappa}(\langle \hat{C} \rangle - \langle \hat{C} \rangle_0) + \beta i \frac{4g_0\beta^*}{\kappa}(\langle \hat{C} \rangle - \langle \hat{C} \rangle_0) = 0, \tag{5.29}$$

$$\beta^* \hat{d}_- - \beta \hat{d}_-^\dagger \sim \beta^* \frac{2g_0\beta}{\kappa}\langle \hat{S}_2 \rangle - \beta \frac{2g_0\beta^*}{\kappa}\langle \hat{S}_2 \rangle = 0. \tag{5.30}$$

Thus, we can also neglect these terms.

Finally, we return to the terms, $\langle \hat{d}_\pm [\hat{\Psi}^\dagger \hat{\Psi}, \hat{H}] \rangle$. The equations of motions for the atomic number density is

$$[\hat{\Psi}^\dagger \hat{\Psi}, \hat{H}] = i\frac{d\hat{\Psi}^\dagger \hat{\Psi}}{dt} = -\frac{\hbar^2}{2m}\left( \hat{\Psi}^\dagger(z)\frac{\partial^2 \hat{\Psi}(z)}{\partial z^2} - \frac{\partial^2 \hat{\Psi}^\dagger(z)}{\partial z^2}\hat{\Psi}(z) \right) \tag{5.31}$$

To first approximation, this is essentially $\langle \hat{d}_\pm \rangle$ times the expectation value of the atomic kinetic energy. The kinetic energy is approximately the square of the group velocity of the atomic wave-packet. In the tight-binding limit ($V_0 \geq 5E_R$), the energy of the single-particle wave-packet is given by

$$\hbar\epsilon = -\hbar 2J\cos(dq), \tag{5.32}$$

where $d$ is the lattice spacing, $q$ is the (continuous) quasi-momentum, and $J$ is the hopping energy. The group velocity is

$$v_g = \frac{\partial \epsilon}{\partial q} = 2Jd\sin(dq). \tag{5.33}$$

The maximum kinetic energy is then

$$T_0 = \frac{1}{2}m v_{g,0}^2 = \frac{1}{2}m(2Jd)^2 = \pi^2 E_R \left(\frac{\hbar J}{E_R}\right)^2. \tag{5.34}$$

The kinetic energy is about ten times the tunneling rate squared in units of the recoil energy. We can approximate the tunneling rate as

$$\hbar J = E_R e^{-V_0/4E_R}, \tag{5.35}$$

which indicates that the kinetic energy is on the order of ten recoils at most.

We can make the approximation,

$$\langle \hat{d}_{\pm}[\hat{\Psi}^{\dagger}\hat{\Psi}, \hat{H}]\rangle \approx \pi^2 E_R \left(\frac{\hbar J}{E_R}\right)^2 \langle \hat{d}_{\pm}\hat{\Psi}^{\dagger}\hat{\Psi}\rangle \leq \pi^2 E_R \langle \hat{d}_{\pm}\hat{\Psi}^{\dagger}\hat{\Psi}\rangle. \tag{5.36}$$

This term is a dispersive shift, and since

$$\pi^2 E_R \ll \hbar\kappa, \tag{5.37}$$

we may neglect it. Finally, ensuring that we can neglect all of these terms compared to the external potential requires explicit knowledge of the form of $V_{\text{ext}}$ and will therefore be left for the next section.

Thus, in the correlation hierarchy, each consecutive order scales as $|g_0|N_a/\kappa$ times the previous order. For instance, $\langle \hat{d}_{+}\hat{\Psi}^{\dagger}\hat{\Psi}\rangle$ scales as $|g_0|N_a/\kappa$ times $\langle \hat{\Psi}^{\dagger}\hat{\Psi}\rangle$. Therefore requiring $|g_0|N_a/\kappa \ll 1$ allows us to neglect all terms involving correlations between three or more operators. We reiterate finally that this condition is equivalent with the physical requirement that the numbers of photons in $\hat{d}_{\pm}$ are small compared with the number of photons in the symmetric mean field, since

$$|\langle \hat{d}_{\pm}\rangle| \sim \frac{|g_0\beta|N_a}{\kappa} \ll |\beta|. \tag{5.38}$$

With these approximations in hand, we solve equations (5.9) and (5.10) by adiabatically slaving the fields to the atomic motion, yielding.

$$\langle \hat{d}_{-}\rangle = \frac{-ig_0\beta\langle \hat{S}_2\rangle}{\Delta_p + i\kappa/2}, \tag{5.39}$$

$$\langle \hat{d}_{+}\rangle = \frac{2g_0\beta(\langle \hat{C}\rangle - \langle \hat{C}\rangle_0)}{\Delta_p + i\kappa/2}. \tag{5.40}$$

The equation of motion for the atomic field operator is

$$i\hbar\frac{d\hat{\Psi}(z)}{dt} = \left(-\frac{\hbar^2}{2m}\frac{d^2}{dz^2} + V_{\text{lat}}(z) + V_{\text{ext}}(z)\right)\hat{\Psi}(z), \tag{5.41}$$

and the probe field amplitude is given by

$$\langle \hat{d}_{-}(t)\rangle = \frac{-ig_0\beta}{\Delta_p + i\kappa/2}\langle \hat{S}_2\rangle. \tag{5.42}$$

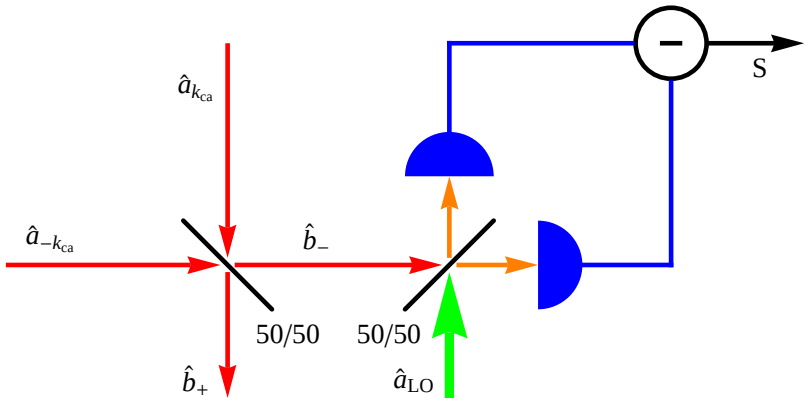


Figure 5.2: Schematic of the balanced heterodyne detection scheme. The out-coupled cavity beams, $\hat{a}_{\pm k_C}$, are combined to form symmetric ($\hat{b}_+$) and anti-symmetric ($\hat{b}_-$) modes. The antisymmetric mode beats against a strong local oscillator (LO), $\hat{a}_{LO}$ and photodetectors count the number of photons in the quadratures of $\hat{b}_-$. The difference of these counts is the signal.

Since the atoms are independent of each other and couple symmetrically to the light field, we can in equation (5.42) make the replacement,

$$\langle \hat{S}_2 \rangle \to N_a \langle \psi(t) | \sin(2k_C \hat{z}) | \psi(t) \rangle, \tag{5.43}$$

where $|\psi(t)\rangle$ is a single-particle state satisfying equation (5.41) with $\hat{\Psi}(z) \to |\psi(t)\rangle$.

### 5.1.3 Detection scheme and signal-to-noise ratio

Through equation (5.42), $\langle \hat{d}_- \rangle$ provides a measure of the atomic dynamics inside the cavity. In reference [85], two schemes for detection of atomic motion using the out-coupled cavity fields were presented. We here review the superior case, where balanced heterodyne detection of $\hat{d}_-$ is performed. Briefly, the signal is combined with a strong local oscillator (LO) at a 50/50 beam-splitter, and the two output signals are measured with photo-detectors and subtracted from each other. This differencing cancels the large mean-field signal created by the LO. The noise is dominated by the LO noise and is conveniently cancelled when computing their signal-to-noise ratio. The general setup is illustrated in figure 5.2.

In what follows, we compute the exact expressions for the signal and the signal-to-noise ratio for this heterodyne detection scheme. We use a basic quantum Langevin approach [44] combined with beam-splitter theory [76] to exactly calculate the signal power spectrum and signal variance, and the signal-to-noise ratio is computed as the ratio.

According to input-output theory [44] this field is proportional to

$$\hat{d}_{\text{out}} = \sqrt{\kappa}\ \hat{d}_{-} + \hat{d}_{\text{in}}. \tag{5.44}$$

Input-output theory relates the fields inside and outside a cavity using a quantum Langevin approach, writing the output (i.e. signal) field in terms of the input field and the field out-coupled from the cavity. Equation (5.44) has a simple interpretation as the superposition of two electromagnetic fields, $\sqrt{\kappa}\ \hat{d}_{-}$ and $\hat{d}_{\text{in}}$, and can be viewed as a boundary condition at the cavity output. In this case, the input field state is the vacuum, which results in $\langle \hat{d}_{\text{out}} \rangle = \sqrt{\kappa}\ \langle \hat{d}_{-} \rangle$.

The output field is combined at a 50/50 beam-splitter with a strong local oscillator. The output fields at the beam-splitter are given by

$$\begin{bmatrix} \hat{b}_2 \\ \hat{b}_1 \end{bmatrix} = \frac{1}{\sqrt{2}} \begin{bmatrix} -i & 1 \\ 1 & -i \end{bmatrix} \begin{bmatrix} \hat{d}_{\text{out}} \\ \hat{a}_{\text{LO}} \end{bmatrix}. \tag{5.45}$$

The intensities of these two fields are measured with photodetectors. These signals are subtracted from each other, mixed with an oscillating signal $\cos(\omega t)$ and integrated in time. The final signal is proportional to

$$\hat{N}(\omega, T) = \int_0^T dt \left( \hat{b}_2^{\dagger}(t)\hat{b}_2(t) - \hat{b}_1^{\dagger}(t)\hat{b}_1(t) \right) \cos(\omega t). \tag{5.46}$$

Defining

$$\alpha_{\text{LO}} = \langle \hat{a}_{\text{LO}} \rangle = |\alpha_{\text{LO}}| e^{-i\omega_{\text{LO}} t} e^{i\phi_{\text{LO}}}, \tag{5.47}$$

$$\hat{a}_{\text{LO}} = \alpha_{\text{LO}} + \hat{v}, \tag{5.48}$$

we can write

$$\hat{b}_2^\dagger \hat{b}_2 - \hat{b}_1^\dagger \hat{b}_1 = i(\alpha_{\rm LO}^* \hat{d}_{\rm out} - \alpha_{\rm LO} \hat{d}_{\rm out}^\dagger) + i(\hat{v}^\dagger \hat{d}_{\rm out} - \hat{d}_{\rm out}^\dagger \hat{v}) \approx i(\alpha_{\rm LO}^* \hat{d} - \alpha_{\rm LO} \hat{d}^\dagger), \quad (5.49)$$

where we have taken $\hat{d} = \sqrt{\kappa}\ \hat{d}_-$ for convenience, and we have assumed that the local oscillator has a very large amplitude. Finally,

$$\begin{aligned} \hat{N}(\omega, T) &= \int_0^T dt\ i \left( |\alpha_{\rm LO}| e^{i\omega_{\rm LO} t} e^{-i\phi_{\rm LO}} \hat{d}(t) - |\alpha_{\rm LO}| e^{-i\omega_{\rm LO} t} e^{i\phi_{\rm LO}} \hat{d}^\dagger(t) \right) \cos(\omega t) \\ &= \frac{iT|\alpha_{\rm LO}| e^{-i\phi_{\rm LO}}}{2} \hat{d}(\omega_{\rm LO} + \omega) + \frac{iT|\alpha_{\rm LO}| e^{i\phi_{\rm LO}}}{2} \hat{d}(\omega_{\rm LO} - \omega) + \text{H.c.} \end{aligned} \quad (5.50)$$

where we have defined

$$\hat{d}(\omega) = \frac{1}{T} \int_0^T dt\ e^{i\omega t} \hat{d}(t). \quad (5.51)$$

The signal variance is given by

$$\langle \Delta \hat{N}^2(\omega, T) \rangle = \left\langle (\hat{N}(\omega, T) - \langle \hat{N}(\omega, T) \rangle)^2 \right\rangle. \quad (5.52)$$

We define the signal fluctuation operator,

$$\Delta \hat{d}(\alpha) = \hat{d}(\alpha) - \langle \hat{d}(\alpha) \rangle, \quad (5.53)$$

and make the assumption that the signal is at all times a coherent state, in which case $\Delta \hat{d}(\alpha)$ is in the vacuum, and therefore only anti-normal-ordered correlation functions involving these operators are non-zero. In addition, we assume that

$$\langle \Delta \hat{d}(t) \Delta \hat{d}(t') \rangle = \delta(t - t'), \quad (5.54)$$

which is approximately valid when the interrogation time $T$ is much larger than $1/\kappa$. We are left with

$$\begin{aligned} \frac{4}{T^2 |\alpha_{\rm LO}|^2} \langle \Delta \hat{N}^2(\omega, T) \rangle &= \langle \Delta \hat{d}(\omega_{\rm LO} + \omega) \Delta \hat{d}^\dagger(\omega_{\rm LO} + \omega) \rangle + \langle \Delta \hat{d}(\omega_{\rm LO} + \omega) \Delta \hat{d}^\dagger(\omega_{\rm LO} - \omega) \rangle \\ &\quad + (\omega \to -\omega). \end{aligned} \quad (5.55)$$

Noting that

$$\begin{aligned}\langle \Delta\hat{d}(\alpha)\Delta\hat{d}^\dagger(\alpha')\rangle &= \frac{1}{T}\int_0^T dt\ e^{i\alpha t}\frac{1}{T}\int_0^T dt'\ e^{-i\alpha' t'}\langle \Delta\hat{d}(t)\Delta\hat{d}^\dagger(t')\rangle \\ &= \frac{1}{T}\int_0^T dt\ e^{i\alpha t}\frac{1}{T}\int_0^T dt'\ e^{-i\alpha' t'}\delta(t-t') \\ &= \frac{1}{T}\left(\frac{1}{T}\int_0^T dt\ e^{i(\alpha-\alpha')t}\right), \end{aligned} \tag{5.56}$$

we can see that only the diagonal terms contribute here—with a factor of $1/T$—so that

$$\langle \Delta\hat{N}^2(\omega,T)\rangle = \frac{|\alpha_{\rm LO}|^2 T}{2}. \tag{5.57}$$

We are finally in a position to compute the signal-to-noise ratio. We define the signal quadrature operator,

$$\hat{q}_-(\alpha,\phi_{\rm LO}) = \frac{i}{\sqrt{2}}(e^{-i\phi_{\rm LO}}\hat{d}_-(\alpha) - e^{i\phi_{\rm LO}}\hat{d}_-^\dagger(\alpha)). \tag{5.58}$$

in which case our signal is given by

$$\langle \hat{N}(\omega,T)\rangle = \frac{T|\alpha_{\rm LO}|\sqrt{\kappa}}{\sqrt{2}}\langle \hat{q}_-(\omega_{\rm LO}+\omega,\phi_{\rm LO})\rangle + \frac{T|\alpha_{\rm LO}|\sqrt{\kappa}}{\sqrt{2}}\langle \hat{q}_-(\omega_{\rm LO}-\omega,\phi_{\rm LO})\rangle. \tag{5.59}$$

The signal-to-noise is given by the ratio of the signal power to signal variance, which is

$$\mathrm{SNR} = \frac{|\langle \hat{N}(\omega,T)\rangle|^2}{\langle \Delta\hat{N}^2(\omega,T)\rangle} = \kappa T|\langle \hat{q}_-(\omega_{\rm LO}-\omega,\phi_{\rm LO})\rangle + (\omega\to-\omega)|^2. \tag{5.60}$$

If we are looking for a particular dynamical frequency $\omega_0$ of the atomic motion, we set $\omega \approx \omega_{\rm LO} - \omega_0$. For the system investigated below, we find that when the field has a large amplitude at $\omega_0$, it does not have a large amplitude at $2\omega_{\rm LO} - \omega_0$. Thus, we may drop the first term, leaving

$$\mathrm{SNR} = \kappa T|\langle \hat{q}_-(\omega,\phi_{\rm LO})\rangle|^2. \tag{5.61}$$

By varying the phase $\phi_{\rm LO}$ on the local oscillator, we can maximize this signal-to-noise ratio.

## 5.2 Results

In this section, we consider the motion of atoms confined in the optical lattice in the presence of gravity,

$$V_{\text{ext}}(z) = mgz, \tag{5.62}$$

and use the scheme outlined in the previous section to probe the motion of the atoms. Gravity measurements are important for instance for optical lattice clocks [79]. For this reason, we treat the specific system of a gas of $^{87}$Sr atoms, although the method certainly applies to many species of atoms. The parameters for the coupled atom-cavity system are chosen to reflect current experimental conditions. They are $\lambda_{\text{C}} = 2\pi/k_{\text{C}} = 813$ nm, $\hbar\kappa = 100E_R$, $\Delta_p = \omega_p - \omega = 0$, $\hbar g_0 = 10^{-4}E_R$, and $N_a = 10^4$, implying derived parameters of $E_R \approx 2\pi$ 4 kHz $\hbar$ and $mgd \approx 0.25E_R$; $E_R = \hbar^2 k_{\text{C}}^2/2m$ is the recoil energy of the lattice, and $d = \pi/k_{\text{C}}$ is the lattice spacing.

We have to ensure that the back-action of both $\hat{d}_-$ and $\hat{d}_+$ on the atoms is still negligible. Specifically, the coupling strengths in equation (5.12) must be small compared to the characteristic coupling strength of $V_{\text{ext}}$, $\hbar\omega_B = mgd$. These conditions are met if $|V_0|(g_0 N_a/\kappa)^2 \ll \hbar\omega_B$. This inequality is satisfied for the parameters above. While these conditions are necessary, the exact criteria for being able to neglect the back-action of the fields on the atoms requires more careful numerical study. We do not perform these investigations here.

Within this setup, we envision an experiment in which the atoms are initially loaded into a harmonic trap. A vertical one-dimensional optical lattice is slowly ramped on so that the atoms are in the ground state of the combined potential of trap and lattice for a non-interacting gas. The trap is switched off over a time that is long compared to the time-scale of vibrational dynamics in order to prevent inter-band transitions during the switch-off. The gas is then allowed to evolve under gravity. In the presence of such a constant force, the atoms undergo Bloch oscillations. This dynamics is briefly reviewed

in the following discussion.

### 5.2.1 System dynamics: Bloch oscillations

The central result of the theory describing Bloch oscillations is the acceleration theorem, based on a semi-classical equation of motion [8], which states that the average quasi-momentum of a wave-packet restricted to the first band increases linearly in time until it reaches the Brillouin zone (BZ) boundary, at which point it is Bragg-reflected. Explicitly, this is

$$\hbar\langle q\rangle(t) = \hbar\langle q\rangle(0) + mgt, \tag{5.63}$$

where the quasi-momentum, $q$, is restricted to the range, $-k_{\mathrm{C}} \leq q \leq k_{\mathrm{C}}$. Since the group velocity of the atomic wave-packet is given by the derivative of the dispersion relation [8], the periodic nature of the quasi-momentum implies that the atomic momentum oscillates at a frequency, $\omega_B = mgd/\hbar$. These Bloch oscillations will persist as long as there is negligible Landau-Zener tunneling to higher bands. Each time the wave-packet reaches the BZ boundary, a fraction of population is transferred to the second band, given by [91]

$$P_{LZ} = \exp\left(-\frac{\pi^2}{8}\frac{\Delta^2}{mgdE_R}\right), \tag{5.64}$$

where $\Delta$ is the band-gap at the boundary. When $\Delta^2 < 4mgdE_R$, the population transfer is appreciable, and vibrational dynamics within lattice sites significantly complicate the behavior of the atoms. For this reason, we restrict our attention to lattice depths greater than $3E_R$, where $P_{LZ}$ is at most $10^{-5}$ for our choice of parameters.

In order to understand how Bloch oscillations are reflected in the time-dependence of the probe field, we carefully consider equation (5.42). The operator, $\sin(2k_{\mathrm{C}}\hat{z})$, is periodic in space with period $d$ and has odd parity, implying that it connects two Bloch states, $|\psi_q^{(n)}\rangle$ and $|\psi_{q'}^{(n')}\rangle$, only if the quasi-momenta are equal, $q = q'$, and the bands

satisfy $n - n' = \text{odd}$. Expanding the atomic wave function in the Bloch states as

$$|\psi\rangle = \sum_{n,q} c_q^{(n)} |\psi_q^{(n)}\rangle, \tag{5.65}$$

we can approximate the matrix element in equation (5.42) as

$$\langle\psi| \sin(2k_C\hat{z})|\psi\rangle \approx \sum_q \rho_{q,q}^{(1,2)} + h.c., \tag{5.66}$$

where $\rho_{q,q}^{(1,2)} = c_q^{(1)*} c_q^{(2)}$ is the coherence between bands one and two. This assumes an initial state confined to the first band in the case of negligible coupling to bands three and higher. Using equation (5.41), we can derive an approximate equation of motion for the coherence; it is

$$i\frac{d\rho_{q,q}^{(1,2)}}{dt} = \Delta^{(1,2)}(q)\rho_{q,q}^{(1,2)} + \omega_B \rho_q^{(1)}, \tag{5.67}$$

where $\rho_q^{(1)}$ is the population of the $q$-quasi-momentum state in the first band, and $\hbar\Delta^{(1,2)}(q) = E_q^{(2)} - E_q^{(1)}$ is the energy difference between the $q$-quasi-momentum Bloch states in the first two bands. Since $\Delta^{(1,2)}(q) \gg \omega_B$, the coherence follows the first-band population adiabatically. In this approximation, $\rho_{q,q}^{(1,2)} = -\rho_q^{(1)}\omega_B/\Delta^{(1,2)}(q)$.

Combining this expression for a wave-packet that is narrow in quasi-momentum with equation (5.63), equation (5.42) becomes approximately

$$\langle\hat{d}_-(t)\rangle \approx \frac{ig_0\beta N_a}{\Delta_p + i\kappa/2}\frac{\omega_B}{\Delta^{(1,2)}(mgt)}. \tag{5.68}$$

This expression implies that the probe field amplitude is largest when the atomic wave-packet is centered at the BZ boundary since $\Delta^{(1,2)}(mgt)$ is smallest at this point.

Equations (5.41) and (5.42) are numerically integrated for an initial state that is a Gaussian of spatial width, $\sigma$, projected into the first band. This approximates the ground state of the combined potential of lattice and harmonic trap for a non-interacting gas. An example of the system dynamics is illustrated in figure 5.3, where $V_0 = -3E_R$, and $\sigma = 2d$. A vertical slice through figure 5.3(a) is the wave function density in the

first band plotted versus quasi-momentum at an instant in time. The center of this wave-packet moves linearly in time and is reflected at the BZ boundary ($q = k_{\mathrm{C}}$), as in equation (5.63). Bloch oscillations are illustrated in figure 5.3(b), where the atomic momentum oscillates in time. Finally, the response of the probe field to this dynamics is illustrated in figure 5.3(c). As predicted above, the probe field intensity peaks when the atomic wave-packet reaches the BZ boundary.

### 5.2.2 Signal and SNR

As described in section 5.1, the probe field is combined at the cavity output with a strong local oscillator, and the resulting signal is proportional to a quadrature of the probe field, equation (5.58). An example of such a signal is plotted in figure 5.4. There is a clear peak at the Bloch oscillation frequency in the signal power spectrum, but there are also several harmonics present. In calculating the SNR, equation (5.61), we place a notch-filter about $\omega_B$ and count only the total number of photons out-coupled from the quadrature at this frequency.

There are a few properties of the system that can affect the SNR. First, the width of the initial wave-packet has an effect. It is easiest to see why this is so by taking as the initial state a Wannier function, which is a coherent superposition of Bloch states in a single band, populated equally. According to equation (5.63), the wave-packet is continuously reaching the BZ boundary, and the oscillation in the signal is washed out. Second, when the lattice is too deep, the first two bands are essentially flat, in which case $\Delta_q^{(1,2)}$ does not change with quasi-momentum, eliminating the oscillations in the signal according to equation (5.68).

The temperature of the atomic gas can also significantly influence the SNR. For a finite temperature, the pure state in equation (5.43) is replaced with a density matrix. The incoherent sum over different states of the atoms will alter the expectation value, possibly reducing it. In addition, the temperature and chemical potential of the gas de-

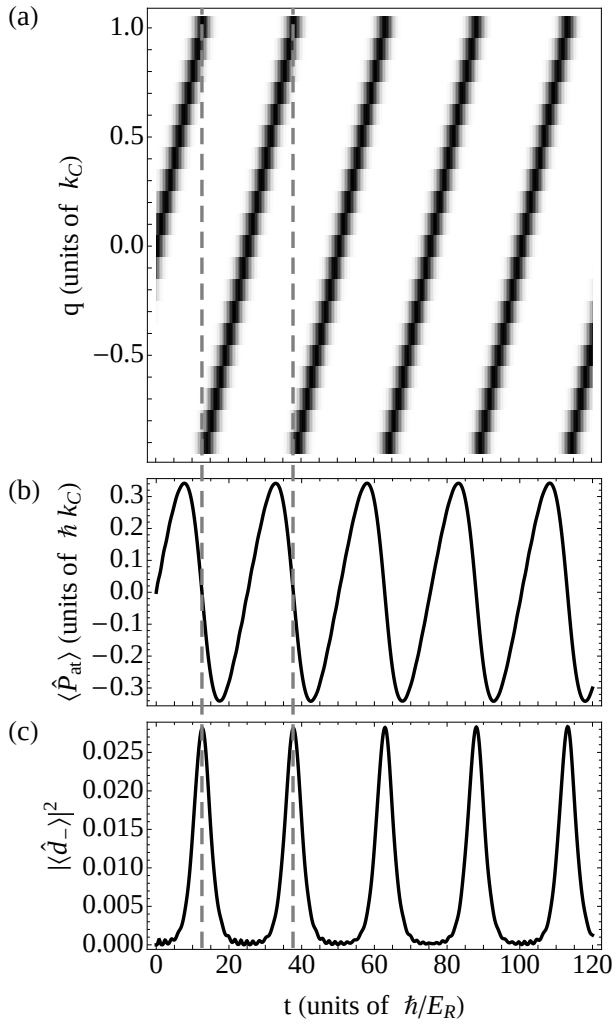


Figure 5.3: Example of system dynamics for $V_0 = -3E_R$ and initial state a Gaussian of width $\sigma = 2d$ projected into the first band. (a) Atomic density in the first band plotted versus quasi-momentum. White corresponds to zero population, black to maximal population. Population in the second band is at most $0.001N_a$. (b) Expectation value of atomic momentum illustrating Bloch oscillations. (c) Number of photons in the probe field.

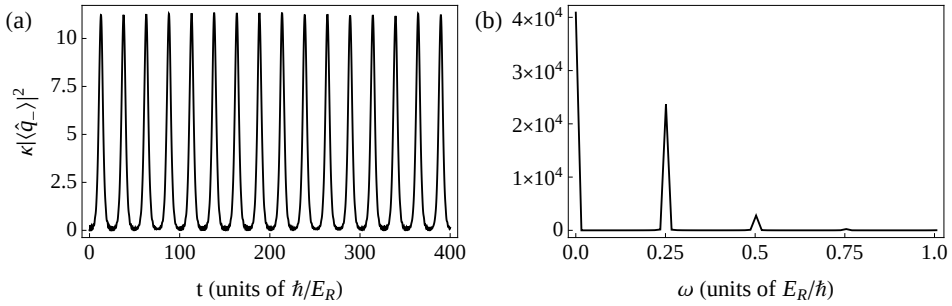


Figure 5.4: Examples of the (a) signal power and (b) signal power spectrum, computed with parameters, $V_0 = -3E_R$, $\hbar g_0 = 10^{-4}E_R$, $N_a = 10^4$, and $\hbar\kappa = 100E_R$. The signal displays a clear oscillation at the Bloch frequency, $\omega_B = 0.25E_R/\hbar$.

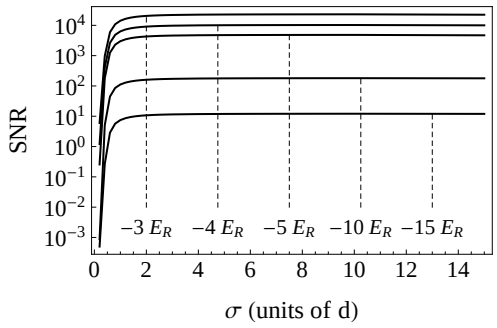


Figure 5.5: Signal-to-noise ratio as a function of the initial wave-packet width for an interrogation time of 1s and for lattice depths of $V_0 = -3, -4, -5, -10, -15 E_R$. For $\sigma < 2d$, the SNR is reduced due to parts of the wave-packet constantly moving past the Brillouin zone boundary, where the signal peaks. The SNR saturates near $\sigma = 2d$.

termine the relative populations of the various Bloch states, and appreciable population in higher bands can destroy Bloch oscillations. As long as the temperature is smaller than the bandgap, $k_B T \ll \hbar \Delta_{k_C}^{(1,2)}$, this effect will be small.

Finally, the replacement, equation (5.43), can not be made when the atoms are not independent, e.g. if they interact with each other. In this case it is possible that the scaling of the SNR with the number of atoms will be reduced from $N_a^2$. A proper treatment of thermal and interaction effects is necessary for exact results. Here, we neglect both interactions and finite temperature for the case of $^{87}$Sr atoms, in which case equation (5.43) is valid.

Equation (5.12) is numerically integrated for a time $t = 400\hbar/E_R$. The resulting wave function is used to compute the probe field amplitude, equation (5.42), which is Fourier-transformed and squared, yielding the power spectrum. The SNR is computed and scaled up linearly to an interrogation time of 1s, which assumes that coherence time of the Bloch oscillations is longer than 1s.

The results are plotted in figures 5.5 and 5.6. The SNR rises from zero for small wave-packet widths and saturates near $\sigma = 2d$. The decrease in SNR for $\sigma < 2d$ is a result of the fact that the wave-packet is wide in quasi-momentum, which means that

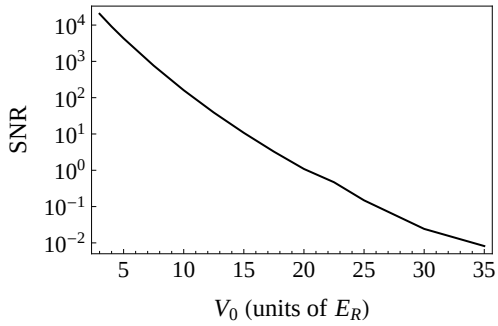


Figure 5.6: Signal-to-noise ratio as a function of lattice depth for $\sigma = 2d$ and an interrogation time of $1s$. For $|V_0| < 3E_R$, significant Landau-Zener tunneling to the second band destroys Bloch oscillations. For $|V_0| > 3E_R$, the SNR decreases due to the increasing flatness of the lowest band.

a significant portion of the wave-packet is at the BZ boundary for all times. We get a maximum when the lattice depth is relatively small, $|V_0| \approx 3E_R$, and the SNR decreases with increasing lattice depth.

## 5.3 Conclusion

We have described a general cavity QED system in which properties of atomic dynamics can be probed *in situ* and non-destructively. One cavity field is strong enough to act as a conservative lattice potential for the atoms, and the other cavity field is weak so that it acts as a non-destructive probe of atomic motion. This technique is applied to the detection of Bloch oscillations. Balanced heterodyne detection of the probe field at the cavity output combined with integration in time and across the atomic cloud allows for SNRs as high as $10^4$.

Examining equations (5.42) and (5.61), we can see that the SNR can be increased by either decreasing the cavity linewidth, $\kappa$, at fixed lattice depth and atom-cavity coupling or increasing the coupling constant, $g_0$, at fixed $V_0$ and $\kappa$. The linewidth can be decreased as long as the system remains in the bad cavity limit. However, a linewidth of $\kappa = 100E_R$ is already very small from an experimental standpoint, so decreasing it beyond this level is a technological challenge. On the other hand, $g_0$ can be varied merely by varying the detuning between the cavity fields and atomic transitions. In addition, the SNR scales with the square of the number of atoms, so increasing $N_a$ beyond the $10^4$ level assumed in this paper is also desirable. This can all be done to the extent that the conditions outlined in section 5.1 and section 5.2 are still met.

This scheme can be extended for use in detection of various atomic properties, and the measurement of Bloch oscillations itself can be viewed as a general DC probe for atomic dynamics and states. For instance, Bloch oscillations may be used for measurement of fundamental constants [28] and for Casimir forces [132]. Varying the detuning between two lattice beams gives rise to an effective acceleration of the lattice [91], and

band physics may be probed by varying the Bloch oscillation frequency in such a setup. Breakdown of Bloch oscillations are a signature of many-body effects in an atomic gas [42], and this is signaled by a reduction in SNR compared to the non-interacting case.

Two generalizations of this measurement technique are readily realizable. We may implement a time-periodic force whose tunable driving frequency can be a spectroscopic probe of atomic dynamics. The simplest examples of this include shaking the lattice [62] and modulating the amplitude of the lattice [1]. Another important extension of the method involves measuring higher-order correlation functions of the out-coupled probe field. Since one cavity field operator couples to two atomic field operators (see for instance equation (5.9)), higher-order properties of the atoms such as density-density correlations can easily be measured with standard quantum optical techniques. The use of higher-order correlation functions of the probe field is a starting point for generalizing this technique to probe many-body physics in optical lattices.

# Chapter 6

## Cavity QED Measurements of Many-Body Dynamics Near the Mott-Insulator Regime

In the previous chapter, we presented a method for probing the dynamics of non-interacting atoms trapped in an optical lattice by monitoring the light field out-coupled from an optical cavity. For this particular measurement, we predicted signal-to-noise (SNR) ratios as high as $10^4$. There were a number of drawbacks in this technique. First, the condition that the cavity fields act simultaneously as both the probe field and the lattice field limited the measurement to one where the atomic dynamics induce at least coherences between bands. Since the signal went to zero as the lattice depth was increased, this method was restricted to small lattice depths. In addition, we were not able to vary the probe wavelength relative to the lattice wavelength. Finally, the method worked only for atomic wave-packets with widths of at least a few lattice constants

In this chapter, we relax the condition that the cavity fields act as both lattice and probe fields, allowing us to optimize the signal as a function of system parameters such as probe wavelength even in systems where the lattice depth is large. The detection scheme is applied to the atomic dynamics of atoms near the Mott-insulator regime that are subjected to a constant external force. This system is modeled by a single-band Bose-Hubbard model with a linear energy shift. Atoms are allowed to hop around the lattice when the energy offset between adjacent wells is nearly equal to the two-particle interaction strength. This physics is closely related to that exploited in atomtronic

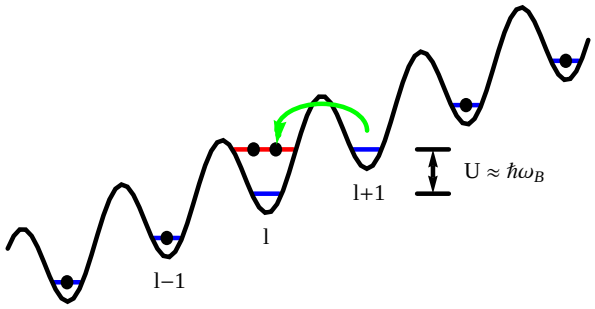


Figure 6.1: Schematic of the atomic system. In the Mott-insulator regime with unit-filling, there is exactly one particle per site. When the lattice is tilted so that the difference in energy $\hbar\omega_B$ between adjacent wells is equal to the two-particle interaction strength $U$, particles are free to hop one site to the left. Assuming the rest of the lattice wells each contain one atom, the state pictured is the one-dipole state, $|1;l\rangle \propto \hat{b}_l^\dagger \hat{b}_{l+1}|\psi_{\rm MI}\rangle$.

systems to emulate electronic devices such as diodes [103].

We first develop the theory of atomic dynamics in this system, using the methods described in reference [112] as a starting point. Following this, we couple this system to the two counter-propagating modes of a ring cavity and examine the behavior of the lattice fields in this special atomic regime.

## 6.1 Atomic Dynamics

The Hamiltonian for atoms moving in a one-dimensional optical lattice in the presence of a constant force is given by

$$\hat{H} = \int dz\ \hat{\Psi}^\dagger(z)\left(-\frac{\hbar^2}{2M}\frac{d^2}{dz^2} + V_0\cos^2(k_{\rm L}z) + Maz + \hbar g_0\hat{\Psi}^\dagger(z)\hat{\Psi}(z)\right)\hat{\Psi}(z), \qquad (6.1)$$

where $F = Ma$ is the force acting on the particles of mass $M$. As in Chapter 3, we expand the atomic field operators in Wannier states. In the tight-binding regime ($V_0 \geq 10E_R$), the Hamiltonian reduces to the standard Bose-Hubbard model with an extra linear shift,

$$\hat{H}_{\rm A} = \sum_j(\epsilon + MgZ + Mgdj)\hat{b}_j^\dagger\hat{b}_j - J\sum_{\langle j,k\rangle}\hat{b}_j^\dagger\hat{b}_k + \frac{U}{2}\sum_j\hat{b}_j^\dagger\hat{b}_j^\dagger\hat{b}_j\hat{b}_j, \qquad (6.2)$$

where

$$Z = \int dz\ w^*(z) z w(z). \tag{6.3}$$

We have dropped the band index $n$ since in this regime, all of the dynamics occurs within the first band, $n = 1$. This system is illustrated in figure 6.1.

This Hamiltonian is the starting point for the physics investigated in this chapter. We restrict our attention to parameter regimes near the Mott-insulator phase, $U \gg J$, with the linear shift approximately equal to the on-site interaction energy,

$$U \approx \hbar\omega_B = Mgd. \tag{6.4}$$

In this regime, if the system is initialized in the Mott insulator state, the atomic dynamics considerably simplifies. This simplification can be effected by deriving an effective low-energy Hamiltonian in a reduced Hilbert space consisting of states near-resonant with the integer-filled number state. Since particle numbers are conserved, we can drop the on-site energy terms involving $\epsilon$ and $MgZ$. In addition, we mainly consider a filling fraction of 1. The general behavior observed should be sustained for larger integer filling fractions. Finally, we consider finite-sized lattices with $N$ sites.

### 6.1.1 Dipole Hamiltonian

As an approximation to the Mott-insulator state, we consider the unit-filled state,

$$|\psi_{\mathrm{MI}}\rangle = \left( \prod_{k=1}^{N} \hat{b}_k^\dagger \right) |0\rangle. \tag{6.5}$$

This state has energy

$$E_{\mathrm{MI}} = \langle \psi_{\mathrm{MI}} | \hat{H}_{\mathrm{A}} | \psi_{\mathrm{MI}} \rangle = \frac{1}{2} N(N+1)\hbar\omega_B. \tag{6.6}$$

It is directly connected via the hopping part of the Hamiltonian to the states,

$$|1;l\rangle = \frac{1}{\sqrt{2}}\hat{b}_l^\dagger \hat{b}_{l+1}|\psi_{\mathrm{MI}}\rangle, \tag{6.7}$$

$$|1;l^+\rangle = \frac{1}{\sqrt{2}}\hat{b}_{l+1}^\dagger \hat{b}_l|\psi_{\mathrm{MI}}\rangle, \tag{6.8}$$

$$l = 1, \ldots N-1, \tag{6.9}$$

which respectively have energies

$$E_{1;l} = \langle 1;l|\hat{H}_{\mathrm{A}}|1;l\rangle = \frac{1}{2}N(N+1)\hbar\omega_B + U - \hbar\omega_B, \tag{6.10}$$

and

$$E_{1;l^+} = \langle 1;l^+|\hat{H}_{\mathrm{A}}|1;l^+\rangle = \frac{1}{2}N(N+1)\hbar\omega_B + U + \hbar\omega_B, \tag{6.11}$$

The state $|1;l\rangle$ has one particle per site except at sites $l$ and $l+1$ where there are two and zero particles, respectively. The state $|1;l^+\rangle$ is similar except that the number of particles on sites $l$ and $l+1$ are zero and two, respectively. The MI state is also connected to states where the two-particle and zero-particle sites are not adjacent. However, since the coupling is second order in the hopping $J$, and the states are separated in energy, we can neglect them as long as we consider small enough timescales for the dynamics.

We work in the parameter regime where

$$U \approx \hbar\omega_B, \tag{6.12}$$

$$|J| \ll U + \hbar\omega_B. \tag{6.13}$$

The states $|1;l^+\rangle$ then couple to $|\psi_{\mathrm{MI}}\rangle$ with coupling constant,

$$g_{MI,+} \sim \frac{J^2}{U + \hbar\omega_B} \ll J, \tag{6.14}$$

so we can neglect these states.

This argument easily generalizes when we consider, for instance, the states that $|1;l\rangle$ are connected to. These consist of states where two particles have been moved one

site to the left,

$$|2;l,j\rangle = \frac{1}{2}\hat{b}_l^\dagger \hat{b}_{l+1} \hat{b}_j^\dagger \hat{b}_{j+1} |\psi_{\mathrm{MI}}\rangle : \begin{array}{c} j = 1, \ldots, l-2 \\ l = 3, \ldots, N-1 \end{array} . \tag{6.15}$$

The domains chosen for the site indices $j$ and $l$ ensure that if there is a "hole" at sites $j$ and $l$, then on each of the sites $l+1$ and $j+1$, there are two particles. These states have energy,

$$E_{1;l} = \langle 1;l|\hat{H}_{\mathrm{A}}|1;l\rangle = \frac{1}{2}N(N+1)\hbar\omega_B + 2(U - \hbar\omega_B), \tag{6.16}$$

and again, since $U \approx \hbar\omega_B$, these states are near-resonant with the $|1;l\rangle$ states and are connected with coupling proportional to $J$.

In general, the near-resonant subspace is spanned by the states,

$$|M;k_M,\ldots,k_1\rangle = \frac{1}{\sqrt{2^M}} \prod_{i=1}^{M} \hat{b}_{k_i}^\dagger \hat{b}_{k_i+1} |, \tag{6.17a}$$

$$k_i = 2i-1, \ldots, k_{i+1} - 2, \tag{6.17b}$$

$$k_M = 2M-1, \ldots, N-1. \tag{6.17c}$$

The parameter, $M$, counts the number of dipoles—that is, the number of zero-particle/two-particle adjacent-site pairs—in the state $|M;k_M,\ldots,k_1\rangle$, and the two-particle sites are given by the site indices $\{k_M,\ldots,k_1\}$. The maximum number of dipoles in an $N$-site lattice is $\lfloor N/2 \rfloor$, where $\lfloor\cdot\rfloor$ is the floor function. The total number of dipole states in the $M$-dipole subspace is given by

$$n_M = \frac{(N-M)!}{M!(N-2M)!} = \binom{N-M}{M}. \tag{6.18}$$

We enumerate the states as

$$n_{k_M,\ldots,k_1} = 1 + \sum_{m=1}^{M} \binom{k_m - m}{m}. \tag{6.19}$$

A state $|M+1;k_{M+1},\ldots,k_1\rangle$ is connected via the hopping terms to the states $|M;l_M,\ldots,l_1\rangle$ where we have simply removed one of the $k_i$'s. Since this connection

implies a particle hopping onto an already occupied site, we get an extra factor of $\sqrt{2}$ due to the bosonic nature of the particles. The Hamiltonian restricted to these subspaces can be written as

$$\hat{H}_D = \frac{1}{2}N(N+1)\hbar\omega_B + \sum_{M=0}^{\lfloor N/2 \rfloor} \hat{H}^{(M)} + \sum_{M=0}^{\lfloor N/2 \rfloor - 1} \hat{H}_J^{(M\to M+1)} + \text{H.c.}, \tag{6.20a}$$

$$\hat{H}^{(M)} = \sum_{k_M,\ldots,k_1} M(U - \hbar\omega_B)|M; k_M, \ldots, k_1\rangle\langle M; k_M, \ldots, k_1|, \tag{6.20b}$$

$$\begin{aligned}\hat{H}_J^{(M\to M+1)} = -J\sqrt{2} \sum_{k_{M+1},\ldots,k_1} & |M+1; k_{M+1}, \ldots, k_1\rangle \\ & \times \sum_{n=1}^{M+1} \langle M; k_{M+1}, \ldots, k_{n+1}, k_{n-1}, \ldots, k_1|,\end{aligned} \tag{6.20c}$$

where it is understood that for $M = 0$, there is no sum over $k_i$'s, and the single state is exactly $|\psi_{\text{MI}}\rangle$.

### 6.1.2 Symmetric Hamiltonian

We can get an idea of how to further simplify this Hamiltonian by first considering the coupling between the Mott-insulator state and the one-dipole subspace, given by

$$\hat{H}_J^{(0\to 1)} = -J\sqrt{2} \sum_{l=1}^{N-1} |1; l_1\rangle\langle\psi_{\text{MI}}|. \tag{6.21}$$

We define a new basis for the one-dipole subspace by

$$|1; l\rangle = \frac{1}{\sqrt{N-1}} \sum_{m=0}^{N-2} e^{-i2\pi ml/N-1} |1_m\rangle. \tag{6.22}$$

Renaming $|\psi_{\text{MI}}\rangle$ as $|0\rangle$ (we can think of this state as the dipole "vacuum"), $\hat{H}_J^{(0\to 1)}$ becomes

$$\hat{H}_J^{(0\to 1)} = -J\sqrt{2}|1_0\rangle\langle 0|. \tag{6.23}$$

Consequently, as far as the dipole vacuum is concerned, the only relevant state in the one-dipole subspace is $|1_0\rangle$. The states $|1_{m\neq 0}\rangle$ do not couple to $|0\rangle$ so they can be neglected.

The problem is more complicated for the general coupling problem. Taking the above as a guide, we define a new basis, $|M_m\rangle$, for the $M$-dipole subspace by

$$|M_m\rangle = \frac{1}{\sqrt{n_M}} \sum_{k_M,\ldots,k_1} e^{i2\pi m n_{k_M,\ldots,k_1}/n_M} |M; k_M, \ldots, k_1\rangle, \tag{6.24}$$

$$|M; k_M, \ldots, k_1\rangle = \frac{1}{\sqrt{n_M}} \sum_{m=0}^{n_M-1} e^{-i2\pi m n_{k_M,\ldots,k_1}/n_M} |M_m\rangle. \tag{6.25}$$

In terms of these new states, $\hat{H}_J^{(M\to M+1)}$ becomes

$$\begin{aligned}\hat{H}_J^{(M\to M+1)} &= -J\sqrt{2} \sum_{k_{M+1},\ldots,l_1} |M+1; k_{M+1}, \ldots, k_1\rangle \\ &\quad \times \sum_{n=1}^{M+1} \frac{1}{\sqrt{n_M}} \sum_{m=0}^{n_M-1} e^{i2\pi m n_{k_{M+1},\ldots,k_{n+1},k_{n-1},\ldots,k_1}/n_M} \langle M_m| \\ &= -J\sqrt{2} \sum_{m=0}^{n_M-1} (M+1)\sqrt{\frac{n_{M+1}}{n_M}} |M+1; \psi_m\rangle\langle M_m|. \end{aligned} \tag{6.26}$$

where we have defined the states,

$$|M+1; \psi_m\rangle = \sum_{k_{M+1},\ldots,k_1} \sum_{n=1}^{M+1} \frac{e^{i2\pi m n_{k_{M+1},\ldots,k_{n+1},k_{n-1},\ldots,k_1}/n_M}}{(M+1)\sqrt{n_{M+1}}} |M+1; k_{M+1}, \ldots, k_1\rangle. \tag{6.27}$$

This new set of states is not identical with the set defined in equation (6.24). We can see this by noting that each state in equation (6.24) gets multiplied by one phase only, whereas each state in the expansion, equation (6.27), is multiplied by a sum of phases. These new states do not comprise an orthogonal set, and in general they are not normalized. We note however that $|M+1; \psi_0\rangle = |(M+1)_0\rangle$.

If the system is initialized in the state $|0\rangle$, then for short times, this state will evolve into $|1_0\rangle$, which will in turn evolve into $|2_0\rangle$, as we can see from taking the special case $\hat{H}_J^{(1\to 2)}$ above. Since $|(M+1)_0\rangle$ is not in general orthogonal to $|M+1; \psi_{m\neq 0}\rangle$, it is coupled to $|M_{m\neq 0}\rangle$ through these states. For instance, $|2_0\rangle$ is coupled to the states $|1_{m\neq 0}\rangle$ through other states within the two-dipole subspace. If the overlap between these states is small, however, then we can neglect them as long as we evolve only for short enough times.

We can compute these overlaps as

$$S^{(M)}_{m'm} = \langle M;\psi_{m'}|M;\psi_m\rangle \tag{6.28}$$

$$= \frac{1}{M^2}\frac{1}{n_M}\sum_{n',n=1}^{M}\sum_{k_M,\ldots,k_1} e^{i2\pi m n_{k_M,\ldots,k_{n+1},k_{n-1},\ldots,k_1}/n_{M-1}} \times e^{-i2\pi m' n_{k_M,\ldots,k_{n'+1},k_{n'-1},\ldots,k_1}/n_M - 1}. \tag{6.29}$$

In order to characterize the total overlap of the $|M;\psi_{m\neq 0}\rangle$'s with $|M_0\rangle$, we compute the quantity,

$$S^{(M)}_0 = \sqrt{\sum_{m\neq 0}\left|S^{(M)}_{0,m}\right|^2}. \tag{6.30}$$

In figure 6.2 we have plotted some of these overlaps. For large enough numbers of lattice sites, those dipole subspaces that are close to the dipole vacuum have the property that the overlaps are small. However, for dipole subspaces far from the dipole vacuum (e.g. $M = \lfloor N/2 \rfloor$), these overlaps are not small and in fact are never zero. This means that if we evolve long enough so that these large dipole-number subspaces get populated, then we cannot simplify the Hamiltonian. We note that this is a qualitative argument, and a rigorous, quantitative argument for this approximation requires appealing to second-order perturbation theory or the variational principle.

For short times, the only states relevant to the dynamics are the states $|M_0\rangle$. The hopping Hamiltonians become

$$\hat{H}_J^{(M\to M+1)} = -J(M+1)\sqrt{2}\sqrt{\frac{n_{M+1}}{n_M}}|(M+1)_0\rangle\langle M_0|. \tag{6.31}$$

The effective tunneling parameter is given by

$$J^{(M\to M+1)} = J(M+1)\sqrt{2}\sqrt{\frac{n_{M+1}}{n_M}} = J\sqrt{2}\sqrt{\frac{(M+1)(N-2M)(N-2M-1)}{(N-M)}}. \tag{6.32}$$

The size of this reduced Hilbert space is $\lfloor N/2 \rfloor + 1$, which scales as the number of sites, $N$. This is a huge reduction over the full Hamiltonian and even over the dipole Hamiltonian derived in the previous section.

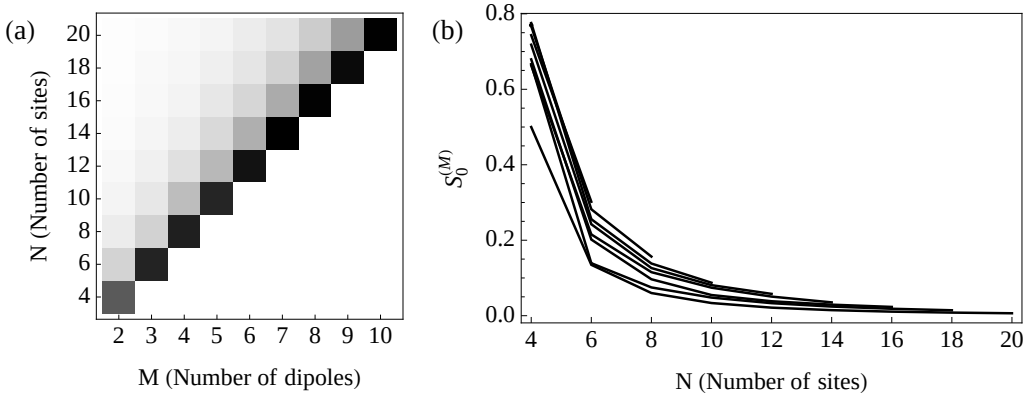


Figure 6.2: Overlaps $S_0^{(M)}$ in the $M$-dipole subspace. (a) As the number of sites is increased in a fixed dipole subspace, the total overlap decreases, indicating that the extra states, $|M;\psi_{m\neq 0}\rangle$ become more irrelevant. (b) The overlaps tend towards zero as long as $M \lesssim N/4$.

### 6.1.3 Validity of the approximations

In this section, we investigate the general dynamics in various parameter regimes. We have two main goals: (a) to determine when the approximate Hamiltonians generated in the previous sections are useful, and (b) to determine the large-$N$ behavior of the system.

#### 6.1.3.1 Comparison of full basis and dipole basis dynamics

We first determine how well the dynamics are approximated using only states in the dipole subspace. To do this, we vary the interaction strength $U$ at a fixed number of sites $N = 6$. Taking the initial state to be the unit-filled state, we evolve the system for a time $\Delta t = 2000\hbar/E_R$. The lattice depth is $V_0 = -15E_R$, corresponding to a hopping energy of $J = 0.0065E_R$, so that $\Delta t \approx 13\hbar/J$. We are therefore evolving over timescales relevant to the atomic dynamics. The interaction strength $U$ takes on values $5J$, $10J$, $20J$, and $70J$. We consider the exactly resonant case, $\hbar\omega_B = U$.

In figure 6.3, we plot the total population $P_D$ in the dipole subspace as a function of time using the full Hilbert space of 6 atoms in 6 sites. As the interaction strength is increased from $5J$ to $70J$, $P_D$ saturates at 1, indicating that the bulk of the atomic dynamics is occurring within the dipole subspaces once the interaction strength is large enough. This is consistent with the discussion in previous sections.

However, as we can see from figure 6.4, the population in the dipole subspaces decreases with the number of sites at a fixed $U$; in this figure, $P_D$ is plotted for $N = 2$, 3, 4, 5, and 6 at $U = 20J$. Apparently, there is a lattice-size dependence in the dynamics. In making the dipole approximation, it is not enough to stipulate $U \gg J$. Equation 6.32 suggests that the proper condition is $U \gg J\sqrt{N}$, although this may not be enough if higher dipole subspaces get populated.

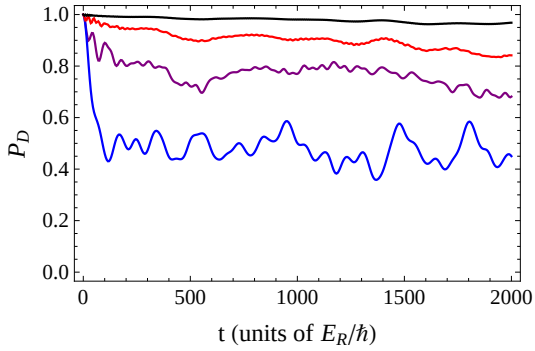


Figure 6.3: Total population $P_D$ of the dipole subspaces for a six-site lattice computed using the full-basis Hamiltonian. As the interaction strength is increased from $U = 5J$ (blue) through $U = 10J$ (purple) and $U = 20J$ (red) to $U = 70J$ (black), this population saturates at 1, indicating that the dynamics occur mainly within the dipole subspaces.

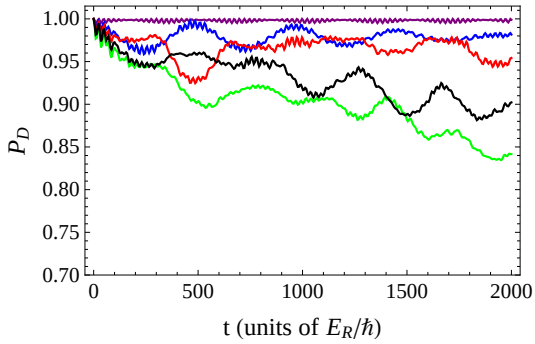


Figure 6.4: Total population $P_D$ of the dipole subspaces for an interaction strength of $U = 20J$ computed using the full-basis Hamiltonian. As the number of sites is increased from $N = 2$ (purple) through $N = 3$ (blue), $N = 4$ (red), and $N = 5$ (black) to $N = 6$ (green), this population decreases, indicating that there is the dynamics depend in some non-trivial way on the system size.

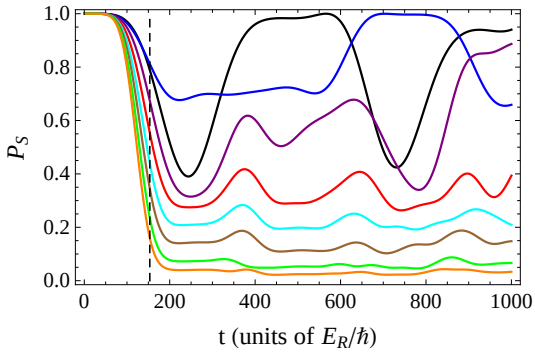


Figure 6.5: Total population $P_S$ in the symmetric states as a function of time as computed with the dipole subspace Hamiltonian. The lattice size is varied, taking on values of $N = 4$, 5, 6, 8, 10, 12, 15, and 18 sites. As the lattice size is increased, the symmetric Hamiltonian approximation gets worse. The timescale over which non-symmetric states get populated is given by $\hbar/J$, indicated as a vertical dashed line.

#### 6.1.3.2 Comparison of dipole basis and symmetric basis dynamics

The situation is not as promising for the symmetric Hamiltonian. In figure 6.5, we plot the total symmetric-state population at $U = \hbar\omega_B$ for lattice sizes ranging from $N = 4$ to $N = 18$ using the dipole subspace Hamiltonian. The approximation that the dynamics occur within the symmetric subspace is good only for times $t \ll \hbar/J$; this timescale is indicated as a vertical dashed line in the figure. For lattice sizes $N \geq 18$ and times greater than $t > \hbar/J$, the atomic dynamics occur entirely outside the symmetric subspace. For this reason, the symmetric approximation made in the previous section is not a good one. However, there is evidence that such an approximation works in a dilute gas, i.e. one where the number of atoms is much smaller than the number of lattice sites [110].

#### 6.1.3.3 Two-state dynamics for $|U - \hbar\omega_B| \gg J$

There is one special case where the symmetric Hamiltonian is a good approximation for the atomic system. When $|U - \hbar\omega_B| \gg J$, the coupling of the unit-filled state $|\psi_{\mathrm{MI}}\rangle$ to dipole subspaces beyond $M = 1$ scales as $J^2/|U - \hbar\omega_B| \ll J$. The system then

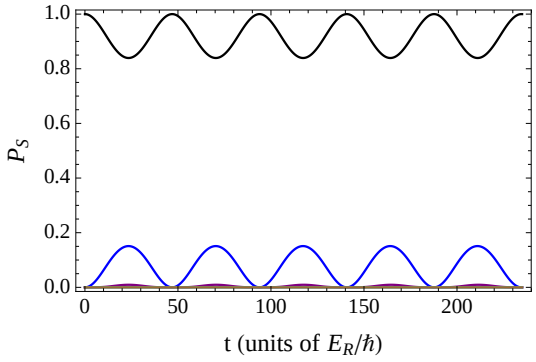


Figure 6.6: Population in the symmetric states as a function of time for $|U - \hbar\omega_B| \gg J$ computed using the dipole subspace Hamiltonian. The system undergoes off-resonant Rabi-type oscillations between the unit-filled state (black) and the symmetric one-dipole state (blue). Other symmetric dipole states get negligibly populated. Parameters here are $N = 10$, $U = 100J$, $J \approx 0.0065E_R$, and $\hbar\omega = U - 20J$.

reduces to a two state system with Hamiltonian,

$$\hat{H}_2 = (U - \hbar\omega_B)|1\rangle\langle 1| - J\sqrt{2(N-1)}(|1\rangle\langle 0| + |0\rangle\langle 1|), \tag{6.33}$$

and the system displays Rabi-like oscillations between the unit-filled state and the symmetric one-dipole state. These dynamics are particularly simple, and we therefore consider them below in the discussion of the optical detection of the atomic motion in this system. An example of these dynamics is plotted in figure 6.6. The general dynamics of this system is left for future work.

## 6.2 Detection Scheme

In order to optically probe the atomic dynamics just discussed, we place the system inside an optical cavity that supports two counter-propagating running-wave modes. We pump one of the two cavity modes, and photons from this mode scatter off the atoms into the second mode. A heterodyne detection scheme at the cavity output allows us to measure the dynamics of the amplitude of the probe field. From this measurement, we can infer certain characteristics of the atomic motion.

The Hamiltonians for the bare cavity modes and the cavity-atom interaction are given by

$$\hat{H}_{\mathrm{C}} = \hbar\omega\hat{N}_{\mathrm{C}} + \hbar\eta(\hat{a}^{\dagger}_{k_{\mathrm{C}}} + \hat{a}_{k_{\mathrm{C}}}), \tag{6.34}$$

$$\hat{H}_{\mathrm{A/C}} = \hbar g_0 \hat{N}_{\mathrm{A}}\hat{N}_{\mathrm{C}} + \hbar g_0 \int dz\ \hat{\Psi}^{\dagger}(z)\left(\hat{a}^{\dagger}_{k_{\mathrm{C}}}\hat{a}_{-k_{\mathrm{C}}}e^{-i2k_{\mathrm{C}}z} + \hat{a}^{\dagger}_{-k_{\mathrm{C}}}\hat{a}_{k_{\mathrm{C}}}e^{i2k_{\mathrm{C}}z}\right)\hat{\Psi}(z), \tag{6.35}$$

where

$$\hat{N}_{\mathrm{A}} = \int dz \hat{\Psi}^{\dagger}(z)\hat{\Psi}(z), \tag{6.36}$$

$$\hat{N}_{\mathrm{C}} = \hat{a}^{\dagger}_{k_{\mathrm{C}}}\hat{a}_{k_{\mathrm{C}}} + \hat{a}^{\dagger}_{-k_{\mathrm{C}}}\hat{a}_{-k_{\mathrm{C}}}, \tag{6.37}$$

are the total number of atoms and total number of photons, respectively. Decay of the cavity modes out of the cavity is given by the Liouvillian,

$$\hat{\mathcal{L}}\hat{\rho} = -\frac{\hbar\kappa}{2}\sum_{k=\pm k_{\mathrm{C}}}\left(\hat{a}^{\dagger}_{k}\hat{a}_{k}\hat{\rho} + \hat{\rho}\hat{a}^{\dagger}_{k}\hat{a}_{k} - 2\hat{a}_{k}\hat{\rho}\hat{a}^{\dagger}_{k}\right). \tag{6.38}$$

If we assume that the number of photons in both modes is small enough, we can assume that the atomic dynamics is unaffected by the presence of the cavity. In particular, no interband transitions are induced by the presence of photons in the cavity. In this case, we can expand $\hat{H}_{\mathrm{A/C}}$ in the Wannier functions from the previous section, resulting in

$$\hat{H}_{\mathrm{A/C}} = \hbar g_0 \hat{N}_{\mathrm{A}}\hat{N}_{\mathrm{C}} + \hbar g_0 \sum_{j',j}\hat{b}^{\dagger}_{j'}\hat{b}_{j}\hat{a}^{\dagger}_{-k_{\mathrm{C}}}\hat{a}_{k_{\mathrm{C}}}f_{j',j}(2k_{\mathrm{C}}) + \mathrm{H.c.}, \tag{6.39}$$

where

$$f_{j',j}(k) = \int dz\ w^{*}(z - z_{j'})e^{ikz}w(z - z_{j}). \tag{6.40}$$

Taking

$$2k_{\mathrm{C}} = 2nk_{\mathrm{L}} + q_0, \tag{6.41a}$$

$$0 \leq q_0 \leq 2k_{\mathrm{L}}, \tag{6.41b}$$

$$n \in \mathbb{Z}, \tag{6.41c}$$

the single-particle matrix element becomes

$$f_{j',j}(2k_{\mathrm{C}}) = e^{-iq_0 j' d}\frac{1}{N}\sum_q e^{iq(j-j')d}\int dz\ \psi^*_{q+q_0}(z)e^{i2nk_{\mathrm{L}}z}\left(e^{iq_0 z}\psi_q(z)\right), \tag{6.42}$$

since $e^{iq_0 z}$ has a well-defined quasi-momentum as a sum over Bloch states with the same quasi-momentum. We define

$$I_q^{(n)}(q_0) = \int dz\ \psi^*_{q+q_0}(z)e^{i2nk_{\mathrm{L}}z}\left(e^{iq_0 z}\psi_q(z)\right). \tag{6.43}$$

If we restrict our attention only to the dipole subspaces, then the only terms that survive in $\hat{H}_{\mathrm{A/C}}$ are those involving $\hat{b}_j^\dagger\hat{b}_j$ and $\hat{b}_j^\dagger\hat{b}_{j\pm1}$. In this case, the interaction Hamiltonian is

$$\begin{aligned}\hat{H}_{\mathrm{A/C}} = {}& \hbar g_0\hat{N}_{\mathrm{A}}\hat{N}_{\mathrm{C}} + \hat{a}^\dagger_{-k_{\mathrm{C}}}\hat{a}_{k_{\mathrm{C}}}\hbar g_0\left(\frac{1}{N}\sum_q I_q^{(n)}(q_0)\right)\sum_j \hat{b}_j^\dagger\hat{b}_j e^{-iq_0 jd} + \mathrm{H.c.}\\ &+ \hat{a}^\dagger_{-k_{\mathrm{C}}}\hat{a}_{k_{\mathrm{C}}}\hbar g_0\left(e^{-iq_0 d}\frac{1}{N}\sum_q I_q^{(n)}(q_0)e^{-iqd}\right)\sum_j \hat{b}_{j+1}^\dagger\hat{b}_j e^{-iq_0 jd} + \mathrm{H.c.}\\ &+ \hat{a}^\dagger_{-k_{\mathrm{C}}}\hat{a}_{k_{\mathrm{C}}}\hbar g_0\left(e^{iq_0 d}\frac{1}{N}\sum_q I_q^{(n)}(q_0)e^{iqd}\right)\sum_j \hat{b}_{j-1}^\dagger\hat{b}_j e^{iq_0 jd} + \mathrm{H.c.}\end{aligned} \tag{6.44}$$

This shows us that the plane-wave index $n$ is irrelevant to the extent that the dependence on $n$ is absorbed into the coupling constants. It may make a difference in the relative strength of the two terms, but it is clear that the $q_0$ is the more important quantity. For this reason, we set $n = 0$ in what directly follows and take $I_q(q_0) = I_q^{(0)}(q_0)$. In figure 6.7, we plot the absolute value of the single-particle matrix elements, $f_{0,0}(q_0)$ and $f_{1,0}(q_0)$ as a function of quasi-momentum for different lattice depths. As the lattice depth is increased, $|f_{0,0}|$ increases and $|f_{1,0}|$ decreases. In addition, $|f_{0,0}| \approx 1$ across all quasi-momenta, whereas $|f_{1,0}| = 0$ at $q_0 = \pi/d$. For this reason, we choose $q_0 = \pi/d$ so that the second and third terms in equation (6.44) are zero, and the probe field is sensitive only to the site-numbers. In this way, the signal depends explicitly on the dipole subspace in which the dynamics is occurring.

With the balanced heterodyne detection outlined in the previous chapter, we can detect the cavity field amplitude proportional to $\langle\hat{a}_{-k_{\mathrm{C}}}\rangle$. In order to determine what

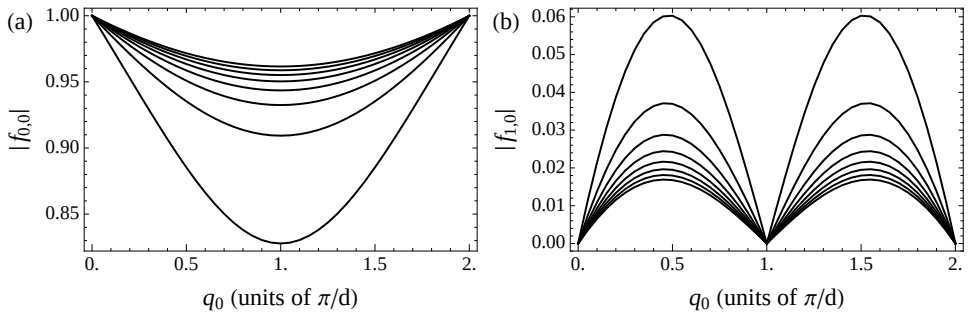


Figure 6.7: Hubbard model coupling parameters $f_{i,j}(q_0)$ for the detection scheme plotted as a function of quasi-momentum. (a) The diagonal coupling $f_{0,0}$ increases as a function of lattice depth $V_0$ and is roughly constant across quasi-momenta. (b) The next-to-nearest-neighbor coupling $f_{1,0}$ decreases with lattice depth and is exactly zero at $q_0 = \pi/d$.

properties of the atomic motion this will measure, we compute the equations of motion for $\langle \hat{a}_{\pm k_{\rm C}} \rangle$. They are

$$i\frac{d\langle \hat{a}_{-k_{\rm C}} \rangle}{dt} = \left(\delta_p + g_0\langle \hat{N}_{\rm A} \rangle - i\frac{\kappa}{2}\right)\langle \hat{a}_{-k_{\rm C}} \rangle + g_0 f_{0,0}(q_0)\sum_j \langle \hat{a}_{k_{\rm C}} \hat{b}_j^\dagger \hat{b}_j \rangle e^{-iq_0 jd} \tag{6.45}$$

and

$$i\frac{d\langle \hat{a}_{k_{\rm C}} \rangle}{dt} = \left(\delta_p + g_0\langle \hat{N}_{\rm A} \rangle - i\frac{\kappa}{2}\right)\langle \hat{a}_{k_{\rm C}} \rangle + \eta + g_0 f_{0,0}(q_0)\sum_j \langle \hat{a}_{-k_{\rm C}} \hat{b}_j^\dagger \hat{b}_j \rangle e^{iq_0 jd} \tag{6.46}$$

Since the cavity linewidth is large, we can adiabatically slave $\langle \hat{a}_{k_{\rm C}} \rangle$ to the atomic motion, writing

$$\langle \hat{a}_{k_{\rm C}} \rangle \to \alpha = \frac{-\eta}{\delta_p + g_0\langle \hat{N}_{\rm A} \rangle - i\kappa/2}, \tag{6.47}$$

We have neglected the other terms because they are small compared to both $\kappa$ and $\langle \hat{N}_{\rm A} \rangle$. We can also adiabatically solve for $\langle \hat{a}_{-k_{\rm C}} \rangle$, resulting in

$$\langle \hat{a}_{-k_{\rm C}} \rangle = \frac{-\alpha g_0 f_{0,0}(q_0)}{\delta_p + g_0\langle \hat{N}_{\rm A} \rangle - i\kappa/2}\langle \hat{n}(q_0) \rangle, \tag{6.48}$$

where

$$\hat{n}(q_0) = \sum_j \langle \hat{b}_j^\dagger \hat{b}_j \rangle e^{-iq_0 jd}. \tag{6.49}$$

The last quantity is the one that tells us how the field amplitude reflects the atomic dynamics. In the next section, we explore the behavior of this expectation value for the various types of atomic states that show up in our approximations.

### 6.2.1 Dipole-subspace detection

We need to determine what sort of information about the atomic dynamics that detection of the field amplitude allows us access to. As a first step, we compute the expectation values, $\langle M; k_M, \ldots, k_1 | \hat{n}(\pi/d) | M; k_M, \ldots, k_1 \rangle$. All other expectation values vanish, since $|M; k_M, \ldots, k_1\rangle$ are site-number eigenstates. Abbreviating $|M; k_M, \ldots, k_1\rangle$

as $|M;\{k_i\}\rangle$, the matrix elements are

$$\begin{aligned}\langle M;\{k_i\}|\hat{n}(\pi/d)|M;\{k_i\}\rangle &= \sum_j \langle M;\{k_i\}|\hat{b}_j^\dagger \hat{b}_j|M;\{k_i\}\rangle e^{-ij\pi} \\ &= \sum_j \left(\sum_{n=1}^{M}(\delta_{j,k_n} - \delta_{j,k_n+1}) + 1\right) e^{-ij\pi} \\ &= 2\sum_{n=1}^{M}(-1)^{k_n} + \sum_j (-1)^j. \end{aligned} \tag{6.50}$$

The second term is clearly zero. The size of the first term depends on where the dipoles are, and it can range anywhere from 0 to $\pm 2M$. For instance, if $\{k_i\} = \{2,4,6,8\}$, then the first term is equal to $-8$, whereas if $\{k_i\} = \{1,4,7,10\}$, then it is equal to zero. This matrix element is sensitive to the distribution of dipoles within a dipole subspace.

In the context of the simplified two-state model of the previous section, we compute

$$\langle 1|\hat{n}(\pi/d)|1\rangle = \frac{1}{N-1} 2\sum_{j=1}^{N-1}(-1)^j = \frac{-2}{N-1}, \tag{6.51}$$

where we have assumed a lattice with an even number of sites. While this quantity differs from zero, which is the value of $\langle 0|\hat{n}(\pi/d)|0\rangle$, it decreases with the lattice size, indicating that the signal will not be very strong for large lattices. In figure 6.8, we have plotted $F$ from equation (6.49) as a function of time for the system described in figure 6.6. The field oscillates from 0, which indicates that the atoms are in the unit-filled states, to 0.0013, which is where the atoms are in a superposition of unit-filled and symmetric one-dipole states.

### 6.2.2 Conclusion

We have investigated a system comprised of strongly-interacting bosons confined in a tilted optical lattice. In the regime where the interaction strength is equal to the energy difference between adjacent lattice wells, the system dynamics take place in a restricted subspace that consists of so-called dipole states.

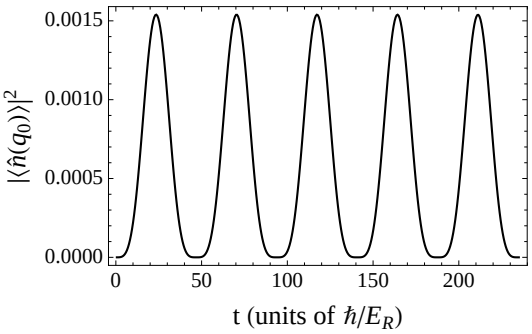


Figure 6.8: Time sequence for $|\langle\hat{n}(q_0)\rangle|^2$. The probe-field intensity is proportional to this quantity. The signal oscillates between 0 and 0.0015. The maximum value 0.0015 depends on the population of the symmetric one-dipole state.

We have also developed a method for measuring this atomic dynamics by coupling the atoms to two counter-propagating modes of an optical cavity. Pumping one mode strongly, we detect the light-field out-coupled through the cavity mirrors from the second mode. The center-of-mass motion is reflected in the dynamics of the probe field, as we demonstrate for one special case where the atomic motion consists of particles oscillating back and forth between adjacent wells.

The detection scheme is relatively insensitive to the dynamics in this special case, but there is a strong signal for dipole states far from the unit-filled state. One generalization of this measurement method is to measure higher-order correlations of the light-field, since they are coupled to higher-order correlation functions of the atoms such as $\langle \hat{n}_i \hat{n}_j \rangle$. These density-density correlations are sensitive to differences in particle number on different sites, and therefore this may be a better differentiator of the dipole states.

Eventually, this system might be utilized as a probe for more complicated many-body systems—for instance, those experiencing long-range interactions.

# Chapter 7

## Quantum Non-Demolition Measurement of the Photon Number in a Cavity

Up to this point, we have been interested in the properties of single- and many-particle atomic systems and how these properties might be experimentally probed with light. In the final chapter of this thesis, we reverse our focus and examine a cavity QED system in which atoms may be used to probe the state of the light field. In this case, we perform a quantum nondemolition (QND) measurement of the cavity photon number by measuring the internal state of an atom dispersively coupled to a single mode of the cavity. Besides providing tests of fundamental principles such as quantum measurement theory, this setup allows for a simple method of preparing non-classical states of light such number states. These states are important in precision metrology applications where the goal is to beat the standard quantum limit of measurement uncertainty [55, 83].

We imagine an experiment where a cloud of two-level atoms are subjected to a $\pi/2$-pulse. The ground state atoms are split off and allowed to evolve freely, whereas the excited state atoms are allowed to interact with a single standing-wave mode of a far-detuned optical resonator. We operate in the Bragg regime where the recoil energy of the atom during absorption and re-emission of a photon is much larger than the interaction strength. This restricts the dynamics to two center-of-mass states undergoing Rabi-like oscillations with a photon-number dependent frequency. The excited and ground state

atoms are recombined and subjected to a second $\pi/2$-pulse. The population inversion of each atom is measured, and the photon number is inferred using a Bayesian method.

A similar scheme was proposed for making QND measurements of the photon number by measuring the momentum distribution of atoms sent through a cavity [56]. This system operated in the Raman-Nath regime [88] where many Bragg peaks appear in the atomic momentum distribution. This requires that the atom-field interaction time must be much smaller than the inverse recoil frequency.

Our scheme is also closely connected to the microwave cavity QND measurements performed in the group of Raimond and Haroche [50]. In these experiments, Rydberg atoms are sent through a high finesse cavity. The recoil imparted to the atom during absorption or emission of a microwave photon is negligible in these situations. In addition, the interaction is such that the population inversion of the atoms is unchanged. The relative phase between excited and ground state changes with a frequency dependent on the number of photons in the cavity, and Ramsey interferometry at the cavity output allows to infer the photon number in the cavity.

Quantum non-demolition measurements have in general been applied to high-fidelity readout of ionic qubit states [59], to probing of Rabi oscillations in cesium clocks [26, 131], and to proposals for atomic state preparation in ultracold gases [87].

## 7.1 Ramsey Interferometry in the Bragg Regime

For the purposes of this QND measurement scheme, we need the probability that an atom is in the excited state given there are $n$ photons in the cavity. The Hamiltonian describing the interaction of a single two-level atom with one quantized standing-wave mode of a linear cavity and a classical clock laser is

$$\begin{aligned}\hat{H} = &\frac{\hbar\delta}{2}\hat{\sigma}^z + \frac{1}{2m}\hat{P}^2 + \hbar\omega\hat{a}^\dagger\hat{a} \\ &+ 2\hbar g\ \hat{a}^\dagger\hat{a}\cos^2(k_{\mathrm{C}}\hat{z}) + \frac{\hbar\Omega}{2}\left(\hat{\sigma}^+ e^{ik_{\mathrm{L}}\hat{x}} + \hat{\sigma}^- e^{-ik_{\mathrm{L}}\hat{x}}\right),\end{aligned} \tag{7.1}$$

where $\hat{P}$ is the center-of-mass momentum of the atom, $\delta$ is the detuning between the clock laser frequency and the atomic transition frequency, and $k_{\mathrm{L}}$ is the clock-laser wave vector. We work in the basis where $\hat{\sigma}^z$, $\hat{P}$, and $\hat{a}^\dagger\hat{a}$ are diagonal,

$$|\sigma, p, n\rangle = |\sigma\rangle|p\rangle|n\rangle, \tag{7.2a}$$

$$\hat{P}|p\rangle = \hbar p|p\rangle, \tag{7.2b}$$

$$\hat{a}^\dagger\hat{a}|n\rangle = n|n\rangle, \tag{7.2c}$$

$$\hat{\sigma}^z|\sigma\rangle = (\delta_{e,\sigma} - \delta_{g,\sigma})|\sigma\rangle. \tag{7.2d}$$

The matrix elements of the Hamiltonian sans the clock-pulse are

$$\hat{H}^{(n)}_{pp'} = \delta_{pp'}\left(\frac{\hbar^2 p^2}{2m} + \hbar(g+\omega)n\right) + \frac{\hbar g n}{2}\left(\delta_{p',p+2k_{\mathrm{C}}} + \delta_{p',p-2k_{\mathrm{C}}}\right), \tag{7.3}$$

where we have left out reference to the internal degrees of freedom.

According to the experiment envisioned above, the initial state of the system is

$$|\psi_i\rangle = |g, 0, n\rangle. \tag{7.4}$$

A $\pi/2$-pulse is applied to this state, resulting in

$$|\psi(0)\rangle = \frac{1}{\sqrt{2}}|n\rangle(|0\rangle|g\rangle + |k_{\mathrm{L}}\rangle|e\rangle). \tag{7.5}$$

The ground state is allowed to evolve freely for a time $t$, resulting in

$$|\psi_g(t)\rangle = e^{i\delta t/2}e^{-in(g+\omega)t}|0\rangle|g\rangle|n\rangle. \tag{7.6}$$

On the other hand, the excited state atom interacts with the cavity field. We separate out the free time-dependence of this state and expand in plane-wave modes as

$$|\psi_e(t)\rangle = e^{-i\delta t/2}e^{-in(g+\omega)t}|n\rangle|e\rangle\sum_p C_p(t)|p\rangle, \tag{7.7}$$

$$C_p(0) = \delta_{p,k_{\mathrm{L}}}. \tag{7.8}$$

The equation of motion for the coefficient $C_p$ is given by

$$i\dot{C}_p = \frac{\hbar}{2m}p^2 C_p + \frac{ng}{2}\left(C_{p+2k_{\mathrm{C}}} + C_{p-2k_{\mathrm{C}}}\right). \tag{7.9}$$

In particular, the initial state $C_{k_\mathrm{L}}$ couples directly to $C_{k_\mathrm{L}\pm 2k_\mathrm{C}}$. If we consider a near-resonant clock-pulse, i.e. $k_\mathrm{L} \approx k_\mathrm{C}$, and we assume $ng \ll \hbar k_\mathrm{C}^2/2m$—the condition for being in the Bragg regime—then we need only consider two states, $C_{k_\mathrm{L}}$ and $C_{k_\mathrm{L}-2k_\mathrm{C}}$. We then have the effective Hamiltonian,

$$H_\mathrm{eff} = \hbar \begin{bmatrix} k_\mathrm{L}^2\hbar/2m & ng/2 \\ ng/2 & (k_\mathrm{L}-2k_\mathrm{C})^2\hbar/2m \end{bmatrix}, \tag{7.10}$$

in the basis $\{|k_\mathrm{L}\rangle, |k_\mathrm{L}-2k_\mathrm{C}\rangle\}$.

After evolving the initial state for a time $t$ under this Hamiltonian, the state is given by

$$\begin{aligned} |\psi(t)\rangle = &\frac{1}{\sqrt{2}} e^{i\delta t/2} e^{-in(g+\omega)t} |g\rangle|n\rangle|0\rangle \\ &+ \frac{1}{\sqrt{2}} e^{-i\delta t/2} e^{-in(g+\omega)t} |n\rangle|e\rangle \left( C_{k_\mathrm{L}}(t)|k_\mathrm{L}\rangle + C_{k_\mathrm{L}-2k_\mathrm{C}}(t)|k_\mathrm{L}-2k_\mathrm{C}\rangle \right), \end{aligned} \tag{7.11}$$

where, given the initial condition $C_p(0) = \delta_{p,k_\mathrm{L}}$,

$$C_{k_\mathrm{L}}(t) = e^{-i\Phi t}\left( \cos\left(\frac{\Omega}{2}t\right) - i\frac{\Delta}{\Omega}\sin\left(\frac{\Omega}{2}t\right)\right), \tag{7.12}$$

$$C_{k_\mathrm{L}-2k_\mathrm{C}}(t) = e^{-i\Phi t}\frac{-iV}{\Omega}\sin\left(\frac{\Omega}{2}t\right). \tag{7.13}$$

The parameters in these expressions are

$$\Phi = \frac{\hbar}{4m}(k_\mathrm{L}^2 + (k_\mathrm{L}-2k_\mathrm{C})^2), \tag{7.14a}$$

$$\Delta = \frac{\hbar}{2m}(k_\mathrm{L}^2 - (k_\mathrm{L}-2k_\mathrm{C})^2), \tag{7.14b}$$

$$V = ng, \tag{7.14c}$$

$$\Omega = \sqrt{V^2+\Delta^2}. \tag{7.14d}$$

We perform a second $\pi/2$-pulse and compute the population of the excited state at time $t$; it is

$$P(e|n)(t) = \frac{1}{2} - \frac{1}{2}\cos((\delta+\Phi)t)\cos\left(\frac{\Omega t}{2}\right) + \frac{1}{2}\frac{\Delta}{\Omega}\sin((\delta+\Phi)t)\sin\left(\frac{\Omega t}{2}\right). \tag{7.15}$$

The conditions that this formula is correct were given above as $k_{\mathrm{L}} \approx k_{\mathrm{C}}$ and $ng \ll \hbar k_{\mathrm{C}}^2/2m$. We can make these conditions more exact by noting that we want $|k_{\mathrm{L}}\rangle$ to connect to $|k_{\mathrm{L}} - 2k_{\mathrm{C}}\rangle$ but not to $|k_{\mathrm{L}} + 2k_{\mathrm{C}}\rangle$. The coupling constants between these states are given by

$$g_{k_{\mathrm{L}} \pm 2k_{\mathrm{C}}} \sim \frac{2m}{\hbar} \frac{(gn)^2}{(k_{\mathrm{L}} \pm 2k_{\mathrm{C}})^2 - k_{\mathrm{L}}^2} = \frac{m}{2\hbar} \frac{1}{k_{\mathrm{C}}} \frac{(gn)^2}{k_{\mathrm{C}} \pm k_{\mathrm{L}}}. \tag{7.16}$$

As long as $gn \ll 2\hbar k_{\mathrm{C}}(k_{\mathrm{C}} + k_{\mathrm{L}})/m$, then the coupling to $|k_{\mathrm{L}} + 2k_{\mathrm{C}}\rangle$ is negligible. This limits the width of the momentum distribution of the initial ground-state atomic gas along the axis of the cavity.

For simplicity, we set $\delta = -\Phi$, resulting in

$$P(e|n)(t) = \frac{1}{2} - \frac{1}{2} \cos\left( \frac{\omega_R t}{2} \sqrt{\left(\frac{ng}{\omega_R}\right)^2 + 16\left(\frac{k_{\mathrm{C}} - k_{\mathrm{L}}}{k_{\mathrm{C}}}\right)^2} \right), \tag{7.17}$$

where $\omega_R = E_R/\hbar$ is the recoil angular frequency of the cavity field. If the initial ground-state gas of atoms has a momentum distribution $\psi(\hbar p)$ along the axis of the cavity, then we replace $k_{\mathrm{L}}$ with $p + k_{\mathrm{L}}$ in the expression for $P(e|n)(t)$ and integrate it against $|\psi(\hbar p)|^2$.

## 7.2 Bayesian Analysis

The Bayes theorem for conditional probabilities,

$$P(A|B) = \frac{P(A)P(B|A)}{P(B)}, \tag{7.18}$$

states that the conditional probability of $A$ occurring given that $B$ occurred is equal to the probability that $A$ occurs times the conditional probability that $B$ occurs given $A$, up to a normalization. Here, we take $A$ to be the number of cavity photons $n$ and $B$ to be the internal state of the atom $\sigma$, which can be either $e$ or $g$. The quantity $P(\sigma|n)$ is called the forward distribution, $P(n|\sigma)$ is called the updated distribution, and $P(n)$ is called the prior distribution and represents our current state of knowledge before the

next measurement. As measurements are made, our knowledge about the state of the cavity system is updated, as follows.

We assume that we have some prior knowledge of the distribution $P_0(n)$ of photons in the cavity before any measurements are made. This distribution might be a coherent state, reflecting our knowledge of the initial cavity system setup, or it might be a uniform distribution, reflecting our knowledge that the number of photons in the cavity is less than some number $M$. After a single measurement $\sigma_1$ of the internal state of the atom, our knowledge is updated via Bayes theorem as

$$P(n|\sigma_1) = \mathcal{N}_1 P_0(n) P(\sigma_1|n), \tag{7.19}$$

where $\mathcal{N}_1$ is a normalization. If we make $N$ measurements, obtaining the measurement record,

$$\text{REC} = \{\sigma_1, \sigma_2, \ldots, \sigma_N\}, \tag{7.20}$$

then the updated probability distribution for having $n$ photons given this record is given by

$$P(n|\text{REC}) = \mathcal{N}_N P_0(n) \prod_{j=1}^{N} P(\sigma_j|n). \tag{7.21}$$

The final state of the field is a number state since $P(n|\text{REC})$ is expected to limit to some $\delta_{n,n_f}$.

This is the standard Bayes prescription for making a series of measurements to determine a probability distribution, and it coincides with our understanding of the square of the wave-function (or the diagonal elements of the density matrix) being a probability distribution. However, quantum mechanics deals in probability amplitudes first and foremost, and it turns out that there is a quantum Bayes theorem for these amplitudes [25, 44]. Here, since we are dealing with a QND measurement—i.e. the measurement of the internal state of the atom does not alter the photon number—the coherences between different photon number states do not affect the atom-field

interaction. We can therefore neglect them, allowing us to work with the probabilities directly rather than the probability amplitudes.

### 7.2.1 Measurement protocols

In the expression for the forward distribution $P(e|n)(t)$, the time of interaction $t$ is to this point unspecified. This is intentional, as it determines how fast the Bayesian inference method converges. To see that this is so, we consider the case where we know that there are either zero or one photons in the cavity. For simplicity, we assume $k_{\mathrm{C}} = k_{\mathrm{L}}$. If we choose $t = 4\pi/g$, then $P(e|0)(t) = P(e|1)(t) = 1$. The forward distribution then does not distinguish between the 0 and 1 photon states. In particular, the updated prior does not change.

Intuitively, what we want is that the prior "maximally changes" when it is updated. One way to achieve this is to have the largest spread in possible values, $P(e|n)(t)$. The smallest time for which this happens is given by $\tau = 2\pi/n_{\max}|g|$, where $n_{\max}$ is the maximum number of photons in the cavity based on our prior knowledge of the system. In figure 7.1(a), we have plotted the time-dependence of $P(e|n)$ for $n = 0$ to $n = 10$. The probabilities achieve a maximum spread, varying between 0 and 1, at exactly $\tau = 2\pi/10|g|$, as can be seen more readily in figure 7.1(b).

According to this measurement protocol, each atom interacts with the cavity modes for a time $\tau = 2\pi/n_{\max}|g|$. This is particularly simple, and it seems that we have gained by the fact that the interaction time is very small. However, there are other protocols that promise to converge faster than this simple one.

We can see this by investigating figure 7.2. In figure 7.2(a), we have extended the $P(e|n)$ time sequences out to $t = 2\pi/|g|$. At this time, we can see that the $P(e|n)$ is zero for half of the photon numbers and 1 for the rest (see black curve in 7.2(b)). This means that if a measurement is made after an atom is allowed to interact for this amount of time, then the probabilities for half of the photon numbers are automatically

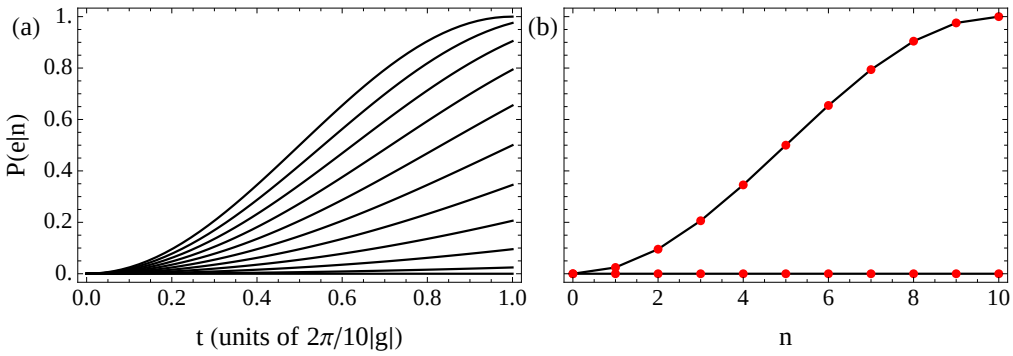


Figure 7.1: Forward probability distribution $P(e|n)$ for the first measurement protocol. (a) The forwards for $n = 0$ to $n = 10$ are plotted for interaction times from $t = 0$ to $t = 2\pi/10|g|$. (b) The probabilities at $t = 2\pi/10|g|$ span the entire range from 0 to 1.

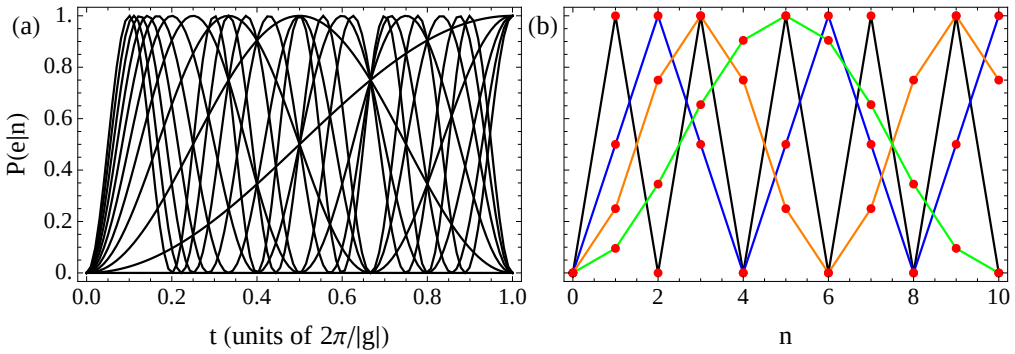


Figure 7.2: Forward probability distribution $P(e|n)$ for the first optimized protocol. (a) The forwards for $n = 0$ to $n = 10$ are plotted for interaction times from $t = 0$ to $t = 2\pi/|g|$. (b) The probabilities at $\tau = 2\pi/|g|$ (black), $\tau = 2\pi/2|g|$ (blue), and $\tau = 2\pi/3|g|$ (orange) are each partitioned into sets of photon numbers where the probabilities are zero or one.

set to zero. This contrasts with measurements made in the previous protocol, where in any measurement, only $n = 0$ and $n = n_{\max}$ can be set to zero. This promises to speed up the convergence process.

We generalize this by noting that there are many times in figure 7.2(a) for which the photon numbers are partitioned into sets where $P(e|n) = 0$, $P(e|n) = 1$, and $0 \neq P(e|n) \neq 1$. Some examples—$\tau = 2\pi/|g|$ (black), $\tau = 2\pi/2|g|$ (blue), $\tau = 2\pi/3|g|$ (orange), and $\tau = 2\pi/5|g|$ (green)—are shown in figure 7.2(b).

Based on these considerations, we adopt the following measurement protocol. Each atom interacts with the cavity mode for a different amount of time. In order, these are

- $\tau = 2\pi/n|g|$, where $n < n_{\max}$ is prime.
- $\tau = 2\pi/n^2|g|$, where $n$ is prime and $n^2 < n_{\max}$ $\cdots$
- $\cdots$ $\tau = 2\pi/n^k|g|$; $k$ is the maximum power for which there is an $n$ such that $n$ is prime and satisfies $n^k < n_{\max}$.
- $\tau = 2\pi/n_{\max}$ until the probability distribution is converged.

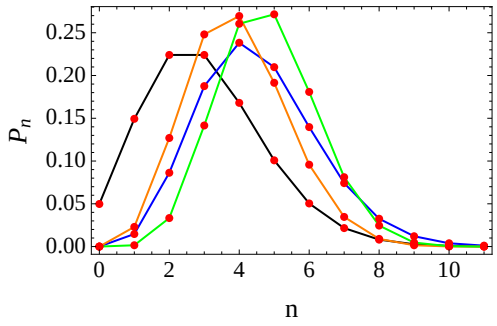


Figure 7.3: A three-measurement Bayesian sequence starting with a coherent state of mean 3 (black). In the first measurement, the result is that the atom is in the excited state; the initial distribution is multiplied by the forward distribution $P(e|n)$ (blue). The second measurement yields $|g\rangle$, so the updated distribution is multiplied by $P(g|n)$ (orange). Finally, the third measurement yields $|e\rangle$, so the updated distribution is multiplied by $P(e|n)$ (green).

This measurement scheme can be applied to prepare a number state of the cavity or to perform tomography on an initial photon number distribution.

## 7.3 Results

In figure 7.3, four photon-number distributions are plotted. The black curve is an initial coherent state distribution with mean 3. The next three curves are the distributions after successive measurements. Here, the measurement record is REC = $\{e, g, e\}$, and therefore the initial distribution gets multiplied first by the distribution in 7.1(b), then by one minus this distribution, and finally by the distribution again. We can already see how the distribution is narrowing.

In figure 7.4, we show three examples of Bayesian measurement sequences starting from the coherent state distribution with mean 3. These distributions are clearly converging to different photon numbers, nine, three, and two, respectively. It is also clear that the convergence is not very fast. That is, even 200 measurements are not enough to converge two of these distributions.

In figures 7.5 and 7.6, we illustrate similar results as in figures 7.3 and 7.4 except

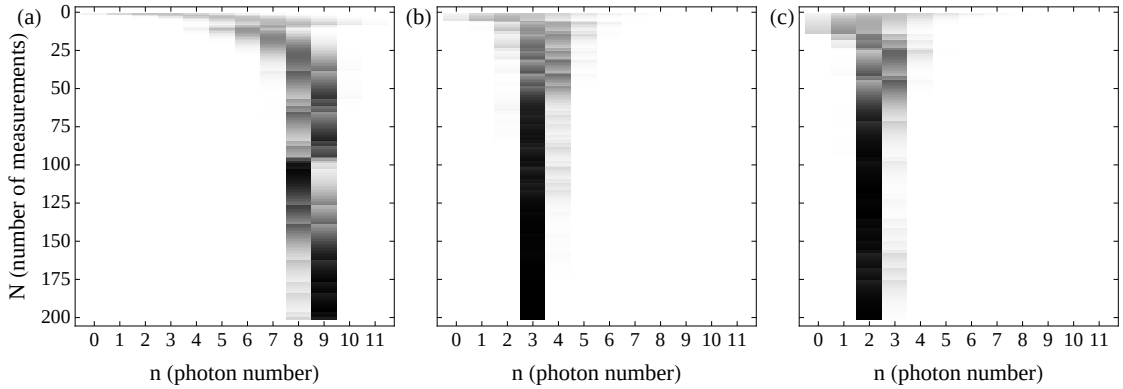


Figure 7.4: Three 200-step Bayesian measurement sequences starting with a coherent state of mean $n = 3$. (a) The distribution seems to be converging to $n = 9$, but there is still significant population in other photon number states. (b) The distribution has converged to $n = 3$ after about 150 measurements. (c) The distribution is converging to $n = 2$.

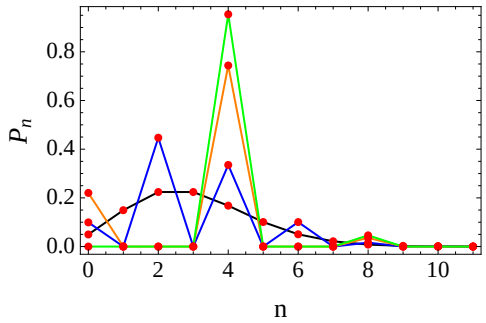


Figure 7.5: A three-measurement Bayesian sequence starting with a coherent state of mean 3 (black). Here, the second measurement protocol is used. After the first measurement, all odd-number photon states have zero probability (blue). After the second measurement all photon numbers except for 0, 4, and 8 have zero probability (orange). Finally, after the third measurement, the zero-photon state has a zero probability, and the distribution seems to be converging to $n = 4$ (green). The forward distributions used here are illustrated in figure 7.2.

that the optimized measurement protocol is used. The distributions are converging an order of magnitude faster.

Finally, we perform tomography on an initial coherent state of mean $n = 3$. The optimized measurement protocol is used, with a total of 19 measurements made in each sequence. Five thousand sequences are run, and the converged results are collected and binned. The resulting distribution is essentially identical to the original distribution.

## 7.4 Experimental Considerations

We have discussed some of the conditions that need to be satisfied in order for this scheme to work. To reiterate, these conditions are $|k_{\mathrm{C}} - k_{\mathrm{L}}| \ll |k_{\mathrm{C}} + k_{\mathrm{L}}|$ and $gn \ll 2\hbar k_{\mathrm{C}}(k_{\mathrm{C}} + k_{\mathrm{L}})/m$. Assuming an initial atomic state with momentum $\hbar p$ and a resonant $\pi/2$-pulse, $k_{\mathrm{C}} \approx k_{\mathrm{L}}$, these conditions become $|p| \ll |p+2k_{\mathrm{C}}|$ and $gn \ll 4\hbar k_{\mathrm{C}}^2/m$. The essence of these conditions is that both the atom-field coupling and the width of the initial atomic momentum distribution along the axis of the cavity need to be much smaller than the recoil energy of the cavity field.

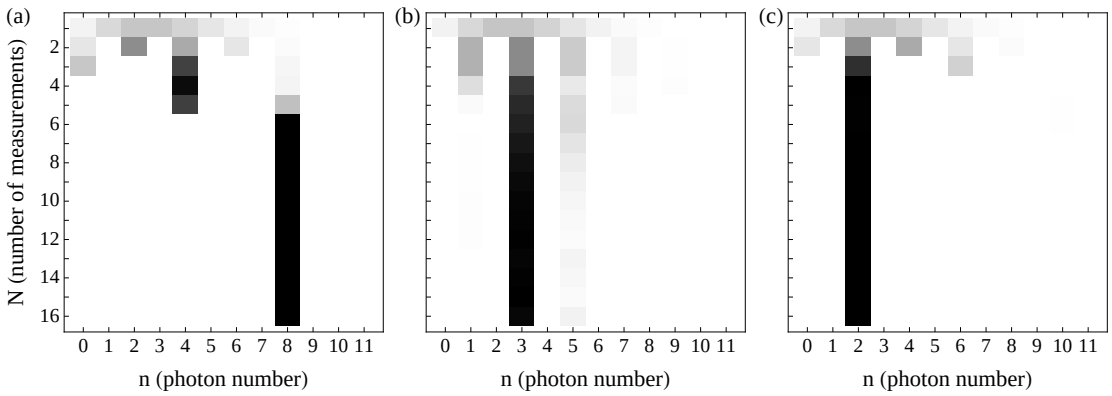


Figure 7.6: Three 200-step Bayesian measurement sequences starting with a coherent state of mean $n = 3$. Here, the second measurement protocol is used. (a) The distribution converged to $n = 8$ within 6 measurements. (b) The distribution is converging to $n = 3$ after 16 measurements. (c) The distribution converged to $n = 2$ after 4 measurements.

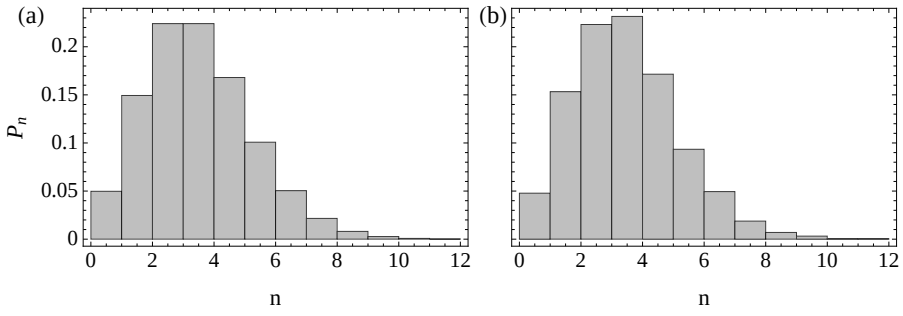


Figure 7.7: Reconstruction of the initial coherent state of mean 3 using the Bayesian measurement sequence. Here, the optimized protocol is used, where in each sequence 19 measurements are made. (a) The initial coherent state distribution. (b) The converged results of 5000 sequences are binned and plotted. This distribution reconstructs the original distribution.

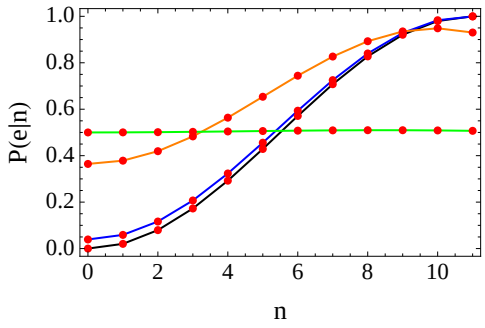


Figure 7.8: Forward distribution for various initial momentum distribution widths. We assume a Gaussian profile for the atomic momentum distribution and consider different widths, $\Delta p = 0$ (black), $\Delta p = 0.005 k_{\mathrm{C}}$ (blue), $\Delta p = 0.02 k_{\mathrm{C}}$ (orange), and $\Delta p = k_{\mathrm{C}}$ (green).

The width of the initial momentum distribution also affects the convergence of the Bayesian sequence. We can see this by assuming an initial Gaussian momentum distribution,

$$\psi(\hbar p) = \frac{1}{\pi^{1/4}\sqrt{\Delta p / k_{\mathrm{C}}}} e^{-p^2/2\Delta p^2}, \tag{7.22}$$

for the atoms and integrating the forward distribution—equation 7.17 with $k_{\mathrm{L}} \to p + k_{\mathrm{C}}$—against $|\psi(\hbar p)|^2$. In figure 7.8, the modified forward distribution is plotted for $\Delta p = 0$, $\Delta p = 0.005 k_{\mathrm{C}}$, $\Delta p = 0.02 k_{\mathrm{C}}$, and $\Delta p = k_{\mathrm{C}}$. By the time the width is equal to the cavity momentum, the forward distribution is essentially flat, and it cannot be used to distinguish different photon number states in a Bayesian sequence.

Another condition we briefly touched on is that the lifetime $1/\gamma$ of the atomic excited state needs to be larger than the time involved in a single Bayes measurement, i.e $\gamma\tau \ll 1$. Similarly, the lifetime $1/\kappa$ of photons in the cavity needs to be larger than the time over which the entire Bayes sequence occurs, i.e $\kappa\tau N \ll 1$ where $N$ is the total number of measurements made.

As an example, we consider a gas of $^{87}$Sr atoms with a temperature of $T = 2\mu$K. The two levels of the atom correspond to the narrow inter-combination line. Typical experimental parameters are $m_{\mathrm{A}} = 1.45 \times 10^{-25}$ kg, $\lambda_{\mathrm{A}} = 698$ nm, $\gamma = 2\pi$ mHz,

$\lambda_C = 813$ nm, and $\kappa = 2\pi \times 10$ kHz [78]. In terms of the recoil angular frequency, $\omega_R = 2\pi \times 3441$ Hz, we have $g \approx -10^{-4}\omega_R$, $k_B T \approx 12\ \hbar\omega_R$, $2\pi/\kappa = 10^{-4}$s, $2\pi/\gamma = 10^3$s, and $\tau = 2\pi/11|g| = 0.26$s.

Although the temperature is very much larger than the recoil energy—implying that the width of the momentum distribution of the atoms is too large for the Bayesian scheme to work—much of this energy can be given to the transverse motion of the atoms rather than the motion along the axis of the cavity. The temperature of the gas of atoms is therefore not a limiting property. However, in this particular setup, the lifetime of photons in the cavity is much smaller than the time over which a single measurement is made, rendering the method unfeasible.

## 7.5 Conclusion

We have demonstrated a Bayesian protocol that measures the number of photons in a cavity by coupling the field to a sequence of two-level atoms and performing Ramsey interferometry. With a proper choice of measurement protocol—that is, a choice of atom-field interaction times—the state of the cavity field can be collapsed onto a number state within fifteen measurements with a relatively high fidelity. We have demonstrated that the scheme can be used for both quantum state preparation and quantum state tomography.

In cases where the cavity linewidth is large, the lifetime of a photon in the cavity is shorter than the timescale of the measurements required for the Bayesian inference scheme. However, in this case, the cavity field relaxes to a steady state between measurements of the atomic inversion. In essence, the system is re-prepared after every single measurement, indicating that we can perform tomography on this steady state. A possible route to implementing tomography in the bad-cavity limit is outlined in reference [25], where measurements distributed in time are treated. This will be the subject of future work.

# Chapter 8

# Conclusion

In this thesis, we have examined a series of physical systems comprised of gases of ultracold atoms trapped in optical lattices, and we have proposed methods to probe these systems with light.

In the first part of this thesis, we examined the ground-state behavior of a gas of ultracold atoms trapped in a rotating optical lattice. By analogy with quasi-momentum in translationally invariant periodic systems, the notion of quasi-angular momentum was introduced to label the eigenstates of a Hamiltonian that has a discrete rotational symmetry. This symmetry language was translated into a many-body formalism where the creation and annihilation operators carried quasi-angular momentum. Systems comprised of strongly-interacting bosons and non-interacting fermions in two-dimensional lattices were investigated. It was shown that quasi-angular momentum is useful in analyzing the ground-state properties of quantum gases of bosons or fermions in rotating optical lattices. In particular, monitoring the quasi-angular momentum of the ground state as a function of rotation allowed us to identify transitions between different circulation values.

For the case of strongly-interacting bosons, the quasi-angular momentum $m$ cycles through the values $m = \mathrm{mod}_N(nl)$, where $l = 0, 1, 2, \ldots$ and $n$ is the number of particles. For the case of fermions, $m$ cycles through the values $m = \mathrm{mod}_N(nl)$, where $l = 0, 1, 2, \ldots$, for odd numbers of particles and $m = \mathrm{mod}_N(n(l + 1/2))$, where

$l = 0, 1, 2, \ldots$, for even numbers of particles. A system of non-interacting fermions is thereby distinguishable from a system of hard-core bosons. Similar behavior obtains for systems of fermions in two-dimensional square lattices.

We also presented a possible avenue by which the quasi-angular momentum of a state can be experimentally determined. We identified characteristics in the momentum distribution distinguishing between different quasi-angular momentum states at low rotation speeds. For single-particle systems in two-dimensional square lattice geometries, such signatures include the existence of a peak at $\mathbf{k} = 0$ only for the $m = 0$ state and peak-spacing differences between $m = 2$ and $m = 1, 3$ state.

In the second part of this thesis, we proposed a scheme for non-destructively probing the dynamics of atoms by coupling them to two counter-propagating modes of a ring cavity. This scheme satisfied three main goals. The probe was weak so that the atoms can be continuously monitored without affecting their dynamics. The cavity fields act simultaneously as both the external lattice potential and the weak probe for the atoms, requiring no external interrogation fields. The signal-to-noise ratio was large enough for feasible experimental detection. This method was applied to the measurement of the Bloch oscillations that non-interacting atoms in an optical lattice undergo when subjected to a constant, external force. These oscillations were reflected in the dynamics of the probe field, and balanced heterodyne detection of the probe field at the cavity output combined with integration in time and across the atomic cloud allowed for signal-to-noise ratios as high as $10^4$.

We then relaxed the condition that the cavity fields act both as the probe field and the lattice field. We applied a variant of this measurement scheme to probe the dynamics of bosonic atoms confined in deep optical lattices and subjected to a constant, external force. Choosing an energy offset $\Omega$ between adjacent lattice wells approximately equal to the interaction energy $U$ in the Bose-Hubbard model, the Hilbert space could be reduced to include only so-called "dipole states." These states are generated from the

unit-filled state by introducing defects that consist of a pair of adjacent sites in which one particle has been moved one site to the left. We derived an effective Hamiltonian in this low-energy subspace.

By exploiting approximate symmetries of the Hamiltonian, we further reduced the number of relevant states. The final numerical complexity of the problem scaled linearly with the number of lattice sites rather than exponentially. However, we showed that the dynamics of the atoms were described by this simple symmetric Hamiltonian only for short times, after which the population of these states decayed to zero. This suggested that the system could be described by a master equation.

We investigated how these dynamics would be reflected in the behavior of the modes of an optical ring-cavity coupled to the gas of atoms. We proposed the following experimental setup. One mode of the cavity is pumped, and the other mode is monitored as photons are scattered off of the atoms. The time-dependence of the probe field amplitude is given schematically by

$$\alpha \propto \sum_{\langle i,j \rangle} \langle \hat{b}_i^\dagger \hat{b}_j \rangle e^{-ikjd}, \tag{8.1}$$

where $\hat{b}_j$ is the operator annihilating a particle on site $j$, and $d$ is the lattice spacing. The quantity on the right hand side is reminiscent of the structure factor of the atomic gas, and we can infer that the atomic motion can be measured and analyzed through the behavior of the light field.

The future direction of this work involves completely characterizing the dynamics of the atoms and the probe field coupled to these atoms. This relatively simple many-body system can then be used as a probe for more complicated many-particle systems. For instance, by characterizing how the dynamics change when long-range interactions between atoms are introduced, it may be possible to use this scheme to probe long-range correlations between atoms.

In the final part of this thesis, we reversed the paradigm of using light to study

atomic systems and instead proposed a quantum non-demolition measurement of the cavity photon number by entangling the field with two momentum states of long-lived atoms. By means of a sequence of $\pi/2$-pulses, the internal states of the atom are coupled to its external states. We measure the internal state of the atom at the end of the measurement sequence. By use of quantum Bayesian inference and a series of measurements, the state of the field collapses to a photon number state. This scheme can be used not only to prepare a number state of the cavity field, but it also allows us to perform state tomography to reconstruct an initial prepared state of the field.

We note finally that throughout this thesis, there was a strong hierarchy in the atom-field interaction. The experimental exploration of quasi-angular momentum in gases of atoms trapped in rotating lattices comes by way of time-of-flight measurements. In this case, the dynamics of the atoms is primary, and the light-field plays no part in the observables of interest. The use of cavity fields to probe the atomic systems in both chapters 5 and 6 again implies primacy of the atomic dynamics. We spent a lot of time determining exactly when the dynamics of the probe fields did not affect the atomic motion. Finally, in the Bayesian scheme for measuring the cavity photon number, the atomic motion affected the photon dynamics only weakly, whereas the dynamics of the atoms were very different for different photon numbers.

As evidenced by recent work where the atoms and light-field must be treated on an equal footing [7, 122], it will be interesting to move beyond these models where there is a natural hierarchy in the atom-field interaction. This will be the context of future work.

## Bibliography


[1] A. Alberti, G. Ferrari, V. V. Ivanov, and G. M. Tino. Coherent transport of atomic wave packets in amplitude-modulated optical lattices under the effect of gravity. e-print arXiv:0903.0724, 2009.

[2] A. Albus, F. Illuminati, and J. Eisert. Mixtures of bosonic and fermionic atoms in optical lattices. Phys. Rev. A, 68(2):023606, 2003.

[3] B. P. Anderson and M. A. Kasevich. Macroscopic Quantum Interference from Atomic Tunnel Arrays. Science, 282:1686, 1998.

[4] M. H. Anderson, J. R. Ensher, M. R. Matthews, C. E. Wieman, and E. A. Cornell. Observation of Bose-Einstein condensation in a dilute atomic vapor. Science, 269(5221):198, 1995.

[5] M. A. Baranov, K. Osterloh, and M. Lewenstein. Fractional Quantum Hall States in Ultracold Rapidly Rotating Dipolar Fermi Gases. Phys. Rev. Lett., 94:070404, 2005.

[6] K. Baumann, C. Guerlin, F. Brennecke, and T. Esslinger. The Dicke Quantum Phase Transition in a Superfluid Gas Coupled to an Optical Cavity. e-print arXiv:0912.3261, 2009.

[7] K. Baumann, C. Guerlin, F. Brennecke, and T. Esslinger. The Dicke Quantum Phase Transition in a Superfluid Gas Coupled to an Optical Cavity. e-print arXiv:0912.3261, 2009.

[8] M. Ben Dahan, E. Peik, J. Reichel, Y. Castin, and C. Salomon. Bloch Oscillations of Atoms in an Optical Potential. Phys. Rev. Lett., 76:4508, 1996.

[9] R. Bhat, M. J. Holland, and L. D. Carr. Bose-Einstein condensates in rotating lattices. Phys. Rev. Lett., 96(6):60405, 2006.

[10] R. Bhat, M. Krämer, J. Cooper, and M. J. Holland. Hall effects in Bose-Einstein condensates in a rotating optical lattice. Phys. Rev. A, 76:043601, 2007.

[11] R. Bhat, B. M. Peden, B. T. Seaman, M. Krämer, L. D. Carr, and M. J. Holland. Quantized vortex states of strongly interacting bosons in a rotating optical lattice. Phys. Rev. A, 74:063606, 2006.

[12] Rajiv Bhat. Bosons in rotating optical lattices. University of Colorado at Boulder, 2008.

[13] K. M. Birnbaum, A. Boca, R. Miller, A. D. Boozer, T. E. Northup, and H. J. Kimble. Photon blockade in an optical cavity with one trapped atom. Nature, 436:87, 2005.

[14] S. Blatt, A. D. Ludlow, G. K. Campbell, J. W. Thomsen, T. Zelevinsky, M. M. Boyd, J. Ye, X. Baillard, M. Fouché, R. Le Targat, A. Brusch, P. Lemonde, M. Takamoto, F.-L. Hong, H. Katori, and V. V. Flambaum. New Limits on Coupling of Fundamental Constants to Gravity Using $^{87}$Sr Optical Lattice Clocks. Phys. Rev. Lett., 100:140801, 2008.

[15] I Bloch. Ultracold quantum gases in optical lattices. Nat. Phys., 1:23, 2005.

[16] C. C. Bradley, C. A. Sackett, J. J. Tollett, and R. G. Hulet. Evidence of Bose-Einstein condensation in an atomic gas with attractive interactions. Phys. Rev. Lett., 75(9):1687, 1995.

[17] M. Brune, J. Bernu, C. Guerlin, S. Deléglise, C. Sayrin, S. Gleyzes, S. Kuhr, I. Dotsenko, J.-M. Raimond, and S. Haroche. Process Tomography of Field Damping and Measurement of Fock State Lifetimes by Quantum Nondemolition Photon Counting in a Cavity. Phys. Rev. Lett., 101:240402, 2008.

[18] A. Buchleitner and A. R. Kolovski. Interaction-Induced Decoherence of Atomic Bloch Oscillations. Phys. Rev. Lett., 91:253002, 2003.

[19] P. Buonsante, R. Franco, and V. Penna. An algebraic approach to the study of weakly excited states for a condensate in a ring geometry. J. Phys. A, 38(39):8393, 2005.

[20] P. Buonsante, V. Penna, and A. Vezzani. Attractive ultracold bosons in a necklace optical lattice. Phys. Rev. A., 72:043620, 2005.

[21] H. J. Carmichael and K. Kim. A quantum trajectory unraveling of the superradiance master equation. Optics Comm., 179:417, 2000.

[22] Howard J. Carmichael. Statistical Methods in Quantum Optics 2: Non-Classical Fields. Springer, 2008.

[23] I. Carusotto, L. Pitaevskii, S. Stringari, G. Modugno, and M. Inguscio. Sensitive Measurement of Forces at the Micron Scale Using Bloch Oscillations of Ultracold Atoms. Phys. Rev. Lett., 95:93202, 2005.

[24] L. Casetti and V. Penna. Vortex structures in a chain of coupled bosonic wells and the Mott regime. J. Low Temp. Phys., 126:455–460, 2002.

[25] C. M. Caves. Quantum mechanics of measurements distributed in time. A path-integral formulation. Phys. Rev. D, 33:1643, 1986.

[26] S. Chaudhury, G. A. Smith, K. Schulz, and P. S. Jessen. Continuous Nondemolition Measurement of the Cs Clock Transition Pseudospin. Phys. Rev. Lett., 96(4):43001, 2006.

[27] W. Chen, D. Meiser, and P. Meystre. Cavity QED determination of atomic number statistics in optical lattices. Phys. Rev. A, 75:023812, 2007.

[28] P. Cladé, E. de Mirandes, M. Cadoret, S. Guellati-Khèlifa, C. Schwob, F. Nez, L. Julien, and F. Biraben. Determination of the Fine Structure Constant Based on Bloch Oscillations of Ultracold Atoms in a Vertical Optical Lattice. Phys. Rev. Lett., 96:033001, 2006.

[29] J. P. Clemens, L. Horvath, B. C. Sanders, and H. J. Carmichael. Collective spontaneous emission from a line of atoms. Phys. Rev. A, 68:023809, 2003.

[30] C. Cohen-Tannoudji, J. Dupont-Roc, and G. Grynberg. Atom-Photon Interactions. Wiley, 1992.

[31] J. Dalibard, Y. Castin, and K. Molmer. Wave-Function Approach to Dissipative Processes in Quantum Optics. Phys Rev. Lett., 68(5):580, 1992.

[32] K. B. Davis, M. O. Mewes, M. R. Andrews, N. J. van Druten, D. S. Durfee, D. M. Kurn, and W. Ketterle. Bose-Einstein condensation in a gas of sodium atoms. Phys. Rev. Lett., 75(22):3969, 1995.

[33] B. DeMarco and D. S. Jin. Onset of fermi degeneracy in a trapped atomic gas. Science, 285(5434):1703, 1999.

[34] W. S. Dias, E. M. Nascimento, M. L. Lyra, and F. A. de Moura. Frequency doubling of Bloch oscillations for interacting electrons in a static electric field. Phys. Rev. B, 76:155124, 2007.

[35] R. Dum, P. Zoller, and H. Ritsch. Monte Carlo simulation of the atomic master equation for spontaneous emission. Phys Rev. A, 45(7):4879, 1992.

[36] G. Ferrari, N. Poli, F. Sorrentino, and G. M. Tino. Long-Lived Bloch Oscillations with Bosonic Sr Atoms and Application to Gravity Measurement at the Micrometer Scale. Phys. Rev. Lett., 97:060402, 2006.

[37] A. L. Fetter and J. D. Walecka. Quantum Theory of Many-Particle Systems. Dover, New York, 2003.

[38] U. R. Fischer, P. O. Fedichev, and A. Recati. Vortex liquids and vortex quantum Hall states in trapped rotating Bose gases. J. Phys. B: At. Mol. Opt. Phys., 37:S301, 2004.

[39] M. P. A. Fisher, P. B. Weichman, G. Grinstein, and D. S. Fisher. Boson localization and the superfluid-insulator transition. Phys. Rev. B, 40:546, 1989.

[40] T. M. Fortier, N. Ashby, J. C. Bergquist, M. J. Delaney, S. A. Diddams, T. P. Heavner, L. Hollberg, W. M. Itano, S. R. Jefferts, K. Kim, F. Levi, L. Lorini, W. H. Oskay, T. E. Parker, J. Shirley, and J. E. Stalnaker. Precision Atomic Spectroscopy for Improved Limits on Variation of the Fine Structure Constant and Local Position Invariance. Phys. Rev. Lett., 98:070801, 2007.

[41] M. Foss-Feig, M. Hermele, and A. M. Rey. Probing the Kondo Lattice Model with Alkaline Earth Atoms. e-print arXiv:0912.4762, 2009.

[42] J. K. Freericks. Quenching Bloch oscillations in a strongly correlated material: Nonequilibrium dynamical mean-field theory. Phys. Rev. B, 77:075109, 2008.

[43] C. W. Gardiner, A. S. Parkins, and P. Zoller. Wave-function quantum stochastic differential equations and quantum-jump simulation methods. Phys Rev. A, 46(7):4363, 1992.

[44] C. W. Gardiner and P. Zoller. Quantum Noise. Springer-Verlag, 2004.

[45] M. Girardeau. Relationship between systems of impenetrable bosons and fermions in one dimension. J. of Math. Phys., 1:516, 2004.

[46] S. Gleyzes, S. Kuhr, C. Guerlin, J. Bernu, S. Deléglise, B. H. Ulrich, M. Brune, J.-M. Raimond, and S. Haroche. Quantum jumps of light recording the birth and death of a photon in a cavity. Nature, 446:297, 2007.

[47] M. Greiner, O. Mandel, T. Esslinger, T. W. Hänsch, and I. Bloch. Quantum phase transition from a superfluid to a Mott insulator in a gas of ultracold atoms. Nature, 415:39, 2002.

[48] M. Greiner, C. A. Regal, and D. S. Jin. Emergence of a molecular Bose-Einstein condensate from a Fermi gas. Nature, 426(6966):537, 2003.

[49] A. Griessner, D. Jaksch, and P. Zoller. Cavity-assisted nondestructive laser cooling of atomic qubits. J. Phys. B, 37:1419, 2003.

[50] C. Guerlin, J. Bernu, S. Deléglise, C. Sayrin, S. Gleyzes, S. Kuhr, M. Brune, J.-M. Raimond, and S. Haroche. Progressive field-state collapse and quantum non-demolition photon counting. Nature, 448:889, 2007.

[51] S. Gupta, K. L. Moore, K. W. Murch, and D. M. Stamper-Kurn. Cavity Nonlinear Optics at Low Photon Numbers from Collective Atomic Motion. Phys. Rev. Lett., 99:213601, 2007.

[52] M. Hafezi, A. S. Sorensen, E. Demler, and M. D. Lukin. Fractional quantum Hall effect in optical lattices. Phys. Rev. A, 76:023613, 2007.

[53] M. Holland, S. Marksteiner, P. Marte, and P. Zoller. Measurement Induced Localization from Spontaneous Decay. Phys Rev. Lett., 76(20):3683, 1996.

[54] M. J. Holland. Unraveling Quantum Dissipation in the Frequency Domain. Phys Rev. Lett., 81(23):5117, 1998.

[55] M. J. Holland and K. Burnett. Interferometric detection of optical phase shifts at the Heisenberg limit. Phys. Rev. Lett., 71:1355, 1993.

[56] M. J. Holland, D. F. Walls, and P. Zoller. Quantum Nondemolition Measurements of Photon Number by Atomic-Beam Deflection. Phys. Rev. Lett., 67(13):1716, 1991.

[57] C. J. Hood, M. S. Chapman, T. W. Lynn, and H. J. Kimble. Real-Time Cavity QED with Single Atoms. Phys. Rev. Lett., 80(19):4157, 1998.

[58] C. J. Hood, T. W. Lynn, A. C. Doherty, A. S. Parkins, and H. J. Kimble. The atom-cavity microscope: Single atoms bound in orbit by single photons. Science, 287:1447, 2000.

[59] D. B. Hume, T. Rosenband, and D. J. Wineland. High-Fidelity Adaptive Qubit Detection through Repetitive Quantum Nondemolition Measurements. Phys. Rev. Lett, 99:120502, 2007.

[60] F. Illuminati and A. Albus. High-Temperature Atomic Superfluidity in lattice Bose-Fermi Mixtures. Phys. Rev. Lett., 93(9):090406, 2004.

[61] M. Inguscio, W. Ketterle, and C. Salomon, editors. Ultra-cold Fermi Gases (Proceedings of the International School of Physics "Enrico Fermi"). IOP Press, 2007.

[62] V. V. Ivanov, A. Alberti, M. Schioppo, G. Ferrari, M. Artoni, M. L. Chiofalo, and G. Tino. Coherent Delocalization of Atomic Wave Packets in Driven Lattice Potentials. Phys. Rev. Lett., 100:043602, 2008.

[63] J. D. Jackson. Classical Electrodynamics. Wiley, 1999.

[64] D. Jaksch, C. Bruder, J. I. Cirac, C. W. Gardiner, and P. Zoller. Cold Bosonic Atoms in Optical Lattices. Phys. Rev. Lett., 81:3108, 1998.

[65] D. Jaksch and P. Zoller. Creation of effective magnetic fields in optical lattices: the Hofstadter butterfly for cold neutral atoms. New J. Phys., 5:56, 2003.

[66] P. Jordan and E. Wigner. Über das Paulische äquivalenzverbot. Z. Phys., 47:631, 1928.

[67] C. Kittel. Introduction to Solid State Physics. Wiley, 1996.

[68] M. Köhl, H. Moritz, T. Stöferle, K. Günter, and T. Esslinger. Fermionic Atoms in a Three Dimensional Optical Lattice: Observing Fermi Surfaces, Dynamics, and Interactions. Phys. Rev. Lett., 94:80403, 2005.

[69] L. D. Landau and E. M. Lifshitz. Mechanics. Butterworth-Heinemann, Ltd, Oxford, 1976.

[70] J. Larson, B. Damski, G. Morigi, and M. Lewenstein. Mott-Insulator States of Ultracold Atoms in Optical Resonators. Phys. Rev. Lett., 100:050401, 2008.

[71] R. H. Lehmberg. Radiation From an $N$-Atom System. I. General Formalism. Phys. Rev. A, 2:883, 1969.

[72] D. R. Leibrandt, J. Labaziewicz, V. Vuletic, and I. L. Chuang. Cavity Sideband Cooling of a Single Trapped Ion. Phys. Rev. Lett., 103:103001, 2009.

[73] I. D. Leroux, M. H. Schleier-Smith, and V. Vuletic. Implementation of Cavity Squeezing of a Collective Atomic Spin. Phys. Rev. Lett., 104:073602, 2010.

[74] T. O. Levante, M. Baldus, B. H. Meier, and R. R. Ernst. Formalized quantum mechanical Floquet theory and its application to sample spinning in nuclear magnetic resonance. Molec. Phys., 86:1195, 1995.

[75] E. H. Lieb and W. Liniger. Exact analysis of an interacting Bose gas. I. The general solution and the ground state. Phys. Rev., 130(4):1605, 1963.

[76] R. Loudon. The Quantum Theory of Light. Oxford Science Publications, 2003.

[77] W. H. Louisell. Quantum Statistical Properties of Radiation. Wiley, 1990.

[78] A. D. Ludlow, M. M. Boyd, T. Zelevinsky, S. M. Foreman, S. Blatt, M. Notcutt, T. Ido, and J. Ye. Systematic Study of the $^{87}$Sr Clock Transition in an Optical Lattice. Phys. Rev. Lett., 96:033003, 2006.

[79] A. D. Ludlow, T. Zelevinsky, G. K. Campbell, S. Blatt, M. M. Boyd, M. H. G. de Miranda, M. J. Martin, J. W. Thomsen, S. M. Foreman, Jun Ye, T. M. Fortier, J. E. Stalnaker, S. A. Diddams, Y. Le Coq, Z. W. Barber, N. Poli, N. D. Lemke, K. M. Beck, and C. W. Oates. Sr Lattice Clock at 1x10e16 Fractional Uncertainty by Remote Optical Evaluation with a Ca Clock. Science, 319:1805, 2008.

[80] M. P. Marder. Condensed Matter Physics. Wiley, New York, 2000.

[81] L. Mathey, I. Danshita, and C. W. Clark. Creating a supersolid in one-dimensional Bose mixtures. Phys. Rev. A, 79:011602(R), 2009.

[82] P. Mehta and N. Andrei. Nonequilibrium Transport in Quantum Impurity Models: The Bethe Ansatz for Open Systems. Phys. Rev. Lett., 96:216802, 2006.

[83] D. Meiser and M. J. Holland. Robustness of Heisenberg-limited interferometry with balanced Fock states. New J. Phys., 11:033002, 2009.

[84] D. Meiser, J. Ye, D. Carlson, and M. J. Holland. Prospects for a mHz-Linewidth Laser. Phys. Rev. Lett., 102:163601, 2009.

[85] D. Meiser, Jun Ye, and M. J. Holland. Spin squeezing in optical lattice clocks via lattice-based QND measurements. New J. Phys., 10:073014, 2008.

[86] I. B. Mekhov, C. Maschler, and H. Ritsch. Cavity-Enhanced Light Scattering in Optical Lattices to Probe Atomic Quantum Statistics. Phys. Rev. Lett., 98:100402, 2007.

[87] I. B. Mekhov and H. Ritsch. Quantum Nondemolition Measurements and State Preparation in Quantum Gases by Light Detection. Phys. Rev. Lett., 102:020403, 2009.

[88] P. Meystre and M. Sargent III. Elements of Quantum Optics. Springer, 2007.

[89] R. Miller, T. E. Northup, K. M. Birnbaum, A. Boca, Boozer A. D., and H. J. Kimble. Trapped atoms in cavity QED: coupling quantized light and matter. J. Phys. B: At. Mol. Opt. Phys., 38:S551, 2005.

[90] J. N. Milstein, S. Kokkelmans, and M. J. Holland. Resonance theory of the crossover from Bardeen-Cooper-Schrieffer superfluidity to Bose-Einstein condensation in a dilute Fermi gas. Phys. Rev. A, 66:43604, 2002.

[91] O. Morsch, J. H. Müller, M. Cristiani, D. Ciampini, and E. Arimondo. Bloch Oscillations and Mean-Field Effects of Bose-Einstein Condensates in 1D Optical Lattices. Phys. Rev. Lett., 87:140402, 2001.

[92] K.K. Ni, S. Ospelkaus, M. H. G. de Miranda, A. Pe'er, B. Neyenhuis, J. J. Zirbel, S. Kotochigova, P. S. Julienne, D. S. Jin, and J. Ye. A high phase-space-density gas of polar molecules. Science, 322:231, 2008.

[93] A. E. B. Nielsen and K. Mølmer. Atomic spin squeezing in an optical cavity. Phys. Rev. A, 77:063811, 2008.

[94] T. Oka and H. Aoki. Ground-State Decay Rate for the Zener Breakdown in Band and Mott Insulators. Phys. Rev. Lett., 95:137601, 2005.

[95] W. H. Oskay, S. A. Diddams, E. A. Donley, T. M. Fortier, T. P. Heavner, L. Hollberg, W. M. Itano, S. R. Jefferts, M. J. Delaney, K. Kim, F. Levi, T. E. Parker, and J. C. Bergquist. Single-Atom Optical Clock with High Accuracy. Phys. Rev. Lett., 97:020801, 2006.

[96] C. Ospelkaus, S. Ospelkaus, L. Humbert, P. Ernst, K. Sengstock, and K. Bongs. Ultracold Heteronuclear Molecules in a 3D Optical Lattice. Phys. Rev. Lett., 97:120402, 2006.

[97] S. Ospelkaus, C. Ospelkaus, O. Wille, M. Succo, P. Ernst, K. Sengstock, and K. Bongs. Localization of Bosonic Atoms by Fermionic Impurities in a Three-Dimensional Optical Lattice. Phys. Rev. Lett., 96:180403, 2006.

[98] K. Osterloh, M. Baig, L. Santos, P. Zoller, and M. Lewenstein. Cold Atoms in Non-Abelian Gauge Potentials: From the Hofstadter "Moth" to Lattice Gauge Theory. Phys. Rev. Lett., 95:010403, 2005.

[99] R. N. Palmer and D. Jaksch. High-Field Fractional Quantum Hall Effect in Optical Lattices. Phys. Rev. Lett., 96:180407, 2006.

[100] B. Paredes, P. Fedichev, J. I. Cirac, and P. Zoller. $\frac{1}{2}$-anyons in Small Atomic Bose-Einstein Condensates. Phys. Rev. Lett., 87:010402, 2001.

[101] B. M. Peden, R. Bhat, M. Krämer, and M. J. Holland. Quasi-angular momentum of Bose and Fermi gases in rotating optical lattices. J. Phys. B: At. Mol. Opt. Phys., 40:3725, 2007.

[102] B. M. Peden, D. Meiser, M. L. Chiofalo, and M. J. Holland. Non-destructive cavity QED probe of Bloch oscillations in a gas of ultracold atoms. Phys. Rev. A, 80:043803, 2009.

[103] R. A. Pepino, J. Cooper, D. Z. Anderson, and M. J. Holland. Atomtronic Circuits of Diodes and Transistors. Phys. Rev. Lett., 103:140405, 2009.

[104] M. B. Plenio and P. L. Knight. The quantum-jump approach to dissipative dynamics in quantum optics. Rev. Mod. Phys., 70(1):101, 1998.

[105] S. Reich, C. Thomsen, J. Maultzsch, and M. Janina. Carbon nanotubes: Basic concepts and physical properties. Wiley-VCH, 2004.

[106] A. M. Rey, K. Burnett, I. I. Satija, and C. W. Clark. Lifshitz-like transition and enhancement of correlations in a rotating bosonic ring lattice. Phys. Rev. A, 75:063616, 2007.

[107] Ana Maria Rey. Ultracold Bosonic Atoms in Optical Lattices. University of Maryland College Park, 2004.

[108] G. Roati, E. de Mirandes, F. Ferlaino, H. Ott, G. Modugno, and M. Inguscio. Atom Interferometry with Trapped Fermi Gases. Phys. Rev. Lett., 92:230402, 2004.

[109] T. Rosenband, D. B. Hume, P. O. Schmidt, C. W. Chou, A. Brusch, L. Lorini, W. H. Oskay, R. E. Drullinger, T. M. Fortier, J. E. Stalnaker, S. A. Diddams, W. C. Swann, N. R. Newbury, W. M. Itano, D. J. Wineland, and J. C. Bergquist. Frequency ratio of Al+ and Hg+ single-ion optical clocks; Metrology at the 17th decimal place. Science, 319:1808, 2008.

[110] C. Rubbo. Private communication, 2010.

[111] S. Sachdev. Quantum Phase Transitions. Cambridge University Press, New York, 1999.

[112] S. Sachdev, K. Sengupta, and S. M. Girvin. Mott insulators in strong electric fields. Phys. Rev. B, 66:075128, 2002.

[113] H. Sambe. Steady States and Quasienergies of a Quantum-Mechanical System in an Oscillating Field. Phys. Rev. A, 7:2203, 1973.

[114] I. I. Satija, D. C. Dakin, and C. W. Clark. Metal-Insulator Transition Revisited for Cold Atoms in Non-Abelian Gauge Potentials. Phys. Rev. Lett., 97:216401, 2006.

[115] M. Schleier-Smith, I. D. Leroux, and V. Vuletic. Squeezing the collective spin of a dilute atomic ensemble by cavity feedback. Phys. Rev. A, 81:021804(R), 2010.

[116] T. D. Schultz. Note on the one-dimensional gas of impenetrable point-particle bosons. J. Math. Phys., 4:666, 1966.

[117] V. Schweikhard, I. Coddington, P. Engels, V. P. Mogendorff, and E. A. Cornell. Rapidly Rotating Bose-Einstein Condensates in and Near the Lowest Landau Level. Phys. Rev. Lett., 92:040404, 2004.

[118] B. T. Seaman, M. Krämer, D. Z. Anderson, and M. J. Holland. Atomtronics: Ultracold-atom analogs of electronic devices. Phys. Rev. A, 75:023615, 2007.

[119] J. H. Shirley. Solution of the Schröinger Equation with a Hamiltonian Periodic in Time. Phys. Rev., 138:B979, 1965.

[120] C. Sias, A. Zenesini, H. Lignier, S. Wimberger, D. Ciampini, O. Morsch, and E. Arimondo. Resonantly Enhanced Tunneling of Bose-Einstein Condensates in Periodic Potentials. Phys. Rev. Lett., 98:120403, 2007.

[121] A .E. Siegman. Lasers. University Science Books, 1986.

[122] A. O. Silver, M. Hohenadler, M. J. Bhaseen, and B. D. Simons. Bose-Hubbard models coupled to cavity light fields. Phys. Rev. A, 81:023617, 2010.

[123] J. Simon, H. Tanji, J. K. Thompson, and V. Vuletic. Interfacing Collective Atomic Excitations and Single Photons. Phys. Rev. Lett., 98:183601, 2007.

[124] G. A. Smith, S. Chaudhury, A. Silberfarb, I. H. Deutsch, and P. S. Jessen. Continuous weak measurement and nonlinear dynamics in a cold spin ensemble. Phys. Rev. Lett., 93:163602, 2004.

[125] A. S. Sørensen, E. Demler, and M. D. Lukin. Fractional Quantum Hall States of Atoms in Optical Lattices. Phys. Rev. Lett., 94:86803, 2005.

[126] M. Ueda and A. J. Leggett. Ground-State Properties of a Rotating Bose-Einstein Condensate with Attractive Interaction. Phys. Rev. Lett., 83(8):1489, 1999.

[127] D. van Oosten, P. van der Straten, and H. T. C. Stoof. Quantum phases in an optical lattice. Phys. Rev. A, 63:053601, 2001.

[128] B. P. Venkatesh, M. Trupke, E. A. Hinds, and D. H. J. O'Dell. Atomic Bloch-Zener oscillations for sensitive force measurements in a cavity. Phys. Rev. A, 80:063834, 2009.

[129] P. Vignolo, R. Fazio, and M. P. Tosi. Quantum vortices in optical lattices. Phys. Rev. A, 76:023616, 2007.

[130] N. K. Wilkin and J. M. F. Gunn. Condensation of "Composite Bosons" in a Rotating BEC. Phys. Rev. Lett., 84:6, 2000.

[131] P. J. Windpassinger, D. Oblak, P. G. Petrov, M. Kubasik, M. Saffman, C. L. Alzar, J. Appel, J. H. Muller, N. Kjærgaard, and E. S. Polzik. Nondestructive Probing of Rabi Oscillations on the Cesium Clock Transition near the Standard Quantum Limit. Phys. Rev. Lett., 100(10):103601, 2008.

[132] P. Wolf, P. Lemonde, A. Lambrecht, S. Bize, A. Landragin, and A. Clairon. From optical lattice clocks to the measurement of forces in the Casimir regime. Phys. Rev. A, 75:63608, 2007.

[133] A. Yariv. Optical Electronics. CBS College Publishing, 1985.

[134] H. Zoubi and H. Ritsch. Superradiant and dark exciton states in an optical lattice within a cavity. Europhys. Lett., 87:23001, 2009.

[135] M. W. Zwierlein, J. R. Abo-Shaeer, A. Schirotzek, C. H. Schunck, and W. Ketterle. Vortices and superfluidity in a strongly interacting Fermi gas. Nature, 435:1047, 2005.

# Appendix A

# Numerical Implementation

## A.1 Lattices

The Hamiltonian for an atom trapped in a one-dimensional sinusoidal lattice is

$$H(z) = -\frac{\hbar^2}{2m}\frac{d^2}{dz^2} + V_0 \cos^2(kz). \tag{A.1}$$

Scaling energies by the recoil energy, $E_R = \hbar^2 k^2/2m$, momenta by the lattice momentum, $\hbar k$, and positions by the inverse lattice wave vector, $1/k = d/\pi$, this becomes

$$H(z) = E_R \left( -\frac{d^2}{dz^2} + \frac{V_0}{2E_R} + \frac{V_0}{2E_R}\cos(2kz) \right). \tag{A.2}$$

Defining,

$$\begin{aligned} a &= \frac{E}{E_R} - \frac{V_0}{2E_R}, \\ t &= \frac{V_0}{4E_R}, \end{aligned} \tag{A.3}$$

the time-dependent Schrödinger equation can be written as

$$0 = \frac{d^2}{dz^2}\varphi(z) + (a - 2t\cos(2z))\varphi(z). \tag{A.4}$$

This equation is known as Mathieu's equation.

### A.1.1 Mathieu functions

The solutions, $\varphi$, can be written according to Bloch theory as

$$\varphi_k(\phi) = e^{ik\phi} u_k(\phi) : u_k(\phi - \pi) = u_k(\phi), \tag{A.5}$$

for special values of $a$ that make $\varphi_k(\phi)$ periodic with period $\pi$. These are known as Mathieu characteristic values, $a_k(t)$ and $b_k(t)$, and they have the following important properties:

$$a_k(t) = b_k(t) : k \notin \mathbb{Z}, \tag{A.6a}$$

$$a_0(t) < b_1(t) < a_1(t) < b_2(t) < a_2(t) < \cdots : t \neq 0, \tag{A.6b}$$

$$a_{-k}(t) = a_k(t), \tag{A.6c}$$

$$b_{-k}(t) = b_k(t). \tag{A.6d}$$

From now on, we will leave off the parameter $t$ as it is fixed by the lattice depth. We may decompose $\varphi_k(\phi)$ into parts,

$$C_k(\phi) = \frac{\varphi_k(\phi) + \varphi_k(-\phi)}{2}, \tag{A.7}$$

$$S_k(\phi) = \frac{\varphi_k(\phi) - \varphi_k(-\phi)}{2i}, \tag{A.8}$$

which are respectively even and odd functions of $\phi$. These two functions, known as the Mathieu cosine and sine functions, respectively, are also eigenstates of Mathieu's equation with respective eigenvalues, $a_k$ and $b_k$. When $k$ is not an integer, they are degenerate. If $k = m$ is an integer, we note that

$$\lim_{k \to m^-} C_k(\phi) = 0, \tag{A.9}$$

$$\lim_{k \to m^+} S_k(\phi) = 0, \tag{A.10}$$

so that $C$ and $S$ are exactly equal to the Bloch solutions in this case, corresponding to $a_k$ and $b_k$, respectively.

With these facts in hand, the Mathieu cosine and sine functions can be used to construct the Bloch solutions in a systematic way. It is clear from equation A.5 that the quasi-momenta, $q$, are limited to the interval, $-1 \leq q \leq 1$. Equations A.6c and A.6d

allow us to consider only $k \geq 0$. Excluding integer values for now, write $k$ as

$$k \to k_{n,q} = \begin{cases} n + |q| & \text{if} \quad n = \text{even} \\ n + |q| - 1 & \text{if} \quad n = \text{odd} \end{cases}, \tag{A.11}$$

$$n \in \mathbb{Z}^+ \cup \{0\}, \tag{A.12}$$

$$q \in (-1, 0) \cup (0, 1). \tag{A.13}$$

Defining

$$C_q^{(n)}(\phi) = C_{k_{n,q}}(\phi), \tag{A.14}$$

$$S_q^{(n)}(\phi) = S_{k_{n,q}}(\phi), \tag{A.15}$$

$$u_q^{(n)}(\phi) = u_{k_{n,q}}(\phi) = u_{|q|}^{(n)}(\phi), \tag{A.16}$$

and

$$\begin{aligned} \varphi_q^{(n)}(\phi) &= C_q^{(n)}(\phi) + i\text{Sign}(q) S_q^{(n)}(\phi) \\ &= \frac{\varphi_{k_{n,q}}(\phi) + \varphi_{k_{n,q}}(-\phi)}{2} + i\ \text{Sign}(q) \frac{\varphi_{k_{n,q}}(\phi) - \varphi_{k_{n,q}}(-\phi)}{2i} \\ &= e^{ik_{n,q}\phi} \frac{u_{|q|}^{(n)}(\phi) + \text{Sign}(q) u_{|q|}^{(n)}(\phi)}{2} + e^{-ik_{n,p}\phi} \frac{u_{|q|}^{(n)}(-\phi) - \text{Sign}(q) u_{|q|}^{(n)}(-\phi)}{2} \\ &= e^{\text{Sign}(q) ik_{n,q}\phi} u_{|q|}^{(n)}(\text{Sign}(q)\phi), \end{aligned} \tag{A.17}$$

we have that

$$\begin{aligned} \varphi_q^{(n)}(\phi - \pi) &= e^{\text{Sign}(q) ik_{n,q}(\phi - \pi)} u_{|q|}^{(n)}(\text{Sign}(q)(\phi - \pi)) \\ &= e^{-\text{Sign}(q) ik_{n,q}\pi} e^{\text{Sign}(q) ik_{n,q}\phi} u_{|q|}^{(n)}(\text{Sign}(q)\phi) \\ &= e^{-\text{Sign}(q) ik_{n,q}\pi} \psi_q^{(n)}(\phi). \end{aligned} \tag{A.18}$$

The exponential factor out front is

$$e^{-\text{Sign}(q) ik_{n,q}\pi} = \left\{ \begin{bmatrix} e^{-\text{Sign}(q) i(n+|q|)\pi} & \text{if} \quad n = \text{even} \\ e^{-\text{Sign}(q) i(n+|q|-1)\pi} & \text{if} \quad n = \text{odd} \end{bmatrix} \right. = e^{-iq\pi}, \tag{A.19}$$

so that we can write

$$\varphi_q^{(n)}(\phi - \pi) = e^{-iq\pi} \varphi_q^{(n)}(\phi). \tag{A.20}$$

For $k \in \mathbb{Z}$, we let

$$k \to k_{n,q} = \left\{ \begin{bmatrix} n+|q| & \text{if} \quad n = \text{even} \\ n+|q|-1 & \text{if} \quad n = \text{odd} \end{bmatrix} \right., \tag{A.21}$$

$$n \in \mathbb{Z}^+ \cup \{0\}, \tag{A.22}$$

$$q \in [-1, 1), \tag{A.23}$$

and define

$$C_0^{(2p+1)}(\phi) = \varphi_0^{(2p+1)}(\phi) = C_{2p}(\phi), \tag{A.24}$$

$$S_{-1}^{(2p+1)}(\phi) = \varphi_{-1}^{(2p+1)}(\phi) = S_{2p+1}(\phi), \tag{A.25}$$

$$S_0^{(2p)}(\phi) = \varphi_0^{(2p)}(\phi) = S_{2p}(\phi), \tag{A.26}$$

$$C_{-1}^{(2p)}(\phi) = \varphi_{-1}^{(2p)}(\phi) = C_{2p-1}(\phi), \tag{A.27}$$

which is consistent with the definition of $k_{n,q}$ except for $\varphi_{-1}^{(2p)}(\phi)$ which we must reserve as a special case. Implicitly, this assumes that

$$S_0^{(2p+1)}(\phi) = C_{-1}^{(2p+1)}(\phi) = C_0^{(2p)}(\phi) = S_{-1}^{(2p-1)}(\phi) = 0, \tag{A.28}$$

It is simple to show that these still satisfy

$$\varphi_q^{(n)}(\phi - \pi) = e^{-iq\pi}\varphi_q^{(n)}(\phi). \tag{A.29}$$

Thus, we can interpret $q$ as the quasi-momentum and $n$ as the band index of this state.

Finally, the eigenvalues are given by the expression

$$E = E_R \left( a + \frac{V_0}{2E_R} \right). \tag{A.30}$$

For $E_q^{(n)}$, we take

$$E_q^{(n)} : a \to a_{k_{n,q}} : q \notin \mathbb{Z}, \tag{A.31}$$

$$E_0^{(2p)} : a \to b_{2p}, \tag{A.32}$$

$$E_{-1}^{(2p)} : a \to a_{2p-1}, \tag{A.33}$$

$$E_0^{(2p+1)} : a \to a_{2p}, \tag{A.34}$$

$$E_{-1}^{(2p+1)} : a \to b_{2p+1}. \tag{A.35}$$

### A.1.2 Hamiltonian decomposition in momentum space

Instead of using the Mathieu sine and cosine functions – which are special functions implemented in, for instance, Mathematica – we can expand the Hamiltonian, equation A.1, in momentum eigenstates. Implementing periodic boundary conditions as an approximation, this generates a finite-dimensional matrix that can be numerically diagonalized to construct the Bloch eigenstates.

We choose a set of momentum eigenstates,

$$\langle z|n,q\rangle = \mathcal{N} e^{i(2kn+q)z}, \tag{A.36}$$

$$n \in \mathbb{Z}, \tag{A.37}$$

$$0 \leq q \leq 2k, \tag{A.38}$$

where $\mathcal{N}$ is a normalization, and we have indexed the states to reflect the periodicity of the lattice. The matrix elements of the operators in the Hamiltonian are given by,

$$\langle n',q'|\frac{\hbar}{i}\hat{D}_z|n,q\rangle = \delta_{nn'}\delta_{kk'}\hbar(2kn+q), \tag{A.39}$$

$$\langle n',q'|\frac{-\hbar^2}{2m}\hat{D}_z^2|n,q\rangle = \delta_{nn'}\delta_{qq'}\frac{(\hbar(2kn+q))^2}{2m}, \tag{A.40}$$

$$\langle n',q'|\cos(2kz)|n,q\rangle = \frac{V_0}{4}\delta_{qq'}(\delta_{n,n'+1}+\delta_{n,n'-1}). \tag{A.41}$$

Thus,

$$\langle n'k'|\hat{H}|nk\rangle = \frac{(\hbar(2kn+q))^2}{2m}\delta_{kk'}\delta_{nn'} + \frac{V_0}{4}\delta_{kk'}(\delta_{n,n'+1}+\delta_{n,n'-1}). \tag{A.42}$$

This matrix is block-diagonal in the quasi-momentum $q$. However, $n$ can be any integer, so this is still an infinite-dimensional matrix. To get around this, we note that the harmonic trapping term arising from the kinetic energy allows us to truncate the basis for low-energy states.

Finally, if we scale energies, momenta, and positions as we did in previous sections, and we apply periodic boundary conditions to get an $N$-site lattice, the matrix elements of the Hamiltonian become

$$\langle n'm'|\hat{H}|nm\rangle = \left(\frac{2}{N}(Nn+m)\right)^2 \delta_{mm'}\delta_{nn'} + \frac{v_0}{4}\delta_{mm'}(\delta_{n,n'+1} + \delta_{n,n'-1}), \tag{A.43}$$

where

$$m = \frac{N}{2}\frac{q}{k} = 0, \ldots, N-1, \tag{A.44}$$

$$\mathcal{N} = \frac{1}{\sqrt{N\pi}}, \tag{A.45}$$

$$v_0 = \frac{V_0}{E_R}. \tag{A.46}$$

The eigenstates can be written as

$$\psi_{p,q}(z) = \langle z|\psi_{p,q}\rangle = \sum_{n\in\mathbb{Z}} \psi_n^{(p,q)}\langle z|n,q\rangle = \sum_{n\in\mathbb{Z}} \psi_n^{(p,q)}\mathcal{N}e^{i(2kn+q)z}, \tag{A.47}$$

or

$$\psi_{p,m}(z) = \sum_{n=n_{\min}}^{n_{\max}} \psi_n^{(m,q)}\frac{1}{\sqrt{N\pi}}e^{i2(Nn+m)z/N}, \tag{A.48}$$

where $p$ is a band-index, and $\psi_n^{(p,m)}$ are the coefficients of the eigenvectors of the matrix defined by equation A.43.

#### A.1.2.1 Bose-Hubbard parameters

We can compute Bose-Hubbard (BH) parameters as a function of lattice depth using the numerical solutions just derived. Since the definition of the Wannier functions used in the BH derivation depends on the relative phases between Bloch functions, we need to be careful about how the coefficients, $\psi_n^{(p,m)}$, are defined. Luckily, the matrix

defined by equation A.43 is real symmetric, which means the eigenvectors can be chosen to purely real. We then need only worry about an overall minus sign.

With that caveat in hand, we suppose that the coefficients are such that the functions

$$w_j^{(p)}(z) = \frac{1}{\sqrt{N}} \sum_{m=0}^{N-1} e^{i2\pi mj/N} \psi_{p,m}(z) \tag{A.49}$$

are the Wannier functions in band $p$. Then, the hopping parameter is

$$\begin{aligned} -J^{(p)} &= \langle w_j^{(p)} | \hat{H} | w_{j+1}^{(p)} \rangle & \text{(A.50)} \\ &= \frac{1}{N} \sum_{m,m'=0}^{N-1} e^{i2\pi m(j+1)/N} e^{-i2\pi m'j/N} \langle \psi_{p,m'} | \hat{H} | \psi_{p,m} \rangle \\ &= \frac{1}{N} \sum_{m,m'=0}^{N-1} e^{i2\pi m(j+1)/N} e^{-i2\pi m'j/N} E_{p,m} \langle \psi_{p,m'} | \psi_{p,m} \rangle \\ &= \frac{1}{N} \sum_{m=0}^{N-1} e^{i2\pi m/N} E_{p,m}. & \text{(A.51)} \end{aligned}$$

Similarly, the on-site energy is

$$\epsilon^{(p)} = \frac{1}{N} \sum_{m=0}^{N-1} E_{p,m}. \tag{A.52}$$

The parameters used in chapter 6 for $p = 1$ and $2k_{\mathrm{C}} = k2(Nr + l)/N$ are given by

$$\begin{aligned} f_{j',j}(k) &= \langle w'_j | e^{i2(Nr+l)\hat{z}/N} | w_j \rangle & \text{(A.53)} \\ &= \frac{1}{N} \sum_{m,m'=0}^{N-1} e^{i2\pi(mj-m'j')/N} \langle \psi_{m'} | e^{i2(Nr+l)\hat{z}/N} | \psi_m \rangle \\ &= \frac{1}{N} \sum_{m,m'=0}^{N-1} e^{i2\pi(mj-m'j')/N} \sum_{s,s'} \psi_{s'}^{(m')*} \psi_s^{(m)} \langle s', m' | e^{i2(Nr+l)\hat{z}/N} | s, m \rangle \\ &= \frac{1}{N} \sum_{m=0}^{N-1} e^{i2\pi(mj-(m+l)j')/N} \sum_{s} \psi_{s+r}^{(m+l)*} \psi_s^{(m)}. & \text{(A.54)} \end{aligned}$$

### A.1.3 Hard-core boson approximation

Here we make explicit the two-state approximation from chapter 3. We write the states as

$$|l; \{n_k\}\rangle = |\ldots, l + n_{k-1}, l + n_k, l + n_{k+1}, \ldots\rangle, \tag{A.55}$$

where $n_j \in \{0, 1\}$ and stipulate the following conditions:

$$\hat{a}_j|l; \{n_k : n_j = 0\}\rangle = 0, \tag{A.56a}$$

$$\hat{a}_j|l; \{n_k : n_j = 1\}\rangle = \sqrt{l+1}|l; \{n_k : n_j = 0\}\rangle, \tag{A.56b}$$

$$\hat{a}_j^\dagger|l; \{n_k : n_j = 1\}\rangle = 0, \tag{A.56c}$$

$$\hat{a}_j^\dagger|l; \{n_k : n_j = 0\}\rangle = \sqrt{l+1}|l; \{n_k : n_j = 1\}\rangle, \tag{A.56d}$$

$$\hat{a}_j^\dagger\hat{a}_j|l; \{n_k : n_j = 0\}\rangle = l|l; \{n_k : n_j = 0\}\rangle, \tag{A.56e}$$

$$\hat{a}_j^\dagger\hat{a}_j|l; \{n_k : n_j = 0\}\rangle = (l+1)|l; \{n_k : n_j = 0\}\rangle. \tag{A.56f}$$

These conditions imply that the action of the hopping terms is given by

$$\hat{a}_j^\dagger\hat{a}_{j\pm1}|l; \{n_k : n_j = 0, n_{j\pm1} = 1\}\rangle = (l+1)|l; \{n_k : n_j = 1, n_{j\pm1} = 0\}\rangle, \tag{A.57}$$

with all other terms such as $\hat{a}_j^\dagger\hat{a}_{j\pm1}|l; \{n_k : n_j = 0, n_{j\pm1} = 0\}\rangle$ equal to zero.

We define new operators $\hat{b}_j$ that are related to the old ones via

$$\hat{b}_j = \frac{\hat{a}_j}{\sqrt{l+1}}, \tag{A.58}$$

$$\hat{b}_j^\dagger\hat{b}_j = \hat{a}_j^\dagger\hat{a}_j - l. \tag{A.59}$$

The relations above imply that the site-number and hopping operators are given by

$$\hat{a}_j^\dagger\hat{a}_j = \hat{b}_j^\dagger\hat{b}_j + l, \tag{A.60a}$$

$$\hat{a}_j^\dagger\hat{a}_{j\pm1} = (l+1)\hat{b}_j^\dagger\hat{b}_{j\pm1}, \tag{A.60b}$$

and that these operators satisfy the relations,

$$\left[\hat{b}_j, \hat{b}_j^\dagger\right]_+ = 1, \tag{A.61a}$$

$$\left[\hat{b}_j, \hat{b}_j\right]_- = 0, \tag{A.61b}$$

$$\left[\hat{b}_{i\neq j}, \hat{b}_j^\dagger\right]_- = 0. \tag{A.61c}$$

The particles apparently have boson-like properties except for the fact that no more than one particle can occupy a single site, which is enforced by equation A.61a. Finally,

we use equation (A.61a) to re-write the interaction term as

$$\begin{aligned}\frac{U}{2}\sum_{j=1}^{N}\hat{a}_j^\dagger\hat{a}_j\left(\hat{a}_j^\dagger\hat{a}_j-1\right) &= \frac{U}{2}\sum_{j=1}^{N}\left(\hat{b}_j^\dagger\hat{b}_j+l\right)\left(\hat{b}_j^\dagger\hat{b}_j+l-1\right)\\ &= \frac{U}{2}\sum_{j=1}^{N}\hat{b}_j^\dagger\left(1-\hat{b}_j^\dagger\hat{b}_j\right)\hat{b}_j\\ &\quad+\frac{U}{2}\sum_{j=1}^{N}\left(l\hat{b}_j^\dagger\hat{b}_j+(l-1)\hat{b}_j^\dagger\hat{b}_j\right)+\frac{U}{2}\sum_{j=1}^{N}l(l-1)\\ &= Ul\sum_{j=1}^{N}\hat{b}_j^\dagger\hat{b}_j+U\frac{1}{2}Nl(l-1).\end{aligned} \tag{A.62}$$

### A.1.4 Jordan-Wigner fermions

To do this we need the following properties. The operator $\hat{b}_k^\dagger\hat{b}_k$ is either zero or one, so

$$e^{i\pi\hat{b}_k^\dagger\hat{b}_k}=e^{-i\pi\hat{b}_k^\dagger\hat{b}_k}=\left(e^{i\pi\hat{b}_k^\dagger\hat{b}_k}\right)^\dagger. \tag{A.63}$$

In addition, since the site-number operators commute, we can combine these exponentials as

$$e^{i\pi\sum_{k<m}\hat{b}_k^\dagger\hat{b}_k}e^{i\pi\sum_{l<n}\hat{b}_l^\dagger\hat{b}_l}=e^{i\pi\sum_{k<m}\hat{b}_k^\dagger\hat{b}_k+i\pi\sum_{l<n}\hat{b}_l^\dagger\hat{b}_l}. \tag{A.64}$$

Finally, since

$$\begin{aligned}\left[\hat{b}_{k\neq j},\hat{b}_j\right]&=0,\\ \hat{b}_j^2&=0, &\text{(A.65)}\\ \hat{b}_j\hat{b}_j^\dagger\hat{b}_j=\left(1-\hat{b}_j^\dagger\hat{b}_j\right)\hat{b}_j&=\hat{b}_j, &\text{(A.66)}\end{aligned}$$

we have that

$$e^{i\pi\hat{b}_j^\dagger\hat{b}_j}\hat{b}_{j\neq k}=\hat{b}_{j\neq k}e^{i\pi\hat{b}_j^\dagger\hat{b}_j}, \tag{A.67a}$$

$$e^{i\pi\hat{b}_j^\dagger\hat{b}_j}\hat{b}_j=\sum_{n=0}^{\infty}\frac{(i\pi)^n}{n!}\left(\hat{b}_j^\dagger\hat{b}_j\right)^n\hat{b}_j=\sum_{n=0}^{\infty}\frac{(i\pi)^n}{n!}\delta_{n,0}\left(\hat{b}_j^\dagger\hat{b}_j\right)^n\hat{b}_j=\hat{b}_j, \tag{A.67b}$$

$$\hat{b}_je^{i\pi\hat{b}_j^\dagger\hat{b}_j}=\sum_{n=0}^{\infty}\frac{(i\pi)^n}{n!}\hat{b}_j\left(\hat{b}_j^\dagger\hat{b}_j\right)^n=\sum_{n=0}^{\infty}\frac{(i\pi)^n}{n!}\hat{b}_j=e^{i\pi}\hat{b}_j=-\hat{b}_j. \tag{A.67c}$$

These three conditions imply the relations,

$$\left[\hat{b}_{j\neq k}, e^{i\pi\hat{b}_j^\dagger\hat{b}_j}\right]_- = 0, \tag{A.68}$$

$$\left[\hat{b}_j, e^{i\pi\hat{b}_j^\dagger\hat{b}_j}\right]_+ = 0. \tag{A.69}$$

With these relations in hand, we can show that the $\hat{c}_j$ operators are fermionic. First,

$$\begin{aligned}\left[\hat{c}_j, \hat{c}_j^\dagger\right]_+ &= \left[\hat{b}_j e^{i\pi\sum_{k<j}\hat{b}_k^\dagger\hat{b}_k}, e^{-i\pi\sum_{k<j}\hat{b}_k^\dagger\hat{b}_k}\hat{b}_j^\dagger\right]_+ \\ &= \left[\hat{b}_j, \hat{b}_j^\dagger\right]_+ e^{i\pi\sum_{k<j}\hat{b}_k^\dagger\hat{b}_k}e^{-i\pi\sum_{k<j}\hat{b}_k^\dagger\hat{b}_k} \\ &= \left[\hat{b}_j, \hat{b}_j^\dagger\right]_+ = 1.\end{aligned} \tag{A.70}$$

Second,

$$\begin{aligned}[\hat{c}_{j<l}, \hat{c}_l]_+ &= \left[\hat{b}_j e^{i\pi\sum_{k<j}\hat{b}_k^\dagger\hat{b}_k}, e^{-i\pi\sum_{i<l}\hat{b}_i^\dagger\hat{b}_i}\hat{b}_l^\dagger\right]_+ \\ &= \left[\hat{b}_j, e^{-i\pi\hat{b}_j^\dagger\hat{b}_j}\right]_+ \hat{b}_l^\dagger e^{-i\pi\sum_{n<j}\hat{b}_n^\dagger\hat{b}_n}e^{-i\pi\sum_{j<i<l}\hat{b}_i^\dagger\hat{b}_i}e^{i\pi\sum_{k<j}\hat{b}_k^\dagger\hat{b}_k} \\ &= 0.\end{aligned} \tag{A.71}$$

The same computation goes through for $\left[\hat{c}_{j<l}, \hat{c}_l^\dagger\right]_+$, since owing to

$$e^{i\pi\sum_{k<j}\hat{b}_k^\dagger\hat{b}_k} = e^{-i\pi\sum_{k<j}\hat{b}_k^\dagger\hat{b}_k}, \tag{A.72}$$

the only difference is the substitution $\hat{b}_l \to \hat{b}_l^\dagger$. Finally,

$$\begin{aligned}[\hat{c}_N, \hat{c}_1]_+ &= \left[\hat{b}_N e^{i\pi\sum_{k=1}^{N-1}\hat{b}_k^\dagger\hat{b}_k}, \hat{b}_1^\dagger\right]_+ = \hat{b}_N e^{i\pi\sum_{k=1}^{N-1}\hat{b}_k^\dagger\hat{b}_k}\left[e^{i\pi\hat{b}_1^\dagger\hat{b}_1}, \hat{b}_1^\dagger\right]_+ \\ &= 0.\end{aligned} \tag{A.73}$$

Summarizing, we have derived the anti-commutation relations,

$$\left[\hat{c}_j, \hat{c}_j^\dagger\right]_+ = \delta_{ij}, \tag{A.74}$$

$$[\hat{c}_j, \hat{c}_l]_+ = 0, \tag{A.75}$$

which implies that the $\hat{c}$'s are fermionic operators.

Now, this transformation is only really useful if the resulting transformed Hamiltonian is quadratic in these operators, since in this case it is known that the excitations are then fermionic. We need to verify that the exponential factors cancel out. First, we note that the site-number operators are given by

$$\hat{c}_j^\dagger \hat{c}_j = \hat{b}_j^\dagger e^{-i\pi \sum_{k<j} \hat{b}_k^\dagger \hat{b}_k} e^{i\pi \sum_{k<j} \hat{b}_k^\dagger \hat{b}_k} \hat{b}_j = \hat{b}_j^\dagger \hat{b}_j. \tag{A.76}$$

This allows us to easily invert the JW transformation as

$$\hat{b}_j = \hat{c}_j e^{i\pi \sum_{k<j} \hat{c}_k^\dagger \hat{c}_k}. \tag{A.77}$$

Equation A.67 also holds for $\hat{c}_j$.

The hopping terms become

$$\begin{aligned} \hat{b}_{j\leq N}^\dagger \hat{b}_{j+1} &= \hat{c}_j^\dagger e^{-i\pi \sum_{k<j} \hat{c}_k^\dagger \hat{c}_k} e^{i\pi \sum_{k<j+1} \hat{c}_k^\dagger \hat{c}_k} \hat{c}_{j+1} = \hat{c}_j^\dagger e^{i\pi \hat{c}_j^\dagger \hat{c}_j} \hat{c}_{j+1} \\ &= \hat{c}_j^\dagger \hat{c}_{j+1}, \end{aligned} \tag{A.78}$$

and

$$\begin{aligned} \hat{b}_N^\dagger \hat{b}_1 &= \hat{c}_N^\dagger e^{-i\pi \sum_{k=1}^{N-1} \hat{c}_k^\dagger \hat{c}_k} \hat{c}_1 = \hat{c}_N^\dagger e^{i\pi \hat{c}_N^\dagger \hat{c}_N} e^{-i\pi \hat{c}_N^\dagger \hat{c}_N} e^{-i\pi \hat{c}_1^\dagger \hat{c}_1} \hat{c}_1 e^{-i\pi \sum_{k=2}^{N-1} \hat{c}_k^\dagger \hat{c}_k} \\ &= \hat{c}_N^\dagger e^{i\pi \hat{c}_N^\dagger \hat{c}_N} e^{-i\pi \hat{c}_1^\dagger \hat{c}_1} \hat{c}_1 e^{i\pi \hat{c}_1^\dagger \hat{c}_1} e^{-i\pi \hat{c}_1^\dagger \hat{c}_1} e^{-i\pi \sum_{k=2}^{N-1} \hat{c}_k^\dagger \hat{c}_k} e^{-i\pi \hat{c}_N^\dagger \hat{c}_N} \\ &= \hat{c}_N^\dagger (-\hat{c}_1) e^{-i\pi \hat{N}} \\ &= \hat{c}_N^\dagger \hat{c}_1 (-1)^{\hat{N}+1}, \end{aligned} \tag{A.79}$$

where

$$\hat{N} = \sum_{k=1}^{N} \hat{b}_k^\dagger \hat{b}_k = \sum_{k=1}^{N} \hat{c}_k^\dagger \hat{c}_k \tag{A.80}$$

is the total number of particles minus $Nl$. The Hamiltonian can then be written as

$$\begin{aligned} \hat{H} = U\frac{1}{2}Nl(l-1) + Ul \sum_{j=1}^{N} \hat{c}_j^\dagger \hat{c}_j + \sum_{j=1}^{N} \epsilon(\omega) \hat{c}_j^\dagger \hat{c}_j \\ - t(l+1) \sum_{j=1}^{N-1} e^{-i\pi\omega N/4} \hat{c}_j^\dagger \hat{c}_{j+1} + \text{H.c.} \\ - t(l+1) e^{-i\pi\omega N/4} \hat{c}_N^\dagger \hat{c}_1 (-1)^{\hat{N}+1} + \text{H.c.} \end{aligned} \tag{A.81}$$

## A.2 Tilted Lattice Problem

### A.2.1 Dipole subspace Hamiltonian

We first prove by induction that the number of states in the $M$-dipole subspace for a $N$-site lattice is given by the expression,

$$n_M = \binom{N-M}{M}. \tag{A.82}$$

For $M = 0$, this formula yields 1: there is exactly one MI state. For $M = 1$, this formula yields $N - 1$, which is clearly the exact number of one-dipole states. We can count the number of $M = 2$ states by taking all of the $M = 1$ states and adding an extra dipole. To avoid double-counting, we only add dipoles to the left of the existing dipole in the one-dipole subspace. There are $N - 3$ two-dipole states that we can make from $|1; N-1\rangle$ since by having a dipole between sites $N-1$ and $N$, we have effectively removed 2 sites from the lattice. There are $N - 4$ two-dipole states that we can make from $|1; N-2\rangle$, by the same argument. We can do the same thing until we reach the state $|1; 3\rangle$ which accommodates exactly one dipole to the left of site 3. Thus, the number of states is in the two-dipole subspace is

$$n_2 = \sum_{j=3}^{N-1}(N-j) = \sum_{n=1}^{N-3} n = \frac{1}{2}(N-3)(N-2) = \binom{N-2}{2}. \tag{A.83}$$

In general, we consider the subspace spanned by the vectors,

$$|M+1; k_{M+1}, k_M, \ldots, k_1\rangle = \frac{1}{\sqrt{2^M}} \prod_{i=1}^{M+1} \hat{b}^\dagger_{k_i} \hat{b}_{k_i+1} |\psi_{MI}\rangle : \begin{array}{r} k_i = 2i-1, \ldots, k_{i+1}-2 \\ k_M = 2M-1, \ldots, k_{M+1}-2 \\ k_{M+1} = 2M+1, \ldots, N-1 \end{array}, \tag{A.84}$$

for some $2 \leq M \leq \lfloor N/2 \rfloor$. We choose a specific $k_{M+1}$; this effectively reduces the lattice for the remaining dipoles to be of size $k_{M+1} - 1$, since we have a dipole between sites $k_{M+1}$ and $k_{M+1} + 1$. By inductive assumption, there are

$$n_{k_{M+1}} = \binom{k_{M+1}-1-M}{M} \tag{A.85}$$

ways of fitting $M$ dipoles on a lattice of with $k_{M+1}-1$ sites. Letting $k_{M+1}$ vary between $2M+1$ and $N-1$, we can count the total number of states as

$$n_{M+1} = \sum_{k_{M+1}=2M+1}^{N-1} n_{k_{M+1}} = \sum_{k_{M+1}=2M+1}^{N-1} \binom{k_{M+1}-1-M}{M} = \sum_{k=0}^{N-2M-2} \binom{k+M}{M}. \tag{A.86}$$

With repeated uses of the identity,

$$\binom{x+y}{x} = \binom{x+y-1}{x-1} + \binom{x+y-1}{x}. \tag{A.87}$$

it is easy to show that

$$\binom{N-(M+1)}{M+1} = \sum_{k=0}^{N-2M-2} \binom{k+M}{M}, \tag{A.88}$$

and the inductive proof is finished.

This proof also gives us a way to enumerate the states in each dipole subspace. We label the state $|M; k_M, \ldots, k_1\rangle$ as

$$n_{k_M,\ldots,k_1} = 1 + \sum_{m=1}^{M} \binom{k_m - m}{m} : \begin{array}{c} k_i = 2i-1, \ldots, k_{i+1}-2 \\ k_M = 2M-1, \ldots, N-1 \end{array}. \tag{A.89}$$

This enumerates the states in order from 1 to $\binom{N-M}{M}$. Finally, then, we can write down an effective Hamiltonian that includes only the dipole subspaces. The state $|M+1; k_{M+1}, \ldots, k_1\rangle$ is connected to the states $|M; l_M, \ldots, l_1\rangle$ where we have simply removed one of the $k_i$'s. In terms of the indices, the state labeled by

$$n_{k_{M+1},\ldots,k_1} = 1 + \sum_{m=1}^{M+1} \binom{k_m - m}{m} \tag{A.90}$$

in the $(M+1)$-dipole subspace is connected to the states labeled by

$$n_{k_{M+1},\ldots,k_{n+1},k_{n-1},\ldots,k_1} = 1 + \sum_{m=1}^{n-1} \binom{k_m - m}{m} + 1 + \sum_{m=n}^{M} \binom{k_{m+1} - m}{m} \tag{A.91}$$

in the $M$-dipole subspace. Since this connection implies a particle hopping onto an already occupied site, we get an extra factor of $\sqrt{2}$ due to the bosonic nature of the particles.

### A.2.2 Symmetric Hamiltonian

For the purposes of analyzing the dynamics and the detection scheme, we need to know how to numerically implement the quadratic operators, $\hat{b}_j^\dagger \hat{b}_j$ and $\hat{b}_{j+1}^\dagger \hat{b}_j$. We first note that

$$\hat{b}_j^\dagger \hat{b}_j \to \sum_{M=0}^{\lfloor N/2 \rfloor} |M\rangle\langle M|\hat{b}_j^\dagger \hat{b}_j|M\rangle\langle M|, \tag{A.92}$$

$$\hat{b}_{j+1}^\dagger \hat{b}_j \to \sum_{M=1}^{\lfloor N/2 \rfloor} |M-1\rangle\langle M-1|\hat{b}_{j+1}^\dagger \hat{b}_j|M\rangle\langle M|. \tag{A.93}$$

Investigating $\hat{b}_{j+1}^\dagger \hat{b}_j$ first, we can see that

$$\langle M-1|\hat{b}_{j+1}^\dagger \hat{b}_j|M\rangle = \frac{1}{\sqrt{n_M n_{M-1}}} \sum_{k_M,\ldots,k_1} \sum_{l_{M-1},\ldots,l_1} \times \langle M-1; l_{M-1},\ldots,l_1|\hat{b}_{j+1}^\dagger \hat{b}_j|M; k_M,\ldots,k_1\rangle. \tag{A.94}$$

The innermost matrix element is non-zero and equal to $\sqrt{2}$ exactly when $k_n = j$ for some $n$ and $\{l_{M-1},\ldots,l_1\} = \{k_M,\ldots,k_1\}\backslash\{k_n\}$. Equivalently, we count the number of $M$-dipole states that have a dipole between sites $j$ and $j+1$. By removing this dipole, we generate all of the $(M-1)$-dipole states that are coupled to the $M$ subspace via $\hat{b}_{j+1}^\dagger \hat{b}_j$. The matrix element is then equal to

$$\langle M-1|\hat{b}_{j+1}^\dagger \hat{b}_j|M\rangle = \sqrt{\frac{2}{n_M n_{M-1}}} \times (\#\text{ of } M\text{-dipole states with dipole at } j \text{ and } j+1). \tag{A.95}$$

To compute this coupling, we fix $j$, $N$, and $M$, and count the total number of ways we can put $M-1$ dipoles in the remaining sites. There are $j-1$ sites to the left of $j$. There are $N-j-1$ sites to the right of site $j+1$. If we let $m$ be the number of dipoles to the left of site $j$ in a particular configuration, then there are $M-1-m$ dipoles to the right of site $j+1$. The total number of configurations is equal to the product of the number of ways we can fit $m$ dipoles in $j-1$ sites times the number of

ways we can fit $M-m-1$ dipoles in $N-j-1$ sites. This is

$$n_m^{(M;j)} = \binom{j-1-m}{m}\binom{N-j-1-(M-m-1)}{M-m-1}. \tag{A.96}$$

Summing over $m$ will give us the quantity we are seeking. The maximum number of dipoles that we can fit in $N-j-1$ sites is $\lfloor (N-j-1)/2 \rfloor$. Thus, the minimum number of dipoles we need to put to the left of site $j$ is $\max(0, M-1-\lfloor (N-j-1)/2 \rfloor)$. This ensures that we do not attempt to cram too many dipoles to the right of site $j+1$. Similarly, the maximum number of dipoles that we can fit in $j-1$ sites is $\lfloor (j-1)/2 \rfloor$. This cannot be bigger than $M-1$; the largest $m$ can be is then $\min(M-1, \lfloor (j-1)/2 \rfloor)$. With all of this in hand, the total number of $M$-dipole states with a dipole between sites $j$ and $j+1$ is

$$n_j^{(M)} = \sum_{m=\max(0,M-1-\lfloor (N-j-1)/2 \rfloor)}^{\min(M-1,\lfloor (j-1)/2 \rfloor)} \binom{j-1-m}{m}\binom{N-j-1-(M-m-1)}{M-m-1}. \tag{A.97}$$

Thus, in the restricted basis, we can write

$$\hat{b}_{j+1}^\dagger \hat{b}_j \to \sum_{M=1}^{\lfloor N/2 \rfloor} \sqrt{\frac{2}{n_{M-1} n_M}}\, n_j^{(M)} |M-1\rangle\langle M|. \tag{A.98}$$

For the computation of $\hat{b}_j^\dagger \hat{b}_j$, we fix again fix $j$, $N$, and $M$. The total number of states with two particles at site $j$ is exactly $n_j^{(M)}$. The total number of states with zero particles at site $j$ is the same as the total number of states, $n_{j-1}^{(M)}$, with two particles at site $j-1$. Here, $n_N^{(M)}$ and $n_0^{(M)}$ are understood to be zero. The total number of states with one particle at site $j$ is $n_M - n_j^{(M)} - n_{j-1}^{(M)}$. The average number of particles on site $j$ within the $M$-dipole subspace is then

$$\begin{aligned}\langle M|\hat{b}_j^\dagger \hat{b}_j|M\rangle &= \frac{(1)(n_M - n_j^{(M)} - n_{j-1}^{(M)}) + (2)(n_j^{(M)}) + (0)(n_{j-1}^{(M)})}{n_M} \\ &= \frac{n_M + n_j^{(M)} - n_{j-1}^{(M)}}{n_M}.\end{aligned} \tag{A.99}$$

# Appendix B

## Atoms Interacting with Quantized Fields

The description of atoms interacting with quantized light-fields relies heavily on the material in references [30, 63, 71, 77, 88].

For simplicity, we here consider the interaction of a hydrogen atom with an external electromagnetic field. The generalization to other one-electron atoms is straightforward since the energy levels can be treated via quantum-defect theory, and the sizes of the atoms are all much smaller than the wavelength of optical light. The Hamiltonian for a hydrogen atom interacting with an electromagnetic field is given by the minimal substitution, taking the form,

$$H\left(\mathbf{r}_{\mathrm{e}},\mathbf{r}_{\mathrm{p}};\mathbf{p}_{\mathrm{e}},\mathbf{p}_{\mathrm{p}}\right)=\frac{1}{2m_{\mathrm{p}}}\left(\mathbf{p}_{\mathrm{p}}-e\mathbf{A}\left(\mathbf{r}_{\mathrm{p}}\right)\right)^{2}+\frac{1}{2m_{\mathrm{e}}}\left(\mathbf{p}_{\mathrm{e}}+e\mathbf{A}\left(\mathbf{r}_{\mathrm{e}}\right)\right)^{2}+V\left(\left|\mathbf{r}_{\mathrm{e}}-\mathbf{r}_{\mathrm{p}}\right|\right)+H_{\mathrm{EM}}, \tag{B.1}$$

where the first two terms are the Hamiltonians for the nucleus and the electron, respectively, $V$ is the Coulomb interaction between electron and nucleus, and $H_{\mathrm{EM}}$ is the Hamiltonian of the free electromagnetic field. We work in the Coulomb gauge, where

$$\nabla_{x}\cdot\mathbf{A}\left(\mathbf{x}\right)\psi\left(\mathbf{x}\right)=\mathbf{A}\left(\mathbf{x}\right)\cdot\nabla_{x}\psi\left(\mathbf{x}\right)-\left[\nabla_{x}\cdot\mathbf{A}\left(\mathbf{x}\right)\right]\psi\left(\mathbf{x}\right)=\mathbf{A}\left(\mathbf{x}\right)\cdot\nabla_{x}\psi\left(\mathbf{x}\right), \tag{B.2}$$

and we move to center-of-mass coordinates,

$$\mathbf{R}=\frac{m_{\mathrm{p}}\mathbf{r}_{\mathrm{p}}+m_{\mathrm{e}}\mathbf{r}_{\mathrm{e}}}{m_{\mathrm{p}}+m_{\mathrm{e}}}, \tag{B.3}$$

$$\mathbf{r}=\mathbf{r}_{\mathrm{e}}-\mathbf{r}_{\mathrm{p}}. \tag{B.4}$$

In this case, the Hamiltonian becomes

$$\begin{aligned} H\left(\mathbf{R},\mathbf{r}\right) = & -\frac{\hbar^2}{2M}\nabla_R^2 - \frac{\hbar^2}{2\mu}\nabla_r^2 + V\left(r\right) + H_{\mathrm{EM}} \\ & - \frac{\hbar}{i}\frac{e}{m_{\mathrm{p}}}\mathbf{A}\left(\mathbf{R} - \frac{m_{\mathrm{p}}}{\mu}\mathbf{r}\right)\cdot\left(\frac{m_{\mathrm{e}}}{\mu}\nabla_R - \nabla_r\right) \\ & + \frac{\hbar}{i}\frac{e}{m_{\mathrm{e}}}\mathbf{A}\left(\mathbf{R} + \frac{m_{\mathrm{e}}}{\mu}\mathbf{r}\right)\cdot\left(\frac{m_{\mathrm{p}}}{\mu}\nabla_R + \nabla_r\right) \\ & + \frac{e^2}{2m_{\mathrm{p}}}A^2\left(\mathbf{R} - \frac{m_{\mathrm{p}}}{\mu}\mathbf{r}\right) + \frac{e^2}{2m_{\mathrm{e}}}A^2\left(\mathbf{R} + \frac{m_{\mathrm{e}}}{\mu}\mathbf{r}\right). \end{aligned} \tag{B.5}$$

where

$$\mu = \frac{m_{\mathrm{p}}m_{\mathrm{e}}}{m_{\mathrm{p}} + m_{\mathrm{e}}}, \tag{B.6}$$

$$M = m_{\mathrm{p}} + m_{\mathrm{e}}, \tag{B.7}$$

are respectively the reduced mass and the total mass of the atom.

Wavelengths of optical fields are typically on the order of hundreds of nanometers, roughly one hundred times the size of the atom. The electric fields do not appreciably vary in the region over which the wave-function of the atom is non-zero. We can then make the dipole approximation, which at this point amounts to making the replacement,

$$\mathbf{A}\left(\mathbf{R} - \frac{m_{\mathrm{p}}}{\mu}\mathbf{r}\right), \mathbf{A}\left(\mathbf{R} + \frac{m_{\mathrm{e}}}{\mu}\mathbf{r}\right) \rightarrow \mathbf{A}\left(\mathbf{R}\right). \tag{B.8}$$

The Hamiltonian becomes

$$\begin{aligned} H(\mathbf{R},\mathbf{r}) &= H_{\mathrm{COM}}\left(\mathbf{R}\right) + \hat{H}_{\mathrm{A}} + H_{\mathrm{int}}\left(\mathbf{r}\right) + H_2 + H_{\mathrm{EM}} \\ &= -\frac{\hbar^2}{2M}\nabla_R^2 - \frac{\hbar^2}{2m}\nabla_r^2 + V\left(r\right) + \frac{\hbar}{i}\frac{e}{\mu}\mathbf{A}\left(\mathbf{R}\right)\cdot\nabla_r + \frac{e^2}{2\mu}A^2\left(\mathbf{R}\right) + H_{\mathrm{EM}}. \end{aligned} \tag{B.9}$$

For many atoms interacting with the electromagnetic field, we define field operators $\hat{\Phi}\left(\mathbf{R},\mathbf{r}\right)$ – which may be bosonic or fermionic – and write the Hamiltonian as

$$\hat{H} = \int d^3R \int d^3r \hat{\Phi}^{\dagger}\left(\mathbf{R},\mathbf{r}\right) H\left(\mathbf{R},\mathbf{r}\right) \hat{\Phi}\left(\mathbf{R},\mathbf{r}\right). \tag{B.10}$$

The field operator can be expanded in single-particle eigenfunctions as

$$\hat{\Phi}\left(\mathbf{R},\mathbf{r}\right) = \sum_{m,n} \hat{c}_{mn}\psi_n\left(\mathbf{R}\right)\varphi_m\left(\mathbf{r}\right),$$

where $\{\psi_n(\mathbf{R})\}$ and $\{\varphi_m(\mathbf{r})\}$ are respectively diagonalize $H_{\mathrm{COM}}$ and $H_{\mathrm{int}}$.

Defining

$$\hat{\Psi}_m(\mathbf{R}) = \sum_n \hat{c}_{mn}\psi_n^R(\mathbf{R}), \tag{B.11}$$

the various pieces of the Hamiltonian can be written as

$$\hat{H}_{\mathrm{A}} = -\frac{\hbar^2}{2M}\sum_m \int d^3R\hat{\Psi}_m^\dagger(\mathbf{R})\nabla_R^2\hat{\Psi}_m(\mathbf{R}) + \sum_m E_m \int d^3R\hat{\Psi}_m^\dagger(\mathbf{R})\hat{\Psi}_m(\mathbf{R}), \tag{B.12a}$$

$$\hat{H}_{\mathrm{int}} = \sum_{m,m'}\int d^3R\hat{\Psi}_{m'}^\dagger(\mathbf{R})\mathbf{A}(\mathbf{R})\hat{\Psi}_m(\mathbf{R})\cdot\left(\frac{e}{\mu}\int\varphi_{m'}^*(\mathbf{r})\mathbf{p}_r\varphi_m(\mathbf{r})d^3r\right), \tag{B.12b}$$

$$H_2 = \frac{e^2}{2\mu}\sum_m\int d^3R\hat{\Psi}_m^\dagger(\mathbf{R})A^2(\mathbf{R})\hat{\Psi}_m(\mathbf{R}), \tag{B.12c}$$

where $E_m$ is the eneregy eigenvalue corresponding to the internal-state wave function, $\langle\mathbf{r}|m\rangle = \varphi_m(\mathbf{r})$.

## B.1 Hamiltonian of the free electromagnetic field

We expand the vector potential, $\mathbf{A}$, in normal modes as

$$\mathbf{A}(\mathbf{x},t) = \sum_{\mathbf{k},\lambda}\sqrt{\frac{\hbar}{2\omega_k\epsilon_0}}\left(a_{\mathbf{k},\lambda}\hat{e}_{\mathbf{k},\lambda}u_{\mathbf{k}}(\mathbf{x})e^{-i\omega_k t} + a_{k,\lambda}^*\hat{e}_{\mathbf{k},\lambda}u_{\mathbf{k}}^*(\mathbf{x})e^{i\omega_k t}\right), \tag{B.13a}$$

$$\omega_k = c|\mathbf{k}| = ck, \tag{B.13b}$$

$$\hat{k}\times\hat{e}_{\mathbf{k},1} = \hat{e}_{\mathbf{k},2}, \hat{k}\times\hat{e}_{\mathbf{k},2} = -\hat{e}_{\mathbf{k},1}, \hat{e}_{\mathbf{k},1}\times\hat{e}_{\mathbf{k},2} = \hat{k}, \tag{B.13c}$$

where

$$\omega_k = c|\mathbf{k}| = ck, \tag{B.14}$$

$\lambda$ indexes two polarization vectors perpendicular to $\mathbf{k}$, and $u_{\mathbf{k}}(\mathbf{x})$ is a complete, orthonormal set of normal modes of the electromagnetic field, satisfying proper boundary conditions and the Helmholtz equation,

$$\left(\nabla^2 + k^2\right)\mathbf{A}(\mathbf{x},t) = 0. \tag{B.15}$$

We promote the expansion coefficients to operators satisfying bosonic commutation relations,

$$\left[\hat{a}_{\mathbf{k}',\lambda'}, \hat{a}^{\dagger}_{\mathbf{k},\lambda}\right] = \delta_{\mathbf{k},\mathbf{k}'}\delta_{\lambda\lambda'}, \tag{B.16}$$

$$\left[\hat{a}_{\mathbf{k}',\lambda'}, \hat{a}_{\mathbf{k},\lambda}\right] = 0, \tag{B.17}$$

in which case the free Hamiltonian,

$$E_{\mathrm{EM}} = \frac{1}{2}\int d^3x \left(\epsilon_0 \left|E\right|^2 + \frac{1}{\mu_0}\left|B\right|^2\right), \tag{B.18}$$

can be written as

$$\hat{H}_{\mathrm{EM}} = \sum_{k,\lambda} \hbar\omega_k \left(\hat{a}^{\dagger}_{\mathbf{k},\lambda}\hat{a}_{\mathbf{k},\lambda} + \frac{1}{2}\right). \tag{B.19}$$

The equation of motion for the annihilation operator is

$$i\hbar\frac{d\hat{a}_{\mathbf{k},\lambda}}{dt} = \left[\hat{a}_{\mathbf{k},\lambda}, \hat{H}_{EM}\right] = \hbar\omega_k\hat{a}_{\mathbf{k},\lambda}, \tag{B.20}$$

which implies that

$$\hat{a}_{\mathbf{k},\lambda}(t) = \hat{a}_{\mathbf{k},\lambda}(0)\, e^{-i\omega_k t}. \tag{B.21}$$

The electric field operator is

$$\mathbf{E}(\mathbf{x},t) = -\frac{d\mathbf{A}}{dt} = \sum_{\mathbf{k},\lambda} i\sqrt{\frac{\hbar\omega_k}{2\epsilon_0}}\hat{a}_{\mathbf{k},\lambda}\hat{e}_{\mathbf{k},\lambda}u_{\mathbf{k}}(\mathbf{x})\, e^{-i\omega_k t} + h.c.$$

Equation B.21 tells us that this operator is written in the Heisenberg picture. The Schrödinger picture operator is then given by

$$\mathbf{E}(\mathbf{x}) = \sum_{\mathbf{k},\lambda} i\sqrt{\frac{\hbar\omega_k}{2\epsilon_0}}\hat{a}_{\mathbf{k},\lambda}\hat{e}_{\mathbf{k},\lambda}u_{\mathbf{k}}(\mathbf{x}) + h.c. \tag{B.22}$$

We may make the identification,

$$\mathbf{E}^{(+)}_{\mathbf{k},\lambda} = \hat{E}^{(+)}_{\mathbf{k},\lambda}\hat{e}_{\mathbf{k},\lambda} = i\sqrt{\frac{\hbar\omega_k}{2\epsilon_0}}\hat{a}_{\mathbf{k},\lambda}\hat{e}_{\mathbf{k},\lambda}, \tag{B.23}$$

where $\mathbf{E}^{(+)}_{\mathbf{k},\lambda}$ is the complex amplitude associated with the positive frequency part of mode $(\mathbf{k},\lambda)$. The amplitudes of the electric field an vector potential can be related via

$$\mathbf{A}^{(+)}_{\mathbf{k},\lambda} = \sqrt{\frac{\hbar}{2\epsilon_0\omega_k}}\hat{a}_{\mathbf{k},\lambda}\hat{e}_{\mathbf{k},\lambda} = \frac{1}{i\omega_k}\mathbf{E}^{(+)}_{\mathbf{k},\lambda}. \tag{B.24}$$

## B.2 Optical dipole potential

We can simplify equation (B.12b) considerably in the optical regime by way of the rotating wave approximation. In order to make our way towards implementation of this approximation, we first justify making the (approximate) identification, $\hat{H}_{\text{int}} = -\mathbf{d} \cdot \mathbf{E}$, where $\mathbf{d}$ is the dipole moment of the atoms. The matrix element $\frac{e}{\mu} \langle m' | \mathbf{p}_r | m \rangle$ can be re-written by way of the equation,

$$i\hbar \frac{d\mathbf{r}}{dt} = [\mathbf{r}, H_{\text{int}}(\mathbf{r})] = \frac{i\hbar}{\mu} \mathbf{p}_r, \tag{B.25}$$

as

$$\frac{e}{\mu} \langle m' | \mathbf{p}_r | m \rangle = -ie\omega_{mm'} \langle m' | \mathbf{r} | m \rangle . \tag{B.26}$$

The interaction Hamiltonian can then be written as

$$\hat{H}_{\text{int}} = -\sum_{m,m'} \int d^3R \hat{\Psi}^\dagger_{m'}(\mathbf{R}) \sum_{\mathbf{k},\lambda} e \frac{\omega_{mm'}}{\omega_k} \langle m' | \mathbf{r} \cdot \hat{e}_{\mathbf{k},\lambda} | m \rangle \hat{E}^{(+)}_{\mathbf{k},\lambda} u_{\mathbf{k}}(\mathbf{R}) \hat{\Psi}_m(\mathbf{R}) + H.c. \tag{B.27}$$

Up to the factor of $\frac{\omega_{mm'}}{\omega_k}$, this is exactly $-\mathbf{d} \cdot \mathbf{E}$.

We now suppose that we are dealing with field modes that are nearly resonant with the atomic transition; we will make the term "nearly resonant" more precise below. In addition, the matrix element $\langle m' | \mathbf{r} \cdot \hat{e}_{\mathbf{k},\lambda} | m \rangle$ is zero if $m' = m$ since the eigenstates of $H_\Lambda(\mathbf{r})$ can be chosen to be angular momentum eigenstates, in which case $\mathbf{r}$ does not connect states of the same total angular momentum. Focusing on only two states with $\omega_{m'} > \omega_m$ for the moment, we move into an interaction picture where the free time-dependence of the internal state and the electromagnetic field are made explicit. In this case,

$$\begin{aligned} \hat{H}_{\text{int}} = &-\int d^3R \hat{\Psi}^\dagger_{m'}(\mathbf{R}) e \frac{\omega_{mm'}}{\omega_k} \langle m' | \mathbf{r} \cdot \hat{e}_{\mathbf{k},\lambda} | m \rangle \hat{E}^{(+)}_{\mathbf{k},\lambda} u_{\mathbf{k}}(\mathbf{R}) \hat{\Psi}_m(\mathbf{R}) e^{-i(\omega_k - (\omega_{m'} - \omega_m))t} \\ &+ (m \leftrightarrow m') + H.c. \end{aligned} \tag{B.28}$$

If we enforce the condition,

$$|\Omega_{\mathbf{k},\lambda}^{(m',m)}| \ll |\omega_k + (\omega_{m'} - \omega_m)|, \tag{B.29}$$

$$\frac{\hbar}{2}\Omega_{\mathbf{k},\lambda}^{(m',m)} = -ie\frac{\omega_m - \omega_{m'}}{\omega_k}\sqrt{\frac{\hbar\omega_k}{2\epsilon_0}}\left\langle m'\right|\mathbf{r}\cdot\hat{e}_{\mathbf{k},\lambda}\left|m\right\rangle, \tag{B.30}$$

which is what we mean by nearly resonant and is not very difficult to satisfy for optical frequencies, then we can neglect terms involving $e^{\pm i(\omega_k+(\omega_{m'}-\omega_m))t}$, since they average to zero due to rapid oscillations. The interaction Hamiltonian can be then written as

$$\hat{H}_{\text{int}} = \sum_{m'}\sum_{m(\omega_m<\omega_{m'})}\sum_{\mathbf{k},\lambda}\frac{\hbar}{2}\Omega_{\mathbf{k},\lambda}^{(m',m)}\hat{a}_{\mathbf{k},\lambda}e^{i\delta_k^{(m'm)}t}\int d^3R\hat{\Psi}_{m'}^{\dagger}\left(\mathbf{R}\right)u_{\mathbf{k}}\left(\mathbf{R}\right)\hat{\Psi}_m\left(\mathbf{R}\right) + H.c. \tag{B.31}$$

where

$$\delta_k^{(m',m)} = \omega_{m'} - \omega_m - \omega_k. \tag{B.32}$$

It is important to keep in mind that although equation (B.31) seems to have a sum over all internal states of the atom and all modes of the field, this can obviously not be case. Not only does the condition in equation (B.29) break down for different transitions but the same field mode, but the dipole approximation can also break down if the field frequencies get too high. In this thesis, we consider coherent dynamics only when we have two level atoms and at most two modes of the electromagnetic field. Coupling of atoms to a continuum of free-space modes will be treated through a master equation describing spontaneous emission.

## B.3 Adiabatic elimination of high-lying excited states

There is one final simplification we will make for the atom-field interaction. In the case where the field is far enough detuned from the atomic transition while still satisfying equation (B.29), high-lying excited state can be adiabatically slaved to the lower-lying states. This gives rise to an effective position-dependent Stark shift. Not only does this decouple the internal states of the atom, but it also gives rise to an external sinusoidal potential for the atoms.

In the following, we consider only two atomic states, a ground state and an excited state, and we consider at most only two electromagnetic field modes with the same frequency. We have in mind one of two situations. First, the atoms interact with a single standing-wave mode that is pumped by a laser, and the rest of the modes are treated via a master equation. Second, the atoms interact with two counter-propagating modes of an optical cavity – where the mode are isolated from each other in frequency. In either case, we can make the temporary replacement,

$$\Omega_{\mathbf{k},\lambda}^{(e,g)} \to \Omega; \quad \delta_k^{(eg)} = \delta. \tag{B.33}$$

Finally, we assume that the fields are "far-enough" detuned from the atomic transition. We will make more precise what this means below.

The equation of motion for the high-lying, excited-state field operator is

$$i\hbar \frac{d\hat{\Psi}_e}{dt} = \sum_{\mathbf{k},\lambda} \frac{\hbar\Omega}{2} e^{i\delta t} u_{\mathbf{k}} \hat{a}_{\mathbf{k},\lambda} \hat{\Psi}_g. \tag{B.34}$$

We formally integrate this equation for a time $\tau \ll 1/\delta$, resulting in

$$\begin{aligned}
\hat{\Psi}_e(\tau + t_0) &= \int_{t_0}^{\tau+t_0} dt' \sum_{\mathbf{k},\lambda} \frac{-i\Omega}{2} e^{i\delta t'} u_{\mathbf{k}} \hat{a}_{\mathbf{k},\lambda} \hat{\Psi}_g(t') \\
&\approx \sum_{\mathbf{k},\lambda} \frac{-i\Omega}{2} u_{\mathbf{k}} \hat{a}_{\mathbf{k},\lambda} \hat{\Psi}_g(\tau + t_0) \int_{t_0}^{t+t_0} dt' e^{i\delta t'} \\
&= \sum_{\mathbf{k}',\lambda'} \frac{-\Omega}{2\delta} u_{\mathbf{k}'} \hat{a}_{\mathbf{k}',\lambda'} \hat{\Psi}_g(\tau + t_0) \left( e^{i\delta(\tau+t_0)} - e^{i\delta t_0} \right).
\end{aligned} \tag{B.35}$$

The approximation holds when, schematically,

$$|\delta| \gg |\Omega|, \tag{B.36}$$

since in this case the time-evolution of $\hat{\Psi}_g(t)$ is slow compared to $e^{i\delta t}$.

Taking $t = \tau + t_0$ and plugging this back into the interaction Hamiltonian, we

have

$$\hat{H}_{\text{int}} = \sum_{\mathbf{k},\lambda} \frac{\hbar}{2}\Omega \int d^3R \left( \sum_{\mathbf{k}',\lambda'} \frac{-\Omega}{2\delta} u_{\mathbf{k}'} \hat{a}_{\mathbf{k}',\lambda'} \hat{\Psi}_g \left( e^{i\delta t} - e^{i\delta t_0} \right) \right)^{\dagger} u_{\mathbf{k}} \hat{a}_{\mathbf{k},\lambda} e^{i\delta t} \hat{\Psi}_g + H.c.$$

$$= \sum_{\mathbf{k},\lambda,\mathbf{k}',\lambda'} \frac{-\hbar\Omega\Omega^*}{4\delta} \hat{a}^{\dagger}_{\mathbf{k}',\lambda'} \hat{a}_{\mathbf{k},\lambda} \int d^3R \hat{\Psi}^{\dagger}_g (\mathbf{R}) \, u^*_{\mathbf{k}'} (\mathbf{R}) \, u_{\mathbf{k}} (\mathbf{R}) \, \hat{\Psi}_g (\mathbf{R}) + H.c.$$

$$+ \Omega e^{i\delta t} O\left(\frac{\Omega}{\delta}\right) + H.c. \tag{B.37}$$

We drop the last terms by appealing to an iteration of this previous argument, which implies that

$$\Omega e^{i\delta t} O\left(\frac{\Omega}{\delta}\right) = \Omega O\left(\left(\frac{\Omega}{\delta}\right)^2\right). \tag{B.38}$$

By imposing the condition $|\delta| \gg |\Omega|$, we can drop this term. This is in fact the precise characterization of "far-enough" detuned. Now, this process can be repeated for any of the excited states that the state $|g\rangle$ is connected to. We then sum over all of these state to get an effective coupling,

$$g^{(g)}_{\mathbf{k},k',\lambda,\lambda'} = \sum_{\sigma} \frac{\Omega^{(\sigma g)*}_{\mathbf{k}',\lambda'} \Omega^{(\sigma g)}_{\mathbf{k},\lambda}}{2\delta^{(\sigma g)}_{\mathbf{k}}}. \tag{B.39}$$

In addition, this same process can be performed for the excited state in a two-level atom. In this case, we have

$$\hat{H}_{\text{int}} = \sum_{m\in\{e,g\}} \sum_{\mathbf{k},\lambda,\mathbf{k}',\lambda'} \hbar g^{(m)}_{\mathbf{k}',\lambda',\mathbf{k},\lambda} \hat{a}^{\dagger}_{\mathbf{k}',\lambda'} \hat{a}_{\mathbf{k},\lambda} \int d^3R \hat{\Psi}^{\dagger}_m (\mathbf{R}) \, u^*_{\mathbf{k}'} (\mathbf{R}) \, u_{\mathbf{k}} (\mathbf{R}) \, \hat{\Psi}_m (\mathbf{R}) . \tag{B.40}$$

Finally, we consider our two special cases. For the two-level atom interacting with the single-mode field, this becomes

$$\hat{H}_{\text{int}} = \hat{a}^{\dagger}_{\mathbf{k},\lambda} \hat{a}_{\mathbf{k},\lambda} \sum_{m\in\{e,g\}} \hbar g^{(m)}_{\mathbf{k},\lambda} \int d^3R \hat{\Psi}^{\dagger}_m (\mathbf{R}) \left| u_{\mathbf{k}} (\mathbf{R}) \right|^2 \hat{\Psi}_m (\mathbf{R}) . \tag{B.41}$$

For the case of atoms interacting with two counter-propagating, running-wave modes of an optical cavity, we have, assuming the same polarization,

$$\hat{H}_{\text{int}} = \sum_{m\in\{e,g\}} \sum_{\mathbf{k},\mathbf{k}'} \hbar g^{(m)} \frac{1}{V} \int d^3R \hat{\Psi}^{\dagger}_m (\mathbf{R})$$

$$\times \left( \hat{a}^{\dagger}_{\mathbf{k}} \hat{a}_{\mathbf{k}} + \hat{a}^{\dagger}_{\mathbf{k}} \hat{a}_{\mathbf{k}} + e^{-i2\mathbf{k}\cdot\mathbf{R}} \hat{a}^{\dagger}_{\mathbf{k}} \hat{a}_{-\mathbf{k}} + e^{i2\mathbf{k}\cdot\mathbf{R}} \hat{a}^{\dagger}_{-\mathbf{k}} \hat{a}_{\mathbf{k}} \right) \hat{\Psi}_m (\mathbf{R}) . \tag{B.42}$$